



UNIVERSITÀ  
DEGLI STUDI  
FIRENZE

UNIVERSITÀ DEGLI STUDI DI FIRENZE  
DIPARTIMENTO DI INGEGNERIA DELL'INFORMAZIONE (DINFO)  
CORSO DI DOTTORATO IN INGEGNERIA DELL'INFORMAZIONE  
CURRICULUM: ELETTRONICA, ELETTROMAGNETISMO ED  
ELETTROTECNICA (EEE)

---

# RECENT ADVANCES IN APPLIED ELECTROMAGNETISM AND MICROWAVE ENGINEERING

*Candidate*

Giacomo Giannetti

*Supervisors*

Prof. Giuseppe Pelosi

Prof. Stefano Maddio

Prof. Enrico Boni

*Ph.D. Coordinator*

Prof. Fabio Schoen

---

CICLO XXXVII, 2021-2024

Università degli Studi di Firenze, Dipartimento di Ingegneria  
dell'Informazione (DINFO).

Thesis submitted in partial fulfillment of the requirements for the degree of  
Doctor of Philosophy in Information Engineering. Copyright © 2025 by  
Giacomo Giannetti.

*Ad maiorem Dei gloriam*

## Acknowledgments

I deeply acknowledge my supervisors, Prof. Giuseppe Pelosi, Prof. Stefano Maddio, and Prof. Enrico Boni who stimulated and helped me during the Ph.D. program. In addition, many thanks go to Prof. Stefano Selleri, who largely contributed to the presented research endeavors, and to the other colleagues of the “RF, Microwaves, and Electromagnetics Laboratory”, Prof. Alessandro Cidronali, Dr. Giovanni Collodi, and Dr. Monica Righini, for the interesting discussions on my research. All these acknowledged persons are with the University of Florence, Florence, Italy.

Besides scholars at my home university, I warmly thank Prof. Ludger Klinkenbusch with the University of Kiel, Kiel, Germany, for his kind hospitality and support during my stay in Kiel; Prof. Gian Guido Gentili with the Polytechnic University of Milan, Milan, Italy, Prof. Jorge A. Ruiz-Cruz and Prof. Juan Córcoles with the Universidad Politécnica de Madrid, Madrid, Spain, and Dr. Ginés García Contreras with the Universidad Autónoma de Madrid, Madrid, Spain, for the useful discussions and supervision in the development of numerical methods for the analysis of closed waveguides; Prof. Holger Arthaber with the Technical University of Vienna, Vienna, Austria, and Dr. Christian Spindelberger with Rohde&Schwarz, Munich, Germany, for the help and support in the work on the transverse electromagnetic cell; Dr. Luca Piersanti, Dr. Simone Tocci, and Dr. Marco Bellaveglia with the National Laboratory of Frascati of the National Institute for Nuclear Physics, Rome, Italy, and Prof. Andrea Mostacci with La Sapienza University, Rome, Italy, for interesting discussions about microwave filters and the characterization of timing jitter for short electron beams; Prof. Yi Wang with the University of Birmingham, Birmingham, United Kingdom, for his warm and friendly hospitality during my stay in Birmingham in the framework of the European microwave association internship.

Eventually, I am grateful to my brother Dott. Guglielmo Giannetti both with Ducati Motor Holding, Bologna, Italy, and the University of Florence, Florence, Italy, with whom I shared the journey toward the Ph.D., for his invaluable help in the preparation of the technical drawings and his general support; my parents Sig. Andrea Giannetti and Dott.ssa Pina Crescenzi for their trust in my skills and support.

## Abstract

The thesis discusses the most recent advances in the following areas of (I) applied electromagnetism and (II) microwave engineering: (I.a) open scattering problems and (I.b) application programming interfaces; (II.a) microwave filters and diplexers, (II.b) transverse electromagnetic cells, (II.c) closed waveguide devices. For (I.a), an innovative method based on the equivalence principle and the spherical multipole expansion is developed. An arbitrarily shaped equivalence surface encloses a radiator solved numerically in a full-wave software. The equivalent currents on the equivalent surface are exported, and the impinging fields on a sphere enclosing the scatterer are computed using the free-space dyadic Green's function. Eventually, the scattering problem is solved using the transmission matrix approach. For (I.b), novel user-friendly application programming interfaces for HFSS in MATLAB and Python are developed. For operation, they replace the numerical values of the variables that describe the HFSS model with placeholders. Since they do not resort to visual basic for applications scripts, the developed interfaces are easier to setup. For (II.a), attention is drawn to the design of filters and diplexers. Two technologies are considered: the combine cavity and the microstrip. For the former technology, inductive and capacitive end couplings are compared and both a filter and a diplexer are designed for L-band applications. For the latter technology, design compactness and low loss are pursued using complementary low- and band-pass spiral resonators, and two diplexers are developed for satellite communications and personal communications/5G applications. For (II.b), an open transverse electromagnetic cell is designed with a cube of side 10 cm as a uniform test volume and operating in the frequency range 30 – 1000 MHz. An asymmetric design with an off-centered septum between the outer conductors is pursued. In addition, the return loss is improved using a smooth taper that realizes a  $50\ \Omega$ -characteristic impedance for minimum reflections. For (II.c), transformation optics is applied for analyzing closed waveguides. First, the boundary conditions are addressed, and the field is expanded to satisfy the boundary conditions. Second, cutoff eigenvalues and mode fields are computed for 2D cross sections. Third, mode fields are used to solve waveguide scattering problems with discrete discontinuities in a mode-matching framework. Fourth, transformation optics combined with hierarchical model reduction is applied to analyze waveguide devices with circular ports and smooth tapers.



# Contents

<b>Contents</b>	<b>VII</b>
<b>1 Introduction</b>	<b>1</b>
1.1 Objective . . . . .	1
1.2 Thesis structure . . . . .	1
1.3 Selected journal articles . . . . .	2
1.4 Conventions . . . . .	4
<b>I Applied Electromagnetism</b>	<b>7</b>
<b>2 Novel method for solving open scattering problems</b>	<b>9</b>
2.1 Introduction . . . . .	9
2.2 Methods . . . . .	11
2.2.1 Problem statement . . . . .	11
2.2.2 Proposed technique . . . . .	13
2.2.3 Coupling between the two subdomains . . . . .	14
2.3 Results and discussion . . . . .	17
2.4 Conclusion and future developments . . . . .	21
<b>3 New easy-to-implement application programming interfaces</b>	<b>23</b>
3.1 Introduction . . . . .	23
3.2 Methods . . . . .	25
3.3 Results and discussion . . . . .	26
3.4 Conclusion and future developments . . . . .	30

<b>II</b>	<b>Microwave Engineering</b>	<b>31</b>
<b>4</b>	<b>Innovative compact microwave filters and diplexers</b>	<b>33</b>
4.1	Introduction . . . . .	33
4.2	Methods . . . . .	34
4.2.1	Coaxial . . . . .	34
4.2.2	Microstrip . . . . .	37
4.3	Results and discussion . . . . .	39
4.3.1	Coaxial . . . . .	39
4.3.2	Microstrip . . . . .	44
4.4	Conclusion and future developments . . . . .	45
<b>5</b>	<b>Enhanced asymmetric open TEM cells</b>	<b>47</b>
5.1	Introduction . . . . .	47
5.2	Methods . . . . .	48
5.3	Results and discussion . . . . .	50
5.4	Conclusion and future developments . . . . .	52
<b>6</b>	<b>Advanced analysis techniques for closed waveguide devices</b>	<b>53</b>
6.1	Introduction . . . . .	53
6.2	Methods . . . . .	54
6.2.1	Domain transformation . . . . .	55
6.2.2	Boundary conditions . . . . .	57
6.2.3	Wave equation . . . . .	58
6.2.4	Field expansion . . . . .	58
6.2.5	Mode matching . . . . .	61
6.3	Results and discussion . . . . .	62
6.3.1	2D eigenvalue problems . . . . .	62
6.3.2	3D problems with excitation . . . . .	62
6.4	Conclusion and future developments . . . . .	68
<b>7</b>	<b>Conclusion and future developments</b>	<b>69</b>
7.1	Summary of contributions . . . . .	69
7.2	Directions for future work . . . . .	71
	<b>Nomenclature</b>	<b>73</b>
	<b>Acronyms</b>	<b>75</b>

<b>A Full list of publications</b>	<b>77</b>
<b>B Technical drawings</b>	<b>85</b>
<b>Bibliography</b>	<b>91</b>



# Chapter 1

## Introduction

### 1.1 Objective

The objective of this thesis is to illustrate in a structured and organic way the work carried out during the Ph.D. program. This is helped by the format of the thesis, that is, paper-based [1]. The journal articles on which the thesis is based are listed in Sect. 1.3. The full list of publications is reported instead in App. A. Each topic is introduced in a wide way, the works on the subjects are illustrated in a unified view, and some nonpublished materials and latest developments are also added. Not limited to this, the author also indicates the frontier of research and suggests the next potential developments.

According to [2], “The thesis for a Doctorate is based upon independent *original* research: upon an investigation in which the frontiers of knowledge have been explored and extended”. Inspired by this quote, the research focused on publishing the largest number of articles, even on different topics. This is at a premium, as interdisciplinarity is valuable in modern science [3].

### 1.2 Thesis structure

As indicated by the title, the two pillars of the thesis are applied electromagnetism (Pt. I) and microwave engineering (Pt. II). On the one hand, applied electromagnetism deals with the use of electromagnetism in applications such as antennas, filters, diplexers, and polarizers. The term “applied” is used to differentiate it from pure electromagnetism, which is usually used by physicists in fields such as nuclear fusion, particle and nuclear physics,

or astrophysics. Classical books on pure electromagnetism are [4–6], while popular books on applied electromagnetism are [7–9]. Of course, the border between the two areas is indicative.

The subjects of research in applied electromagnetism are as follows:

**Ch. 2** novel method for solving open scattering problems;

**Ch. 3** new easy-to-implement application programming interfaces.

On the other hand, microwave engineering deals with microwave devices and applications. Microwaves are electromagnetic waves comprised in the spectrum between 300 MHz and 300 GHz. Classical books on microwave engineering are [8, 10, 11]. The thesis focuses on these topics:

**Ch. 4** innovative compact microwave filters and diplexers;

**Ch. 5** enhanced asymmetric open TEM cells;

**Ch. 6** advanced analysis techniques for closed waveguide devices.

The topics relate to both design (Ch. 3, Ch. 4, and Ch. 5) and analysis (Ch. 2, Ch. 3, Ch. 5, and Ch. 6). Eventually, Ch. 7 summarizes the main findings of the thesis and provides an outlook for future developments.

### 1.3 Selected journal articles

At least a journal article has been published for each topic analyzed in the thesis. The list of publications on which the thesis is based is as follows. For each manuscript, the contributions of the Ph.D. candidate according to the CRediT taxonomy [12] are also listed:

**Ch. 2** [13] **G. Giannetti** and L. Klinkenbusch, “A numerical alternative for 3D addition theorems based on the bilinear form of the dyadic Green’s function and the equivalence principle,” *Advances in Radio Science*, vol. 22, pp. 9–15, 2024.

**Contributions of the Ph.D. candidate.** *Conceptualization, Formal Analysis, Methodology, Software, Validation, Visualization, Writing – original draft, and Writing – review & editing;*

- Ch. 3** [14] **G. Giannetti**, “Improved and easy-to-implement HFSS-MATLAB interface without VBA scripts: an insightful application to the numerical design of patch antennas,” *The Applied Computational Electromagnetics Society Journal*, vol. 38, no. 06, pp. 377–381, 2023.

**Contributions of the Ph.D. candidate.** *Conceptualization, Formal Analysis, Methodology, Project Administration, Software, Supervision, Validation, Visualization, Writing – original draft, and Writing – review & editing;*

- Ch. 4** [15] E. Boni, **G. Giannetti**, S. Maddio, and G. Pelosi, “Comparison of inductive and capacitive end couplings in the design of a combline microwave cavity filter for the E1 Galileo band,” *Advances in Radio Science*, vol. 22, pp. 1–8, 2024

**Contributions of the Ph.D. candidate.** *Investigation, Methodology, Validation, Visualization, Writing – original draft, and Writing – review & editing;*

[16] **G. Giannetti**, S. Maddio, and E. Boni, “Compact all-metal inline combline coaxial cavity diplexer,” *Journal of Telecommunications and Information Technology*, pp. 9–14, Oct. 2024.

**Contributions of the Ph.D. candidate.** *Investigation, Methodology, Validation, Visualization, Writing – original draft, and Writing – review & editing;*

[17] **G. Giannetti** and S. Maddio, “Low-loss compact diplexer based on complementary spiral resonators,” *Microwave and Optical Technology Letters*, vol. 66, no. 6, 2024.

**Contributions of the Ph.D. candidate.** *Data Curation, Investigation, Methodology, Validation, Visualization, Writing – original draft, and Writing – review & editing;*

[18] **G. Giannetti**, S. Maddio, and S. Selleri, “A compact low-loss single-layer vialess diplexer based on complementary microstrip spiral resonators for satellite communications,” *Progress In Electromagnetics Research Letters*, vol. 122, pp. 45–51, 2024.

**Contributions of the Ph.D. candidate.** *Data Curation, Investigation, Methodology, Validation, Visualization, Writing – original draft, and Writing – review & editing;*

- Ch. 5** [19] **G. Giannetti**, C. Spindelberger, and H. Arthaber, “Simple semi-

analytical septum design for improved matching in open TEM cells,” *IEEE Letters on Electromagnetic Compatibility Practice and Applications*, vol. 6, no. 1, pp. 6–10, 2024.

**Contributions of the Ph.D. candidate.** *Conceptualization, Data Curation, Formal Analysis, Methodology, Software, Validation, Visualization, Writing – original draft, and Writing – review & editing;*

**Ch. 6** [20] G. G. Gentili, **G. Giannetti**, G. Pelosi, and S. Selleri, “Considerations on boundary conditions in transformation optics for complete field computation in generic waveguides,” *Microwave and Optical Technology Letters*, vol. 65, no. 1, pp. 373–380, 2023.

**Contributions of the Ph.D. candidate.** *Conceptualization, Formal Analysis, Methodology, Software, Validation, Visualization, Writing – original draft, and Writing – review & editing;*

[21] G. G. Gentili, **G. Giannetti**, G. Pelosi, and S. Selleri, “Transformation optics combined with line-integrals for fast and efficient mode matching analysis of waveguide devices,” *IEEE Journal of Microwaves*, vol. 3, no. 3, pp. 1051–1060, 2023.

**Contributions of the Ph.D. candidate.** *Conceptualization, Formal Analysis, Methodology, Software, Validation, Visualization, Writing – original draft, and Writing – review & editing;*

[22] **G. Giannetti**, S. Selleri, G. G. Gentili, G. Garcia-Contreras, J. Córcoles, and J. A. Ruiz-Cruz, “Advanced modeling of circular waveguide-based devices with smooth profiles using transformation optics and hierarchical model reduction,” *IEEE Journal of Microwaves*, vol. 4, no. 4, pp. 675–689, 2024.

**Contributions of the Ph.D. candidate.** *Conceptualization, Formal Analysis, Methodology, Software, Validation, Visualization, Writing – original draft, and Writing – review & editing.*

## 1.4 Conventions

Throughout the text, a harmonic time factor  $e^{j\omega t}$ , with  $j$  the imaginary unit,  $\omega$  the angular frequency, and  $t$  the time, is assumed and suppressed, and the following conventions for the nomenclature are adopted:

- Roman font for scalar nonphysical constants as the Euler’s number  $e$ ;

- italic for scalar physical quantities, e.g.,  $e$ ;
- bold italic for physical vectors, e.g.,  $\mathbf{E}$ ;
- uppercase with double bar for physical tensors  $\bar{\bar{E}}$ ;
- bold lowercase for algebraic vectors, e.g.,  $\mathbf{e}$ ;
- bold uppercase for algebraic matrices, e.g.,  $\mathbf{E}$ .



# Part I

## Applied Electromagnetism



# Chapter 2

## Novel method for solving open scattering problems

### 2.1 Introduction

Open scattering problems are common in applied electromagnetism. In such problems, an object or scatterer is illuminated by electromagnetic waves. The illuminating field may be radiated by an antenna or other sources. Instances are the waves radiated by a radar that impinge on an airplane or the waves emitted by satellites for Earth observation purposes. The term “open” indicates that the waves are not confined within closed structures as for guided waves [23], which are addressed in Ch. 6.

The open scattering problems are usually solved numerically since analytical solutions are available only for a few specific cases. Computational electromagnetics is the subject that deals with the numerical analysis of electromagnetic problems as are considered here. Recent reviews on this broad topic are [24, 25]. Unified and panoramic views are given in [26] and [27], respectively. A recent book is [28], while older ones are [29–32].

The domain of open scattering problems is usually electrically large, that is, the problem spans dozens of wavelengths or even more. To solve such problems, domain decomposition [33–35] was introduced in the 1990s and 2000s. Domain decomposition is a technique used to split an electrically large problem into smaller parts, called subdomains, that can be solved separately. The solutions to the subdomains are then joined together through a suitable coupling scheme to solve the entire original problem. In addition,

domain decomposition adds a degree of flexibility since each of the subdomains can be solved with different methods, thus allowing us to choose the best computational method for each subdomain.

Examples in which domain decomposition is applied are described. A suitable numerical method for antenna analysis is the equivalence principle algorithm [36,37]. The antenna is solved using the method of moments and the scattering problem using the transmission matrix (T-matrix) method. In [38,39], far fields impinging on scatterers are considered. These are enclosed by spheres, and their interactions are solved using the T-matrix approach. On the other hand, in [40] a radiator is examined as well, but a single scatterer is considered. Both the antenna and the scatterer are enclosed by nonintersecting spheres and the fields from one subdomain to the other are computed using the T-matrix method. However, the distance between objects is limited by the dimensions of the enclosing spheres, and this drawback is more critical if the enclosed objects are elongated, as for a dipole antenna.

The matrix formulation of scattering, also known as the T-matrix method, was introduced in [41] and a comprehensive review is given in [42]. The matrix formulation is efficient since it relates the incident and reflected multipole amplitude coefficients with a matrix, called transmission matrix. This can be computed in different ways: analytically, for canonical shapes such as (layered) spheres using the null-field method, also known as the extended boundary condition method [41–43]; numerically, via, for example, the impedance matrix from the method of moments formulation [40], or using far fields [44].

The fact that the spheres enclosing the objects, that is, the antenna and scatterer, do not have to intersect is a drawback of the classical method. This limits the minimum distance between either the scatterers or between the radiator and the scatterer. As mentioned above, the limitation becomes more pronounced when the antenna or scatterer displays a large aspect ratio, such as with an electric dipole that is long in one dimension and short in the other two. To overcome this drawback, a numerical method using the dyadic Green's function alongside the equivalence principle is introduced in [13] and described below. Two subdomains are considered: one with an antenna and the other with a scatterer. An arbitrary Huygens surface encloses the radiator. Hence, the method is more flexible and reduces the minimum allowed distance between subdomains. The scattered field is then calculated using the T-matrix method. The scatterer may have any geometry, but the analysis becomes considerably simpler when dealing with a spherical

scatterer, such as the model representing the human head [40]. In this case, the scatterer is a layered dielectric sphere.

Preliminary work has been performed in [45], where the 2D problem (TE polarization) is considered. As a further step, the 3D problem is addressed in [13]. Research in [45] has been carried out during the stay of the author at Kiel University and has been awarded the Young Scientist Award and the Young Scientist Best Paper Award (2<sup>nd</sup> place) at the Kleinheubach conference in 2023. As an extension to the 3D case, [13] has been published in the journal *Advances in Radio Science*.

The chapter is organized as follows. The statement of the scattering problem, the proposed method, and the coupling between subdomains to include multiple interactions are outlined in Sect. 2.2. The results of the proposed method are presented and discussed in Sect. 2.3. Eventually, the conclusion and future developments are described in Sect. 2.4.

## 2.2 Methods

### 2.2.1 Problem statement

The setting considered (Fig. 2.1) is composed of an antenna, reference system  $\mathbf{r}_a = (r_a, \theta_a, \varphi_a)$ , and a scatterer, reference system  $\mathbf{r}' = (r', \theta', \varphi')$ . The latter is contained within a sphere of radius  $R_s$ . In the phasor domain, the multipole expansions of the incident ( $\mathbf{E}^i$ ) and scattered ( $\mathbf{E}^s$ ) electric fields

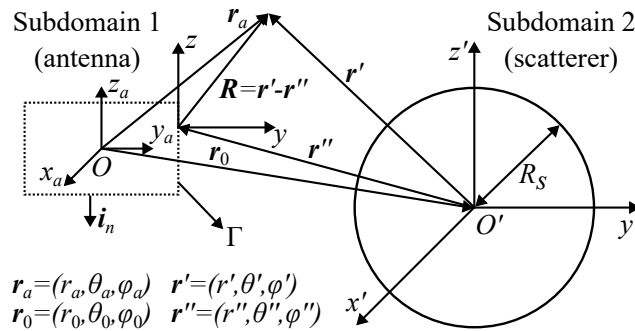


Figure 2.1: Problem setting: subdomain 1 (antenna) and subdomain 2 (scatterer) (Adapted from [13] Creative Commons Attribution 4.0 License).

in the reference system of the scatterer (subdomain 2 in Fig. 2.1) are [46]

$$\mathbf{E}^i(\mathbf{r}') = \sum_{n=1}^N \sum_{m=-n}^n a_{n,m}^i \mathbf{N}_{n,m}^{(1)}(\mathbf{r}') + \frac{Z}{j} \sum_{n=1}^N \sum_{m=-n}^n b_{n,m}^i \mathbf{M}_{n,m}^{(1)}(\mathbf{r}') \quad (2.1a)$$

$$\mathbf{E}^s(\mathbf{r}') = \sum_{n=1}^N \sum_{m=-n}^n a_{n,m}^s \mathbf{N}_{n,m}^{(2)}(\mathbf{r}') + \frac{Z}{j} \sum_{n=1}^N \sum_{m=-n}^n b_{n,m}^s \mathbf{M}_{n,m}^{(2)}(\mathbf{r}'), \quad (2.1b)$$

where  $\mathbf{r}'$  is the observation point, the summations over  $n$  are truncated up to  $n = N$  for a practical implementation, and  $Z = \sqrt{\mu/\varepsilon}$  is the wave impedance, with  $\varepsilon$  and  $\mu$  the permittivity and permeability of the background medium (vacuum in this case), respectively. The coefficients  $a_{n,m}^{i(s)}$  and  $b_{n,m}^{i(s)}$  represent the multipole coefficients of the incident (scattered) electromagnetic field. The vector spherical multipole functions (VSMFs)  $\mathbf{N}_{n,m}^{(q)}(\mathbf{r}')$  and  $\mathbf{M}_{n,m}^{(q)}(\mathbf{r}')$  are defined as [46]

$$\mathbf{M}_{n,m}^{(q)}(\mathbf{r}') = z_n^{(q)}(kr') \mathbf{m}_{n,m}(\theta', \varphi') \quad (2.2a)$$

$$\mathbf{N}_{n,m}^{(q)}(\mathbf{r}') = -\frac{z_n^{(q)}(kr')}{kr'} n(n+1) Y_{n,m}(\theta', \varphi') \mathbf{i}_{r'} + w_n^{(q)}(kr') \mathbf{n}_{n,m}(\theta', \varphi'). \quad (2.2b)$$

Here,  $w_n^{(q)}(kr') = -\frac{1}{kr'} \frac{d}{dr'} (r' z_n^{(q)}(kr'))$ ,  $\mathbf{i}_r$  is the unit vector in the radial direction, and  $k = \omega\sqrt{\mu\varepsilon}$  is the wavenumber of the background medium. The superscripts  $(q) = (1)$  and  $(q) = (2)$  indicate that the radial dependence is given by spherical Bessel functions of the first kind ( $z_n^{(1)} = j_n$ ) or spherical Hankel functions of the second kind ( $z_n^{(2)} = h_n^{(2)}$ ), respectively. Note that spherical Bessel functions of the first kind are regular everywhere and must be used to represent regular fields at the origin ( $r' = 0$ ), while at the given time factor only Hankel functions of the second kind comply with the radiation condition for  $r' \rightarrow \infty$ .

The transverse spherical multipole functions (TSMFs)  $\mathbf{m}_{n,m}(\theta', \varphi')$  and  $\mathbf{n}_{n,m}(\theta', \varphi')$  are defined as

$$\mathbf{m}_{n,m}(\theta', \varphi') = -\frac{1}{\sin(\theta')} \frac{\partial Y_{n,m}(\theta', \varphi')}{\partial \varphi'} \mathbf{i}_{\theta'} + \frac{\partial Y_{n,m}(\theta', \varphi')}{\partial \theta'} \mathbf{i}_{\varphi'} \quad (2.3a)$$

$$\mathbf{n}_{n,m}(\theta', \varphi') = \frac{\partial Y_{n,m}(\theta', \varphi')}{\partial \theta'} \mathbf{i}_{\theta'} + \frac{1}{\sin(\theta')} \frac{\partial Y_{n,m}(\theta', \varphi')}{\partial \varphi'} \mathbf{i}_{\varphi'}, \quad (2.3b)$$

where  $\mathbf{i}_{\theta'}$  and  $\mathbf{i}_{\varphi'}$  are the unit vectors along  $\theta'$  and  $\varphi'$ , respectively, and the

surface spherical harmonics  $Y_{n,m}(\theta', \varphi')$  are defined by

$$Y_{n,m}(\theta', \varphi') = \sqrt{\frac{(n-m)! 2n+1}{(n+m)! 4\pi}} P_n^m(\cos(\theta')) e^{jm\varphi'}. \quad (2.4)$$

where  $P_n^m(\cos(\theta'))$  denotes an associated Legendre function of the first kind.

The multipole expansions (2.1a) and (2.1b) are valid only outside the scatterer, that is, for  $r' > R_s$ . For  $r' \leq R_s$ , the field expansion is [46]

$$\mathbf{E}^{\text{in}}(\mathbf{r}') = \sum_{n=1}^N \sum_{m=-n}^n a_{n,m}^{\text{in}} \hat{\mathbf{N}}_{n,m}^{(1)}(\mathbf{r}') + \frac{\hat{Z}}{j} \sum_{n=1}^N \sum_{m=-n}^n b_{n,m}^{\text{in}} \hat{\mathbf{M}}_{n,m}^{(1)}(\mathbf{r}'), \quad (2.5)$$

where  $a_{n,m}^{\text{in}}$  and  $b_{n,m}^{\text{in}}$  are the multipole coefficients and the hat indicates that the medium is now different [ $\hat{k}$  and  $\hat{Z}$  (2.5) replace  $k$  and  $Z$  in (2.1a)].

In the T-matrix approach, the transmission matrix  $\mathbf{T}$  fully characterizes the scatterer and relates the multipole coefficients of the impinging and scattered waves. For the homogeneous isotropic dielectric sphere considered here, matrix  $\mathbf{T}$  is diagonal and relates the multipole coefficients as [42]

$$a_{n,m}^{\text{in}} = T_n^{(1)} a_{n,m}^{\text{i}} \quad b_{n,m}^{\text{in}} = T_n^{(-1)} b_{n,m}^{\text{i}}, \quad (2.6)$$

where the diagonal entries of the scattering matrix, derived enforcing the continuity of the transverse fields on the scatterer surface, are

$$T_n^{(\gamma)} = \frac{w_n^{(1)}(kR_s)}{w_n^{(1)}(\hat{k}R_s)} \frac{1 - \frac{z_n^{(1)}(kR_s) w_n^{(2)}(kR_s)}{z_n^{(2)}(kR_s) w_n^{(1)}(kR_s)}}{1 - \left(\frac{Z}{\hat{Z}}\right)^\gamma \frac{z_n^{(1)}(\hat{k}R_s) w_n^{(2)}(kR_s)}{z_n^{(2)}(kR_s) w_n^{(1)}(\hat{k}R_s)}}. \quad (2.7)$$

From (2.7), note that  $T_n^{(\gamma)} = 1$  when  $\hat{k} = k$  and  $\hat{Z} = Z$ .

### 2.2.2 Proposed technique

First, the equivalence principle is applied to replace the radiating antenna with a Huygens surface enclosing the antenna (Fig. 2.1). The equivalent currents on the equivalence surface are [7]

$$\mathbf{J}_{\text{eq}} = \mathbf{i}_n \times \mathbf{H}^a(\Gamma) \quad \mathbf{M}_{\text{eq}} = -\mathbf{i}_n \times \mathbf{E}^a(\Gamma), \quad (2.8)$$

where  $\Gamma$  is the Huygens surface, and  $\mathbf{i}_n$  the unit vector directed outwards (Fig. 2.1). The equivalent currents (2.8) are derived from the fields obtained

using the method applied to solve the electromagnetic problem in subdomain 1, in this case the full-wave simulator (FWS) CST [47].

The electromagnetic field outside of the equivalence surface is [7,36,48,49]

$$\mathbf{E}(\mathbf{r}') = -jkZ\mathcal{L}\{\mathbf{J}_{\text{eq}}(\mathbf{r}'')\} - \mathcal{K}\{\mathbf{M}_{\text{eq}}(\mathbf{r}'')\} \quad (2.9a)$$

$$\mathbf{H}(\mathbf{r}') = -jkY\mathcal{L}\{\mathbf{M}_{\text{eq}}(\mathbf{r}'')\} + \mathcal{K}\{\mathbf{J}_{\text{eq}}(\mathbf{r}'')\}, \quad (2.9b)$$

where  $\mathcal{K}$  and  $\mathcal{L}$  are integral operators defined by

$$\mathcal{K}\{\mathbf{I}_{\text{eq}}(\mathbf{r}'')\} = \int_{\Gamma} \nabla' g(\mathbf{r}', \mathbf{r}'') \times \mathbf{I}_{\text{eq}}(\mathbf{r}'') dS'' \quad (2.10a)$$

$$\mathcal{L}\{\mathbf{I}_{\text{eq}}(\mathbf{r}'')\} = \int_{\Gamma} \bar{\bar{G}}(\mathbf{r}', \mathbf{r}'') \cdot \mathbf{I}_{\text{eq}}(\mathbf{r}'') dS''. \quad (2.10b)$$

In (2.10a) and (2.10b),  $\mathbf{I}_{\text{eq}}$  is either  $\mathbf{M}_{\text{eq}}$  or  $\mathbf{J}_{\text{eq}}$ , and  $\mathbf{r}''$  is the source point in the scatterer reference system (Fig. 2.1). In (2.10a), the  $\nabla'$  operates on  $\mathbf{r}'$ , the observation point. The free-space scalar Green's function  $g(\mathbf{r}', \mathbf{r}'') = g(R)$ , the free-space dyadic Green's function  $\bar{\bar{G}}(\mathbf{r}', \mathbf{r}'')$  and the term  $\nabla' g(\mathbf{r}', \mathbf{r}'')$  in (2.10a) are well known and their expressions can be found in [13,23,50].

Evaluating (2.9a) and (2.9b) on the spherical surface enclosing the scatterer ( $r' = R_s$ ),  $\mathbf{E}^i(\mathbf{r}')\big|_{r'=R_s}$  and  $\mathbf{H}^i(\mathbf{r}')\big|_{r'=R_s}$  are obtained and the multipole coefficients of the incident field  $a_{n,m}^i$  and  $b_{n,m}^i$  are calculated from their radial components by using the orthogonality of the VSMFs and TSMFs [46]

$$a_{n,m}^i = -\frac{kR_s \int_0^{2\pi} \int_0^\pi \mathbf{E}^i(\mathbf{r}')\big|_{r'=R_s} \cdot \mathbf{i}_{r'} Y_{n,m}^*(\theta', \varphi') \sin(\theta') d\theta' d\varphi'}{n(n+1)j_n(kR_s)} \quad (2.11a)$$

$$b_{n,m}^i = -\frac{kR_s \int_0^{2\pi} \int_0^\pi \mathbf{H}^i(\mathbf{r}')\big|_{r'=R_s} \cdot \mathbf{i}_{r'} Y_{n,m}^*(\theta', \varphi') \sin(\theta') d\theta' d\varphi'}{n(n+1)j_n(kR_s)}, \quad (2.11b)$$

where \* indicates the complex conjugate. For comparison, hereafter the incident coefficients  $a_{n,m}^i$  and  $b_{n,m}^i$  are computed using the incident electric and magnetic fields in (2.11a) and (2.11) directly derived from a FWS.

### 2.2.3 Coupling between the two subdomains

So far, no interaction between the two subdomains has been considered. Now, a possible way to perform this interaction and then solve the complete

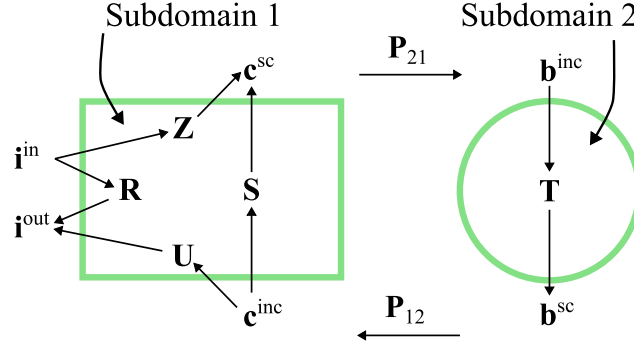


Figure 2.2: Pictorial representation of the generalized scattering problem.

scattering problem is described. This part is novel and has not yet been published. It may be the subject of a future manuscript.

A schematic view of the interaction between the two subdomains is depicted in Fig. 2.2. In this, the antenna is characterized by a matrix  $\mathbf{S}$  that links the incident and radiated fields. Analogously, the scatterer is modeled with the T-matrix method. Then, matrix  $\mathbf{T}$  links the coefficients of the impinging and scattered waves (2.6).

To solve the complete scattering problem, the effects of the scatterer on the antenna must be taken into account. Particularly, from Fig. 2.2 we have

$$\mathbf{i}^{\text{out}} = \mathbf{R}\mathbf{i}^{\text{in}} + \mathbf{U}\mathbf{c}^{\text{inc}} \quad (2.12a)$$

$$\mathbf{c}^{\text{sc}} = \mathbf{Z}\mathbf{i}^{\text{in}} + \mathbf{S}\mathbf{c}^{\text{inc}} \quad (2.12b)$$

$$\mathbf{b}^{\text{inc}} = \mathbf{P}_{21}\mathbf{c}^{\text{sc}} \quad (2.12c)$$

$$\mathbf{b}^{\text{sc}} = \mathbf{T}\mathbf{b}^{\text{inc}} \quad (2.12d)$$

$$\mathbf{c}^{\text{inc}} = \mathbf{P}_{12}\mathbf{b}^{\text{sc}}, \quad (2.12e)$$

being 1 (2) the index for the antenna (scatterer) and

- $\mathbf{b}^{\text{inc}}$  ( $\mathbf{b}^{\text{sc}}$ ) the vector containing the multipole coefficients of the wave impinging on (scattered by) the scatterer;
- $\mathbf{c}^{\text{inc}}$  ( $\mathbf{c}^{\text{sc}}$ ) the vector containing the weights associated with basis functions for both types of equivalent currents impinging on (scattered by) the antenna;
- $\mathbf{i}^{\text{in}}$  the currents feeding the ports of the antenna. They are the source of the problem;

- $\mathbf{i}^{\text{out}}$  the currents flowing out from the ports;
- $\mathbf{T}$  the T-matrix characterizing the scattering;
- $\mathbf{S}$  the generalized scattering matrix of the antenna obtained, for instance, by applying the equivalence principle algorithm [36]. It accounts for the field scattered by the antenna;
- $\mathbf{U}$  the matrix accounting for the field impinging on the antenna that is converted into currents flowing out from the ports;
- $\mathbf{R}$  the matrix accounting for the reflected currents at ports;
- $\mathbf{Z}$  the matrix accounting for the conversion into the fields radiated by the antenna due to the currents feeding the ports of the antenna;
- $\mathbf{P}_{21}$  ( $\mathbf{P}_{12}$ ) the transition matrix from the antenna to the scatterer (from the scatterer to the antenna).

The formulation (2.12) can be solved iteratively or directly by inversion and can be extended to an arbitrary number of scatterers and antennas.

For a prescribed port excitation  $\mathbf{i}^{\text{in}} \neq \mathbf{0}$ ,  $\mathbf{c}^{\text{inc}}$ ,  $\mathbf{c}^{\text{sc}}$ ,  $\mathbf{b}^{\text{inc}}$ ,  $\mathbf{b}^{\text{sc}}$  and  $\mathbf{i}^{\text{out}}$  are unknown. In a direct solution, the coefficients  $\mathbf{b}^{\text{inc}}$  are computed as

$$\mathbf{b}^{\text{inc}} = (\mathbf{P}_{21}^{-1} - \mathbf{S}\mathbf{P}_{12}\mathbf{T})^{-1} \mathbf{Z}\mathbf{i}^{\text{in}}. \quad (2.13)$$

Note that (2.13) requires matrix inversion. Then, a preconditioning matrix [51] may be needed. For an iterative solution, all unknowns are set to zero in the first step ( $i = 0$  with  $i$  an index). The unknowns at the next step  $i + 1$  can be computed from the unknowns at the previous step  $i$  as follows

$$(1) \quad \mathbf{c}^{\text{sc}}(i + 1) = \mathbf{Z}\mathbf{i}^{\text{in}} + \mathbf{S}\mathbf{c}^{\text{inc}}(i) \quad (2.14a)$$

$$(2) \quad \mathbf{b}^{\text{inc}}(i + 1) = \mathbf{P}_{21}\mathbf{c}^{\text{sc}}(i + 1) \quad (2.14b)$$

$$(3) \quad \mathbf{b}^{\text{sc}}(i + 1) = \mathbf{T}\mathbf{b}^{\text{inc}}(i + 1) \quad (2.14c)$$

$$(4) \quad \mathbf{c}^{\text{inc}}(i + 1) = \mathbf{P}_{12}\mathbf{b}^{\text{sc}}(i + 1), \quad (2.14d)$$

Interestingly, the iterative solution does not require matrix inversion. Possible convergence criteria are

$$\|\mathbf{d}(i + 1) - \mathbf{d}(i)\|_l \leq \delta, \quad (2.15)$$

with  $\mathbf{d}$  either  $\mathbf{b}^{\text{inc}}$ ,  $\mathbf{b}^{\text{sc}}$ ,  $\mathbf{c}^{\text{inc}}$ ,  $\mathbf{c}^{\text{sc}}$ , or  $\mathbf{i}^{\text{out}}$ ,  $l$  an integer fixing the norm and  $\delta$  a threshold. This criterion derives from (2.12). The conditions under which (2.15) converges and the rate of convergence must be carefully analyzed and will be the subject of further research.

The matrices  $\mathbf{S}$ ,  $\mathbf{U}$ ,  $\mathbf{Z}$ , and  $\mathbf{R}$  characterize the antenna and derive from the discretization of integral equations. They then depend on the basis and expansion functions used for the discretization (for instance, Rao-Wilton-Glisson basis functions [52], or Dirac functions in the collocation or point matching method [43]). The matrices mentioned above, together with the matrix  $\mathbf{T}$ , do not depend on the relative position of the scatterer and the antenna. In contrast, matrices  $\mathbf{P}_{21}$  and  $\mathbf{P}_{12}$  depend on the relative position of the antenna and the scatterer. After a suitable discretization, they link the weights associated with the basis functions on the equivalence surface enclosing the antenna with the multipole coefficients impinging on the scatterer and vice versa. They also depend on the discretization used for the antenna.

## 2.3 Results and discussion

The antenna and its technical drawings are shown in Fig. 2.3. A single frequency  $f_0 = 2$  GHz ( $\lambda \approx 150$  mm, being  $\lambda$  the wavelength at  $f_0$ ) is considered. However, the method may be extended to a bandwidth in a straightforward way by applying a model-based parameter extraction [53–55] and to the time domain by applying a Fourier transform. The antenna is analyzed by the commercial CST<sup>®</sup> time-domain solver (20 cells per wavelength) and at  $f_0$  presents a return loss of 20.7 dB. The scatterer is a lossless isotropic sphere with radius  $R_s = 30$  mm and relative dielectric permittivity  $\varepsilon_r = 2.2$ .

The box for the equivalence principle and the sphere enclosing the antenna are also shown in Fig. 2.3(a). The box is tighter to the antenna than the sphere. Hence, the minimum distance between the antenna and the scatterer is smaller when the box is used. The box has its sides orthogonal to either  $\mathbf{i}_{x'}$ ,  $\mathbf{i}_{y'}$ , or  $\mathbf{i}_{z'}$ , its center in the antenna reference system is located at  $(x_a = 0$  mm,  $y_a = 0$  mm,  $z_a = -31$  mm) and the lengths of the  $x$ -,  $y$ -, and  $z$ -sides of the box are 325.1 mm =  $2.17\lambda$ , 270.5 mm =  $1.80\lambda$ , and 692.0 mm =  $4.62\lambda$ , respectively. The integral operators are discretized using the point matching method [43]. The distance between the matching points is  $\lambda/20 \approx 7.5$  mm, and then the fields are exported over 18,322 points.

Two positions of the scatterer are considered:

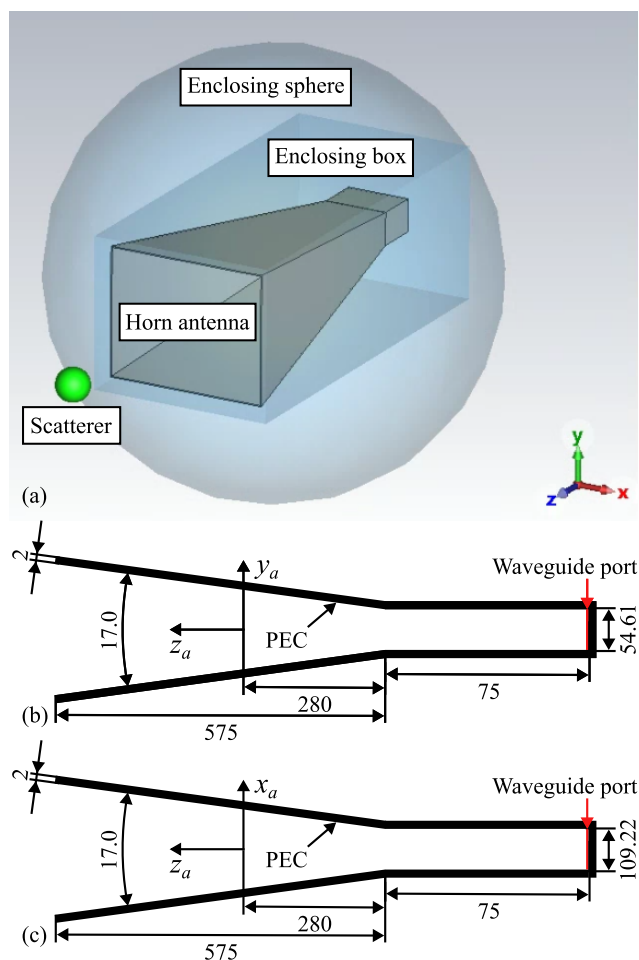


Figure 2.3: View of the problem and technical drawings of the antenna: (a) 3D view of the problem in CST; not-in-scale cross sections of the antenna on (b) the  $yz$ -plane and (c) the  $xz$ -plane. The antenna is fed by a rectangular WR430 waveguide. In (b) and (c), the dimensions are in millimeters except for the taper angles that are in degrees (Adapted from [13] Creative Commons Attribution 4.0 License).

- P1:  $O' = (15, 30, 700)\text{mm}$ ,  $r_0 = 700.8\text{ mm}$ ;
- P2:  $O' = (0, 0, 375)\text{mm}$ ,  $r_0 = 375.0\text{ mm}$ ,

where  $r_0$  is the distance between the origins of the two reference systems (Fig. 2.1). The electrical distances  $kr_0$  are 29.4 and 15.7 for P1 and P2, respectively. For P1, both the proposed method and the classical method based on the addition theorem for VSMFs are applicable. However, P2 can

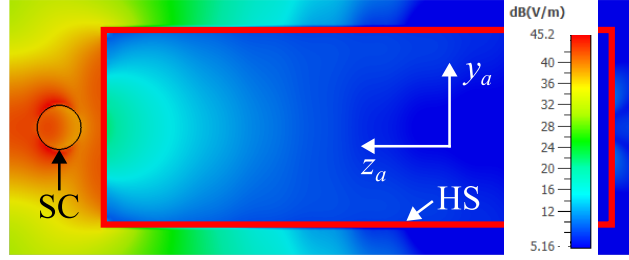


Figure 2.4: Maximum magnitude of the electric field on  $x_a = 0$  mm (Fig. 2.3.b). The equivalence principle is applied in CST with the scatterer in P2. SC stands for scatterer and HS for Huygens' surface (Adapted from [13] Creative Commons Attribution 4.0 License).

be analyzed only with the method proposed here since in this case the spheres enclosing the antenna and the scatterer intersect.

To compare the proposed method and CST, the CST results are obtained by loading the equivalent currents as near-field sources and replacing the antenna with the Huygens surface (Fig. 2.4). More details are given in [13].

For P1, the multipole coefficients of the incident electromagnetic field  $a_{n,m}^i$  and  $(Z/j)b_{n,m}^i$  are shown in Fig. 2.5(P1a and P1b) while those of the field inside the scatterer  $a_{n,m}^{\text{in}}$  and  $(\hat{Z}/j)b_{n,m}^{\text{in}}$  are shown in Fig. 2.5(P1aS and P1bS). The results agree well, except for slight discrepancies between the two methods that occur when the magnitude of the coefficients is less than  $1 \text{ V m}^{-1}$  ( $1 \text{ W rms}$  input power), that is, it becomes less relevant.

Similarly, the results for P2 are depicted in Fig. 2.5(P2a and P2b) and Fig. 2.5(P2aS and P2bS). For this case too, the results are accurate, even if the magnitudes of the multipole coefficient decrease less with increasing order due to the shorter distance between the scatterer and the antenna.

The error between the results from this technique (TT) and CST is [13]

$$\epsilon_{n,m}^{c,(s)} = 20 \log_{10} \left( \frac{\left| c_{n,m}^{(s) \text{ TT}} - c_{n,m}^{(s) \text{ CST}} \right| \cdot F_n}{\max_{n,m} \left( \left| c_{n,m}^{(s) \text{ CST}} \right| \cdot F_n \right)} \right) \quad (2.16)$$

with

$$F_n = \frac{1}{\sqrt{n}} \left( \frac{1}{n} \right)^n, \quad (2.17)$$

where  $c$  is either  $a$  or  $b$ , and  $(s)$  is either (i) for the incident field or (in) for the field inside the scatterer. In (2.16),  $n$  and  $m$  range from 1 to  $N$  and

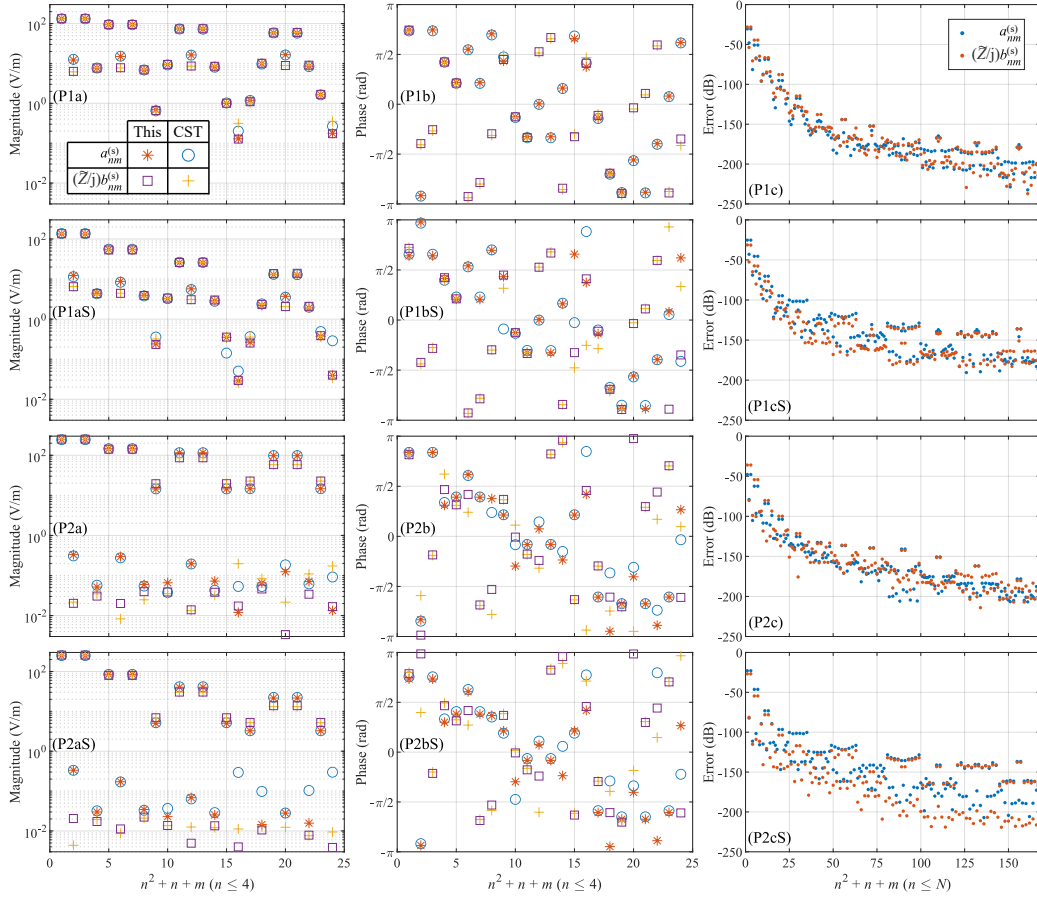


Figure 2.5: Coefficients and errors for expansions (2.1a) and (2.5). In the labels, P1 or P2 specifies the scatterer position; a is for the magnitude, b the phase, and c the error (2.16); with [without] letter S for scatterer, (s) = (i) [(in)] and  $\tilde{Z} = Z$  [ $\hat{Z}$ ]. The legend of (P1a) [(P1c)] is the same for all the graphs in the first two [third] columns. Part of the data is from [13].

from  $-n$  to  $n$ , respectively, as for the double summations in (2.1a). See [13] for more details on the interpretation of error (2.16). The errors defined according to (2.16) are drawn in Fig. 2.5.

In Table 2.1, the maximum values for the error (2.16) are given. The error increases if the scatterer is considered. This may be due to the surface approximation made by CST in meshing the scatterer (Fig. 2.6). A sphere is indeed difficult to mesh with hexahedrons as used by the CST time domain solver. With (without) the scatterer, the error is greater (less) for P2 than for P1. Without (with) scatterer, the error is larger for  $b_{n,m}^i$  ( $a_{n,m}^i$ ).

Table 2.1: Maximum errors over  $n$  and  $m$  for the incident multipole coefficients. For all four combinations of scatterer and position, the coefficient type that results in the largest error is marked in bold.

Scatterer	P1		P2	
	$\max \epsilon_{n,m}^{a,(s)}$	$\max \epsilon_{n,m}^{b,(s)}$	$\max \epsilon_{n,m}^{a,(s)}$	$\max \epsilon_{n,m}^{b,(s)}$
No (s) = (i)	-30.5	<b>-28.1</b>	-47.8	<b>-36.0</b>
Yes (s) = (in)	<b>-25.2</b>	-31.3	<b>-22.9</b>	-26.9

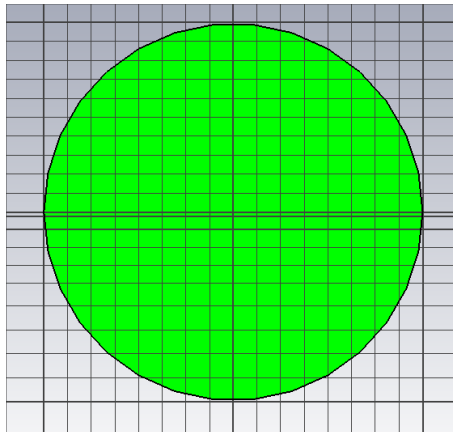


Figure 2.6: Mesh for the scatterer in CST simulations.

## 2.4 Conclusion and future developments

The proposed method, based on the dyadic Green's function and the equivalence principle, is feasible even when the classical approach based on the VSMF translation formulas is not applicable. This feature allows us to reduce the distance between the antenna and the scatterer. The proposed method is compared with the numerical results provided by CST, showing good agreement for the magnitude of the coefficients greater than  $1 \text{ V m}^{-1}$ .

As the next step, it is of interest to solve the full scattering problem by comprising the interaction between different subdomains. Although the theoretical treatment is provided in Subsect. 2.2.3, it must be implemented numerically and the accuracy must be verified. Eventually, it would be great if the proposed method were integrated into a commercial electromagnetic FWS. This would demonstrate the effectiveness of the proposed method.



# Chapter 3

## New easy-to-implement application programming interfaces

### 3.1 Introduction

Application programming interfaces (APIs) are tools to interface programs [56,57]. In particular, full-wave simulations are often used in applied electromagnetism and microwave engineering. On the one hand, these simulations require dedicated software to deliver reliable results. On the other hand, data analysis and processing are usually performed in a numeric computing environment (NCE) such as MATLAB [58] and Python [59] since it is more flexible in handling data for post-processing. To smoothly interconnect a NCE and a FWS, many APIs have been developed. MATLAB is interfaced with HFSS [60] in [61–64] and with FEKO [65] in [56,57]. Python, which is now widely used in the microwave community [66,67], is also used to launch and control FWSs [68,69].

Two common commercial FWSs, CST and HFSS, have recently added built-in APIs with Python (Fig. 3.1), thus showing interest in seamless integration. Interface with CST is also possible through the OLE Automation server. For ANSYS, the company owner and developer of HFSS, the integration of the API inside HFSS is part of a wide and ambitious project called PyAnsys [70]. This provides Python interfaces also to other ANSYS packages. Being open source, Python is preferred over MATLAB.

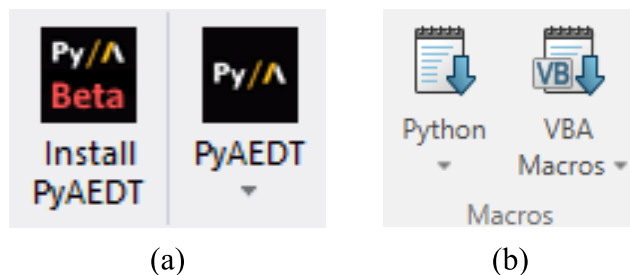


Figure 3.1: Python interfaces in: (a) HFSS; (b) CST.

The above-mentioned APIs require the user to script each command of the HFSS model in Python, IronPython, or visual basic for applications (VBA) languages. This is painful because it is prone to error and, for each operation, one must know the corresponding command and syntax, although a function inside HFSS can register the actions executed by the user [62]. Not least, learning a new programming language may be tough [71].

To overcome this drawback, a new API has been developed [14], which introduces a novel paradigm. According to this, the designer builds the computer-aided design (CAD) model in HFSS and then this is made *scriptable*, that is, the variables can be updated, the model simulated and the results exported directly in the NCE. In other words, the new paradigm is based on the following steps: first, the designer builds the model without VBA scripts through the graphical user interface of the FWS; second, the model variables are varied within any NCE and simulations are run. With this novel paradigm, the designer does not need to know the correspondence between the FWS commands and the scripting language, thus simplifying the API.

The novel API was introduced in [14]. However, that version still required the designer to perform some steps manually, hence limiting the flexibility of the API itself. This drawback has been solved in [72, 73] by automatically recognizing the variables that define the model and substituting them with placeholders. This truly reduces pain in the initial setting of the API. In the following, the latest versions [74, 75] of the API are described.

This chapter is organized as follows. The proposed API with the required steps and files is described in Sect. 3.2. The application of the API to a design example is reported in Sect. 3.3. Eventually, in Sect. 3.4 conclusion is drawn and an outlook on future developments is given.

## 3.2 Methods

The flow chart of the API is shown in Fig. 3.2. The files required by the API and those created by the API itself are listed in Table 3.1 and 3.2, respectively. The file `HFSS_API.py` or `HFSS_API.m` is run (according to the NCE being used) as a first step. The file `base.aedt` is read as an ASCII file, and the numerical variables that define the model are substituted with unique placeholders (number-letter-number-letter in this case, but other compositions are possible, provided that the uniqueness is guaranteed). The output of this first step is summarized in block 1 of the flow chart of Fig. 3.2. In this preliminary step, even the file `ExportToFile.py` is created. When run, it exports the results from HFSS.

As the next point, the updated variable combinations are generated in the NCE (block 2) according to the design technique being considered, e.g., hierarchical optimization. Once the updated variable combination is available, the API reads the `base.txt` file, substitutes the placeholder with the

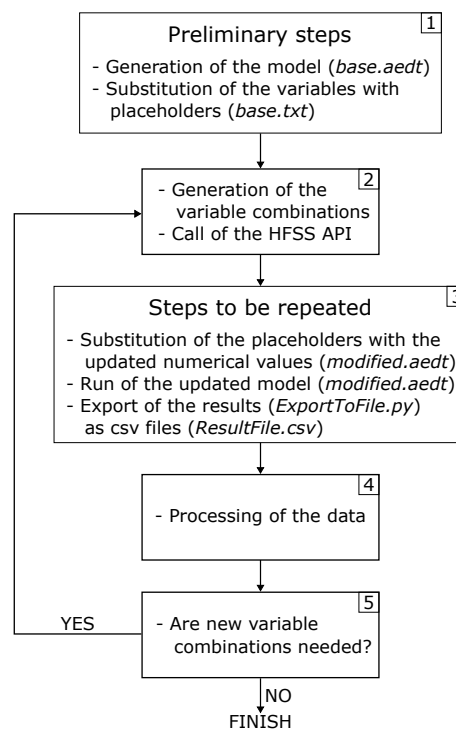


Figure 3.2: Flow chart of the proposed API (Adapted from [14] Creative Commons Attribution-Non Commercial 4.0 International).

Table 3.1: Files needed to run the APIs.

Filename	Description
<code>HFSS_API.py</code>	Python script running the API
<code>HFSS_API.m</code>	MATLAB script running the API
<code>base.aedt</code>	Model to simulate

Table 3.2: Files generated by the APIs.

Filename	Description
<code>ExportToFile.py</code>	Script for result exportation
<code>base.txt</code>	Model with placeholders
<code>modified.aedt</code>	Model with updated variables
<code>ResultFile.csv</code>	Exported results

actual updated variable combination, writes the file `modified.aedt`, and runs the simulation using the HFSS executable file. At this point, the NCE waits to receive back the control once the simulation is finished. Then, the file `ExportToFile.py` is run too, and the desired results are exported as *csv* files, e.g., `ResultFile.csv` (block 3). At this point, the results are processed in the NCE as dictated by the design strategy used (block 4). The three steps in blocks 2, 3, and 4 are repeated until the design strategy is over. This is indicated by the decision question in block 5.

For brevity, the MATLAB and Python commands implementing the above steps are not reported. The interested reader finds them in [14, 72, 73].

### 3.3 Results and discussion

In Fig. 3.3, extracts of the files `base.aedt` and `base.txt` are reported. They show the difference before and after the substitution of the placeholders. According to the internal use of HFSS, variables are subdivided into:

1. `VariableProp` for project variables;
2. `VariableProp` for design variables;
3. `PostProcessingVariableProp` for design variables.

```

$begin 'GlobalVariables'
  VariableProp('$epsR', 'UD', '', '2.2')
$end 'GlobalVariables'
[...]
$begin 'Properties'
  VariableProp('W', 'UD', '', '60mm', oa(i=false, int=false, Min='30mm',
  VariableProp('ts', 'UD', '', '1.6mm')
  VariableProp('d', 'UD', '', 'M/2-b')
  [...]
$end 'Properties'
$begin 'PostProcessingVariables'
  PostProcessingVariableProp('P1_power_mag', 'UD', '', '1W')
$end 'PostProcessingVariables'

```

(a) **numerical values**

```

$begin 'GlobalVariables'
  VariableProp('$epsR', 'UD', '', '0A0A')
$end 'GlobalVariables'
[...]
$begin 'Properties'
  VariableProp('W', 'UD', '', '0B0Bmm', oa(i=false, int=false, Min='30mm')
  VariableProp('ts', 'UD', '', '0D0Dmm')
  VariableProp('d', 'UD', '', 'M/2-b')
  [...]
$end 'Properties'
$begin 'PostProcessingVariables'
  PostProcessingVariableProp('P1_power_mag', 'UD', '', '1D1D')
$end 'PostProcessingVariables'

```

(b) **placeholders**

Figure 3.3: Definitions of the variables in the files defining the HFSS model: (a) before the substitution of placeholders in `base.aedt` (nominal values); (b) after the substitution of placeholders in `base.txt` (Adapted from [72] ©2024 IEEE).

Despite the different definitions, the variables are treated without distinction by the API since all of them are defined by a proposition ending with `VariableProp`.

The API has been illustrated through the design of a patch antenna in [14, 72] and the design of a dual-band resonator in [73]. In addition to these examples, the API has been widely used by the author in [18] to perform a parametric sweep, in [15, 76, 77] for hierarchical optimization, in [78] to tune patch antennas to resonance in a space mapping framework, and in [79] for design optimization. Next, the example of the patch antenna is reported.

The patch antenna is shown in Fig. 3.4. The antenna parameters are as follows. The width of the microstrip for a  $50\ \Omega$ -characteristic impedance is  $M = 4.943$  mm. The distance between the patch and the sides of the substrate is  $L_e = 8$  mm, and the length of the  $50\ \Omega$ -microstrip is  $L_m = 10$  mm. In the following, only the parameters  $a$ ,  $b$ ,  $c$ ,  $W$ , and  $L$  are variable; the others remain fixed. To explore all the study cases,  $d = M/2 - b$  is a dependent variable equal to half the width of the microstrip line entering the antenna at  $y = L_m + a$ . Hierarchical optimization has been carried out to make

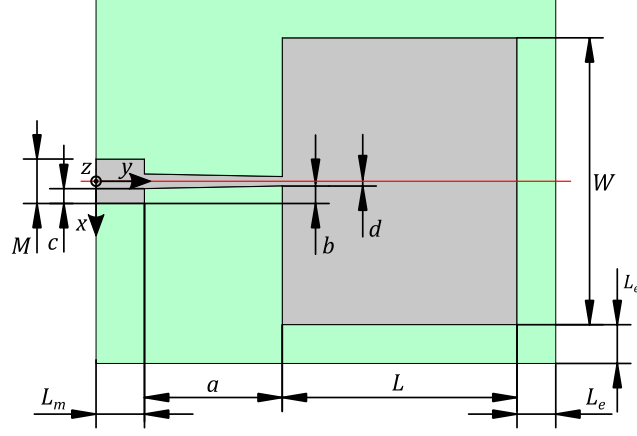


Figure 3.4: Patch antenna with dimensions. The gray and green areas represent the metallization and the substrate, respectively. The substrate-metallization interface is located at the plane  $z = 0$ . The plane  $x = 0$  is a plane of symmetry (Adapted from [14] Creative Commons Attribution-Non Commercial 4.0 International).

the antenna resonate at the frequency of interest, Opt. (i), and improve matching, Opt. (ii) (Opt. stands for optimization). The results are reported in Fig. 3.5. At first, a simple yet intuitive analytical design approach is pursued based on analytical formulas [80]. However, the antenna does not resonate at the intended frequency (blue curve). Then, the patch length  $L$  (Fig. 3.4) is varied to tune the antenna to the desired frequency. Eventually, the other parameters,  $a$ ,  $b$ ,  $c$ , and  $W$ , are varied to improve the matching. Formally, the two optimizations are

$$\begin{cases} \min_L (f_r - f_0)^2 & \text{Opt. (i)} \\ \min_{a,b,c,W} |S_{11}|_m & \text{Opt. (ii)}, \end{cases} \quad (3.1)$$

where  $f_0 = 2$  GHz is the design target frequency, and

$$f_r = \underset{f}{\operatorname{argmin}} |S_{11}| \quad (3.2a)$$

$$|S_{11}|_m = \min_f |S_{11}| = |S_{11}(f_r)|. \quad (3.2b)$$

The variable history for the hierarchical optimization is listed in Table 3.3. After the start guess from analytical formulas, the antenna is first tuned to resonance, Opt. (i), and second the matching is improved, Opt. (ii).

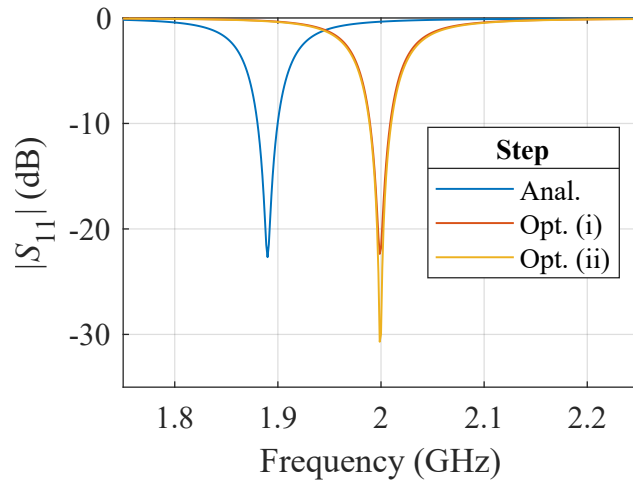


Figure 3.5: Magnitude of  $S_{11}$  for the patch antenna. In the legend, Anal. stands for analytical. Data from [14].

Table 3.3: Variable history for the hierarchical optimization (dimensions are in millimeters, abbreviation a.a. stands for as above).

	Variables				
	$L$	$W$	$a$	$b$	$c$
min	46	57	26	1.500	1.500
max	50	61	32	2.370	2.370
Anal.	49.830	59.290	28.510	2.070	2.070
Opt. (i)	48.472	a.a.	a.a.	a.a.	a.a.
Opt. (ii)	a.a.	59.225	28.440	2.014	1.999

The improvement of the matching does not affect the resonant frequency and therefore is not required to re-tune the antenna to resonance after Opt. (ii). If a re-tuning had been needed, then optimization Opt. (i) would have been launched again. Notwithstanding the simplicity of the design approach, in HFSS, no tool is available that performs the aforementioned steps. Then, tedious and error-prone switches between HFSS and the NCE would be required without an API.

After the antenna is designed, the feeding power is varied to perform studies on the electric field intensity. This analysis is performed in post-processing, thus not requiring a new simulation of the model. It is par-

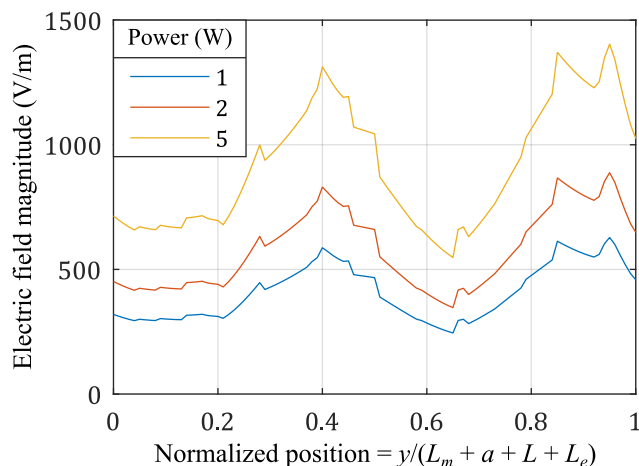


Figure 3.6: Electric field magnitude along the red line in Fig. 3.4. In the  $z$ -direction, the distance from the substrate is 15 mm. The horizontal axis is normalized to the length of the substrate  $L_m + a + L + L_e$ . Data from [73].

ticularly useful for estimating the direction of arrival [81] and serves as a comparison to near-field measurement [82]. The magnitude of the electric field is reported in Fig. 3.6. The maxima of the electric field intensity are at the patch edges. Moreover, because of the linearity of the system, the curves for the electric field intensities are linearly scaled according to the square root of the input power.

### 3.4 Conclusion and future developments

Novel APIs have been introduced and described through an example. The APIs are based on a novel paradigm in which the designer draws the CAD model using the graphical user interface and the model is made scriptable. This approach makes the proposed API fast to apply and user-friendly.

A next step would be to integrate the proposed API into commercial FWSs. In addition, it is of interest to adapt the API to run simulations in parallel to accelerate the design strategy. Eventually, it would be great to extend the proposed approach to other software, even not encoded in ASCII or not related to applied electromagnetism and microwave engineering. Regarding the latter point, the author applied this approach to the general particle tracker software [83] within the framework of the research activity [84].

**Part II**

**Microwave Engineering**



# Chapter 4

## Innovative compact microwave filters and diplexers

### 4.1 Introduction

Filters and diplexers are common in microwave networks [85–87]. They are used to filter and route guided signals according to their frequency spectrum. Due to more stringent requirements in modern systems, it is always at a premium to improve filters and diplexers, for instance, in terms of compactness, loss, and attenuation. Not least, the trend nowadays is to integrate the filtering networks with other components, such as twists and bends [88] or antennas (“filtennas”) [89], and to avoid the use of isolators (reflection-less filters) [90]. A wider overview of past work and an insight into future trends in microwave filters are given in [91–93].

Filter design is divided into two main areas: response synthesis [94–96] and implementation [85,92]. Only the latter has been addressed. Implementation strongly depends on technology. Several technologies are available, depending on the specifications. Common ones are waveguide, dielectric resonator, coaxial, microstrip [85]. Research has focused on the last two technologies and deals with the analysis of innovative end couplings in coaxial cavity filters and the design of compact low-loss diplexers.

The chapter organization follows. In Sect. 4.2, the designs of L-band combline cavity filter and diplexer and two microstrip diplexers are outlined. The next Sect. 4.3 presents and discusses the results. Eventually, in Sect. 4.4 the conclusion is drawn and future developments are described.

## 4.2 Methods

### 4.2.1 Coaxial

Coaxial filters and diplexers support high power before breakdown and their behavior is close to the synthesized Chebyshev responses. The typical unloaded quality factor of coaxial resonators is between  $2 \cdot 10^2$  and  $3 \cdot 10^3$  [97]. Coaxial filters are narrow bandwidth usually, that is, fractional bandwidth (FBW) up to about 20% [92, 98], but no precise limit is fixed. They are modeled with the coupling matrix approach [85] or, in the case of all-pole responses, knowledge of the resonant frequencies of the resonators, the external quality factor, and the coupling coefficient between adjacent resonators is sufficient [98]. The latter approach is a simplified case of the more general one based on the coupling matrix.

The following filter and diplexer are described next:

- L-band filter for E1 Galileo and Iridium;
- L-band diplexer for E1 Galileo and Iridium.

These devices are intended to equip LaBarchettaMagica, a driver to test an autonomous ship for the VELA project [99]. The ship uses the E1 Galileo signal (1559 – 1591 MHz, FBW 2%) for tracking purposes. However, the Iridium satellite communication system works at nearby frequencies (1616 – 1626.5 MHz). Since the two signals are close in the frequency spectrum, the Iridium signal acts as interference for the receiver of the E1 Galileo signal. Therefore, a filter is needed to attenuate the unwanted signal. For this task, a coaxial combline cavity filter is chosen.

#### L-band filter for E1 Galileo and Iridium

The specifications are bandwidth 1559 – 1591 MHz, minimum return loss in passband 19.4 dB (corresponding to 0.05 dB ripple), and at least 40 dB-attenuation in the Iridium frequency bandwidth. Considering a simple all-pole Chebyshev response, the number of resonators to meet the specifications is  $N = 5$  and the derived topology is shown in Fig. 4.1(a). The normalized coupling coefficients,  $m_{i,j}$ ,  $i \neq j$ , are found with standard techniques, and the interested reader can find the details in [15].

From the synthesized response to the physical implementation, standard formulas for the coaxial resonators are used [100]. The filter model and its

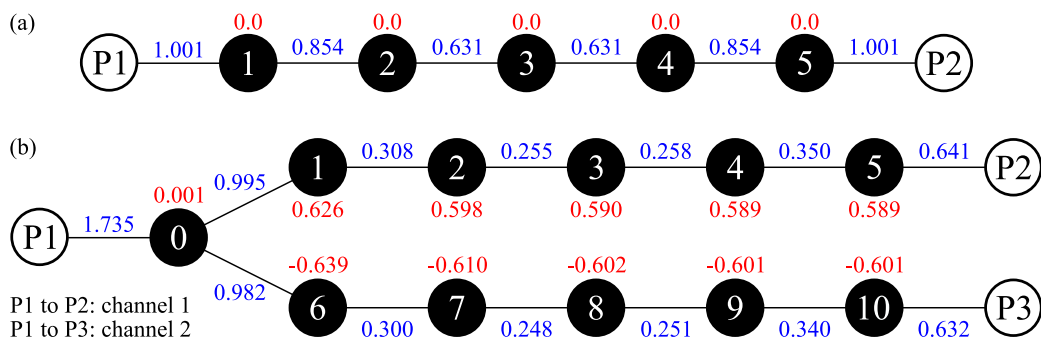


Figure 4.1: Topologies: (a) filter, (b) diplexer. The black (white) circles indicate the resonators (ports). The numbers in red indicate the normalized resonant frequencies  $m_{i,i}$ , while those in blue indicate the normalized coupling coefficients  $m_{i,j}$ . The white numbers identify the resonators (Adapted from [16] Creative Commons Attribution 4.0 License).

dimensions are shown in Fig. 4.2. The technical drawings of the L-band filter are shown in App. B. These have been used for manufacturing by CNC machining.

Research focused on the external coupling between the coaxial cable and the end resonators [15, 76, 77, 101]. In particular, right-angle coaxial-to-rectangular waveguide transitions with inductive and capacitive coupling are investigated (Fig. 4.3). Three right-angle coaxial-to-rectangular wave-

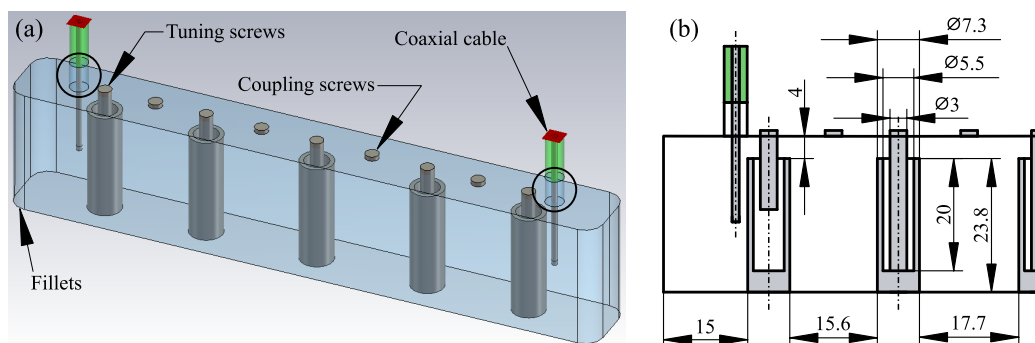


Figure 4.2: Design of the filter: (a) 3D model simulated in CST; (b) technical drawing with dimensions in millimeters. In (a), the extensions inside the circles account for the thickness of the cavity. In (b), only half of the filter is depicted thanks to symmetry. The cavity width is 16 mm and the fillet radius is 4 mm (From [15] Creative Commons Attribution 4.0 License).

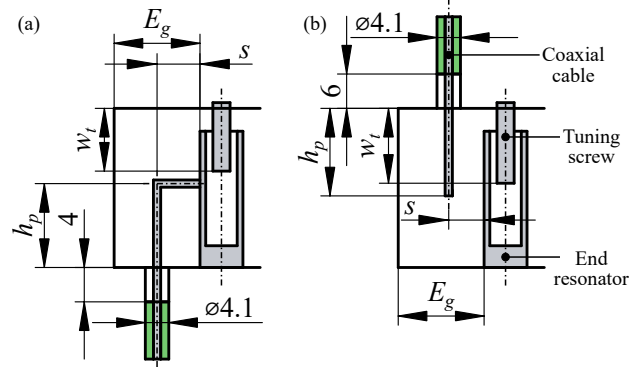


Figure 4.3: Realized end couplings (Adapted from [15] Creative Commons Attribution 4.0 License).

wide transitions with capacitive coupling are numerically investigated [101]. The inductive transition of the same type is instead analyzed numerically in [77]. Transitions with capacitive coupling require neither soldering of the pin nor conductive glue and hence they are easier to manufacture [102]. In addition, the soldering or the use of the conductive glue impacts the realized external quality factor, thus requiring post-manufacturing refinements.

The key parameter that characterizes the external coupling is the external quality factor. In the lossless case, it relates to the group delay as

$$Q_E = \frac{2\pi f_0 \Gamma_d}{4}, \quad (4.1)$$

where  $f_0$  is the center frequency and  $\Gamma_d$  the group delay of  $S_{11}$  at  $f_0$ . The expression (4.1) is valid if the external resonator is tuned to resonance, the other resonators are detuned, and over-coupling occurs [15, 103].

### L-band diplexer for E1 Galileo and Iridium

The specifications for the diplexer are similar to those of the filter: bandwidth 1559 – 1591 MHz for the E1 Galileo channel, 1606 – 1638 MHz for the Iridium channel, minimum return loss in passband 19.4 dB for both channels. The number of resonators per channel is set equal to 5. Considering a resonant star junction to connect the two channels, the topology of the two-channel diplexer is shown in Fig. 4.1(b), along with the nonzero elements  $m_{i,j}$  of the coupling matrix. To obtain the resonant frequencies and the coupling bandwidths from the normalized values, the standard approach is used [104]. The reader is referred to [16] for their numerical values.

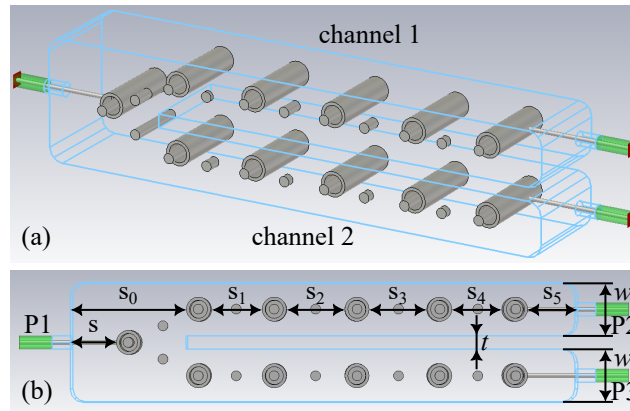


Figure 4.4: Model of the diplexer: (a) perspective and (b) top views. The dimensions in millimeters are: the coaxial resonator inner (outer) diameter is 5.5 and 7.3; the screw diameter is 3; the coaxial cable inner and outer diameters are 1.27 and 4.1. The other dimensions are  $w = 16$ ,  $t = 4$ ,  $s = 13.85$ ,  $s_0 = 34.6$ ,  $s_1 = 16.55$ ,  $s_2 = 17.75$ ,  $s_3 = 17.7$ ,  $s_4 = 15.6$ ,  $s_5 = 15$ . The heights of the tap points from the bottom of the cavity are 18.75 for P1, 6.75 for P2, and 6.90 for P3. The radius of the fillets is 4 (Adapted from [16] Creative Commons Attribution 4.0 License).

The layout of the diplexer is reported in Fig. 4.4. It is similar to the one for the filter in Fig. 4.2 except for the resonant star junction. Unlike the filter, the external coupling is realized by in-line tap coupling. Since the external quality factors for the three ports are different [16], the heights of the coaxial connectors entering the cavity are also different. On the other hand, the resonators of the two channels are identical, and the different resonant frequencies are obtained by adjusting the tuning screws.

## 4.2.2 Microstrip

Microstrip technology is preferred in applications that require compactness and lightweight [85]. The typical unloaded quality factor of the microstrip resonators is between  $5 \cdot 10^1$  and  $2 \cdot 10^2$  [97], thus they are lossier compared to coaxial cavity resonators. Hence the quest for lower-loss microstrip resonators was pursued. Starting from the spiral resonators introduced in [105] and further developed in [106], two diplexers based on complementary spiral resonators have been investigated. Rectangular spiral elements are also used

in [107, 108]. They can be used as defected ground structures [109]. However, a single-layer realization is sought because it is easier to realize. The physical mechanisms behind the spiral resonators are explained in [110, 111].

Two similar devices have been designed to cover different bandwidths: “low” (0.87 and 2.03 GHz), for satellite communications [18], and “high” (2.02 and 3.61 GHz), for personal communications and 5G applications [17].

Regarding the “low” frequency diplexer, a lowpass spiral resonator has been investigated. The technical drawing of this variation is depicted in Fig. 4.5(a). Unlike the lowpass element for the “high” frequency diplexer drawn in Fig. 4.5(b), in this one the spirals depart from two extensions of the central disc, then having an additional degree of freedom. The parametric analysis for this element is carried out in [18], where the physical dimensions of the manufactured diplexer are also reported.

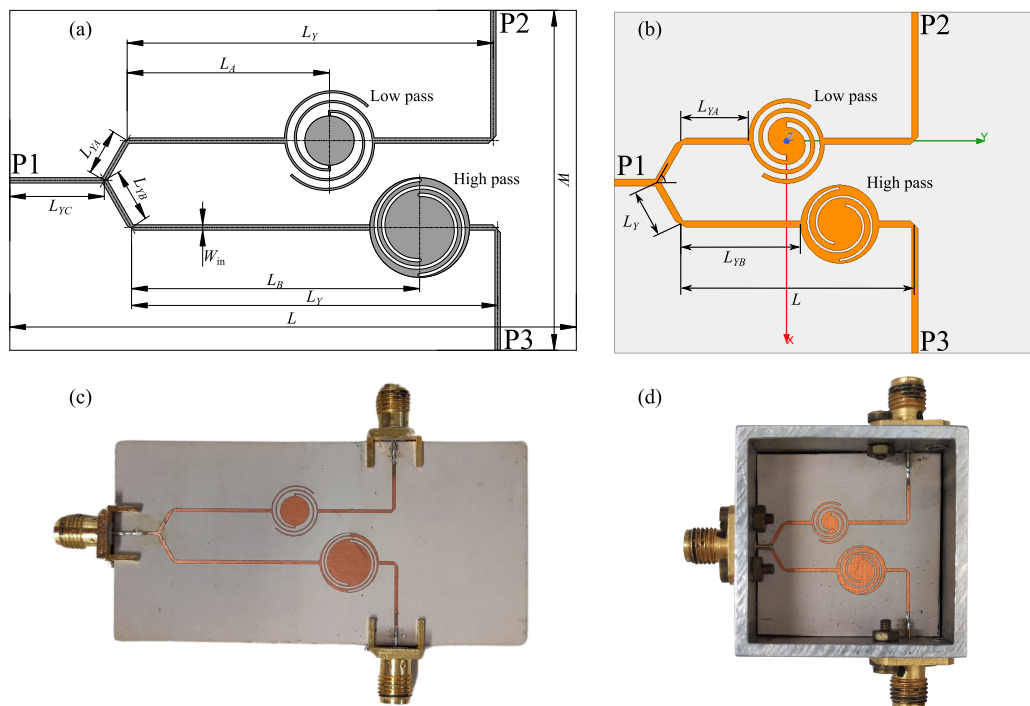


Figure 4.5: Diplexers based on complementary spiral resonators: (a) [(b)] technical drawing for the “low” [“high”] frequency diplexer; (c) [(d)] realized prototype for the “low” [“high”] frequency diplexer (Adapted from [17] ©2024 Wiley Periodicals, LLC. and [18] Creative Commons Attribution 4.0 License).

Based on the spiral passband element presented in [105], a diplexer is proposed. To this aim, a lowpass element is introduced. This is also based on spirals, but is complementary to the one in [105]. The two spiral resonators and their assembly are depicted in Fig. 4.5(b). A nonresonating Y-junction connects the two channels. For details on the physical dimensions, the reader is referred to [17].

It is worth noticing that for both diplexers in Fig. 4.5(a) and (b) is difficult to figure out an equivalent topology as those in Fig. 4.1 for the coaxial combline cavity filter and diplexer. Certainly, the proposed resonators cannot be modeled with an all-pole topology since transmission zeros appear in the diplexer responses, as shown later. The absence of a topology expressing the resonator behavior makes the synthesis of spiral resonator-based devices harder and the designer is forced to rely on design charts and optimization.

## 4.3 Results and discussion

### 4.3.1 Coaxial

#### L-band filter for E1 Galileo and Iridium

The manufactured filter is shown in Fig. 4.6. The cavity and lid are made of aluminum, the resonators and the screws of brass, and the probes for the external coupling of copper. The probes are soldered to SMA connector with solder cups. Even with the utmost attempts, some nonidealities can be observed in the manufactured probes in Fig. 4.6(d).

The curves for the external quality factor versus the pin height are shown in Fig. 4.7, where measured and simulated results are compared. Data for  $h_p = 6$  mm for capacitive coupling are missing since for that value there is undercoupling instead of overcoupling [11] and hence (4.1) does not apply. Indicatively, the external quality factor realized by the inductive coupling spans from 10 to 70, and the one by the capacitive coupling from 60 to 600. Then, on the one hand, the capacitive coupling can realize a wider range of values for the external quality factor, but on the other hand, it is more sensitive to manufacturing tolerances. Note that there is a discrepancy between measured and simulated data, probably due to the limited accuracy of simulations and measurement setup. However, both measured and simulated curves follow the same behavior and they have been fitted with interpolating

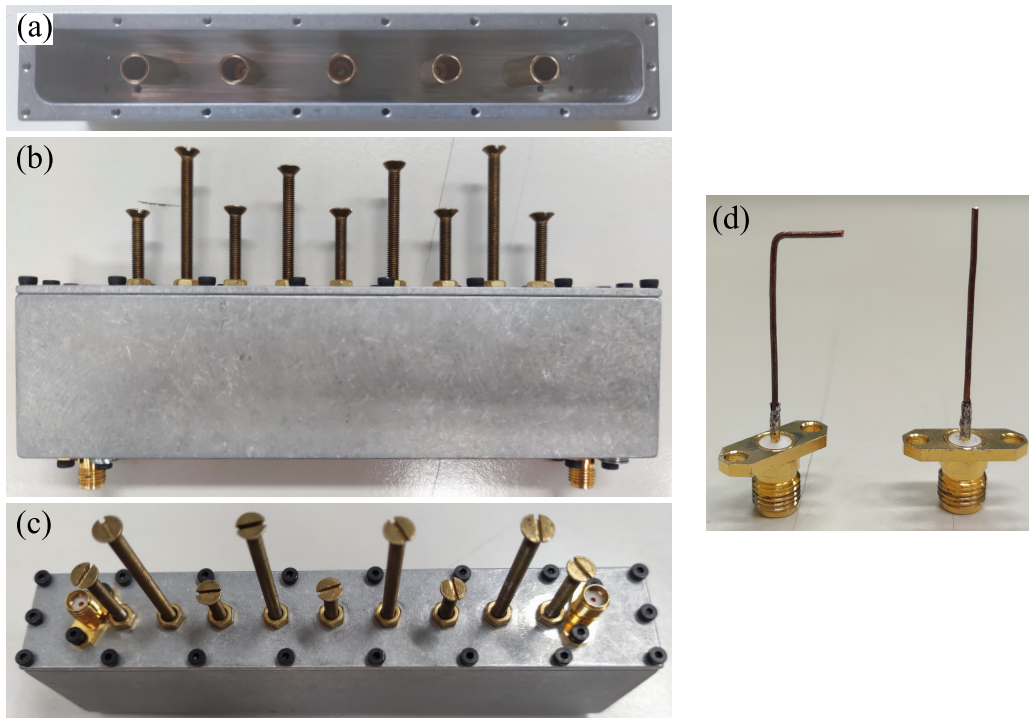


Figure 4.6: Manufactured filter: (a) top view uncovered; (b) lateral view with inductive end coupling; (c) oblique view with capacitive end coupling; (d) instances of two end couplings: inductive (left) and capacitive (right) (Adapted from [15] Creative Commons Attribution 4.0 License).

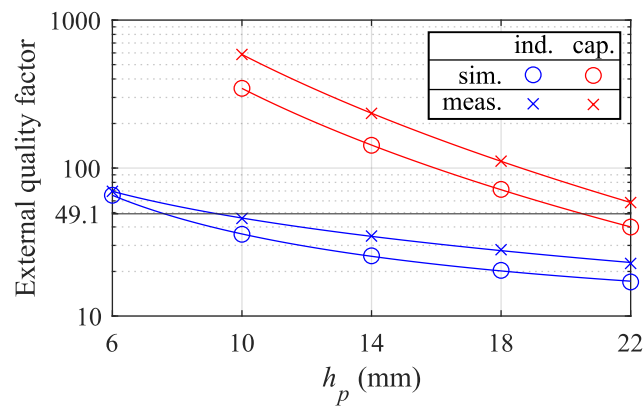


Figure 4.7: External quality factor versus the pin height. In the legend, sim. stands for simulations, meas. for measurements, ind. for inductive, and cap. for capacitive. Solid lines indicate the fitting curves [15]. Data from [15].

curves [15], also reported in Fig. 4.7.

The simulated maximum phasor amplitude for the electric field and the surface current at the center frequency are shown in Fig. 4.8. As expected, the electric field is more intense for the capacitive end coupling and the current density is more intense for the inductive end coupling. However, neither field vanishes for both types of end couplings. Indeed, the term capacitive/inductive indicates only the coupling type that is more relevant, but

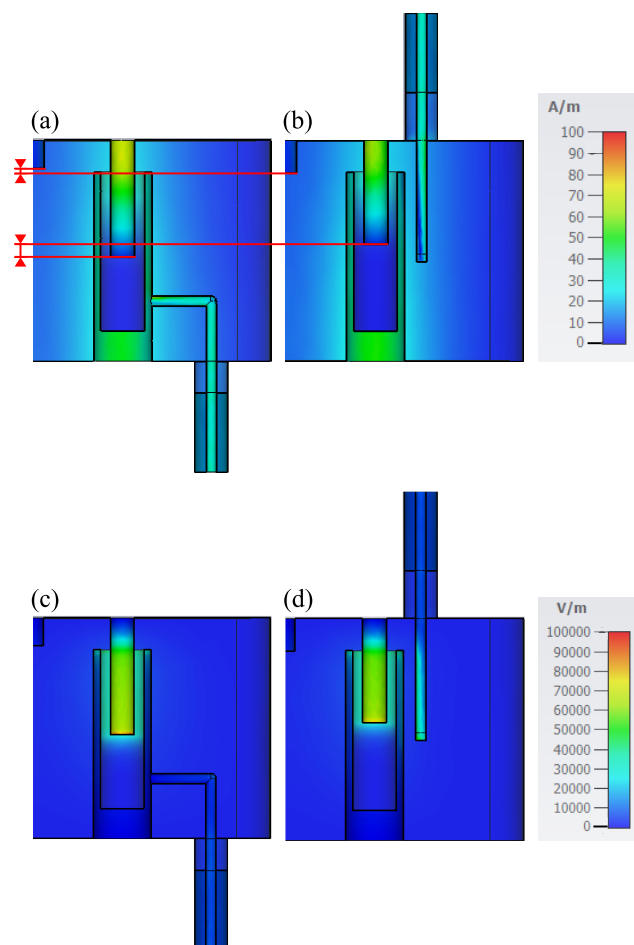


Figure 4.8: Maximum phasor amplitude at the center frequency: (a) [(b)] the current density for the inductive [capacitive] coupling; (c) [(d)] electric field for the inductive [capacitive] coupling. In (a) and (b), the straight red lines underline the different penetrations of the tuning and coupling screws (Adapted from [15] Creative Commons Attribution 4.0 License).

both are present. The different types of end couplings also require different screw penetrations, as highlighted by the red lines in Fig. 4.8(a) and (b).

The responses of the L-band filter for the E1 Galileo bandwidth are shown in Fig. 4.9(a) and (c). The measured responses for both end couplings are close to the synthesized response. Some deviations appear for the capacitive end coupling in the passband, but they are probably due to a coarse tuning of the filter. The insertion loss at the center frequency is 1.72 dB (1.53 dB) for the inductive (capacitive) end coupling. The measured average unloaded quality factor of the resonators is  $8 \cdot 10^2$ .

The filter has also been tuned to the Iridium bandwidth and the corresponding measurements are shown in Fig. 4.9(b) and (d). In this case, too, there is good agreement between the measured and synthesized data, and the small discrepancy for the capacitive coupling is no longer present.

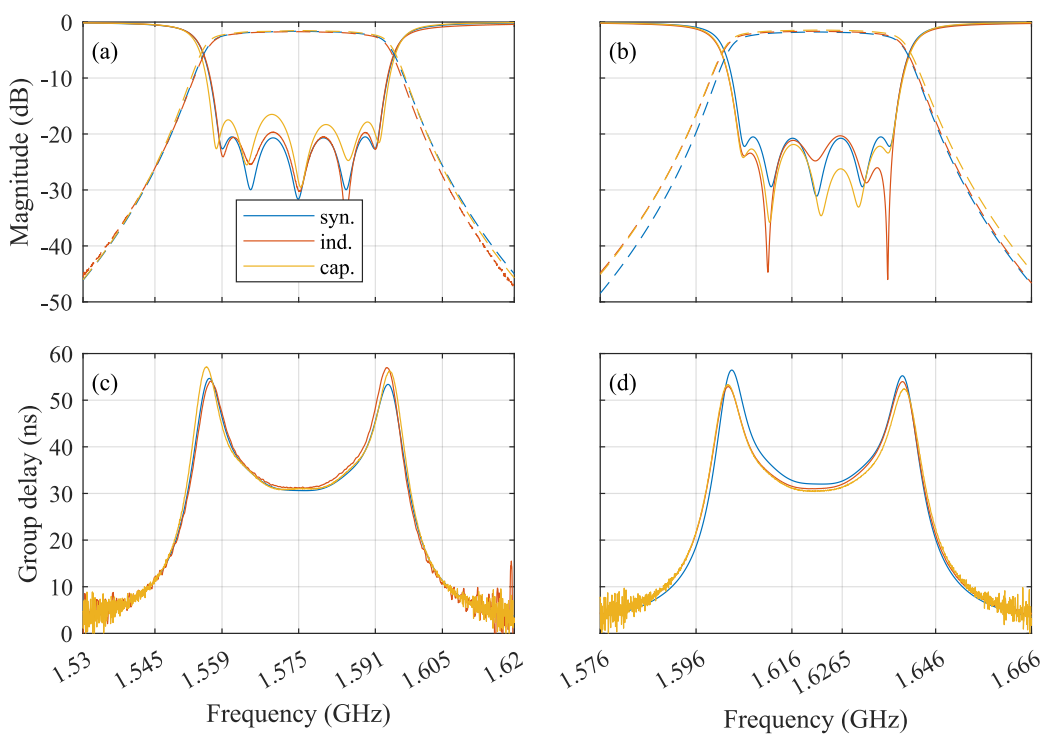


Figure 4.9: Lossy synthesized (syn.) and measured filter responses considering inductive (ind.) and capacitive (cap.) end couplings: (a) [(b)] magnitude for the E1 Galileo [Iridium] bandwidth; (c) [(d)] group delay of  $S_{21}$  for the E1 Galileo [Iridium] bandwidth. In (a) and (b), the curves for  $|S_{11}|$  are solid, and those for  $|S_{21}|$  are dashed. Data from [15].

For completeness, data, technical drawings and CAD models for analyzing the filter are available at [112].

### L-band diplexer for E1 Galileo and Iridium

The prototype of the manufactured diplexer is shown in Fig. 4.10. As for the filter, aluminum is used for the realization of the body and the lid and, in this case, even for the resonators. The screws are made of brass and the probes of copper, as for the filter.

After fine-tuning, the diplexer presents the response in Fig. 4.11. Overall, there is good agreement between the synthesized and measured curves, except for the slower decay of  $|S_{21}|$  below the E1 Galileo bandwidth. This is due to the two too deep minima of  $|S_{11}|$  close to the lower passband edge (see chained-function filters [113,114]). In addition, the Iridium bandwidth is narrower than expected. This does not impact the performance since the Iridium signal is completely within the actual bandwidth, even if narrower than the one from the specifications. The measured average unloaded quality factor is 925, leading to 1.65 dB (1.70 dB) of insertion loss for the E1 Galileo (Iridium) channel. The unloaded quality factor for the diplexer resonators is higher than that for the filter resonators since the aluminum conductivity is higher than the brass one. The diplexer dimensions are  $154.1 \times 36 \times 27.8 \text{ mm}^3$  ( $0.810 \times 0.189 \times 0.146 \lambda^3$ ) walls excluded. The normalized volume per resonator is as low as  $47 \lambda^3$  and the ratio between the unloaded quality factor and the normalized volume per resonator is as high as  $19.8 \cdot 10^{-4} \lambda^{-3}$ . These

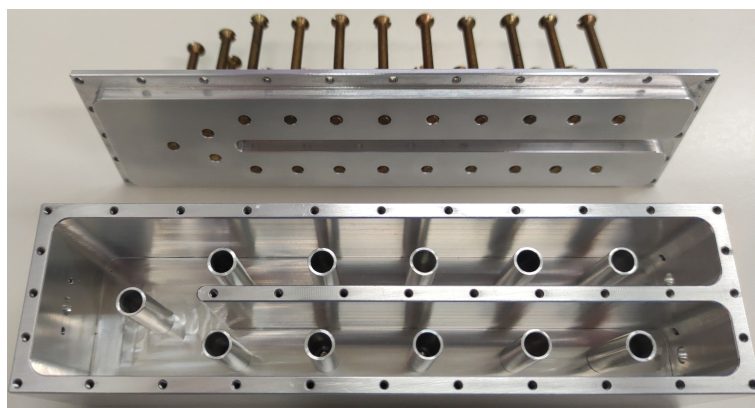


Figure 4.10: Manufactured diplexer, uncovered (From [16] Creative Commons Attribution 4.0 License).

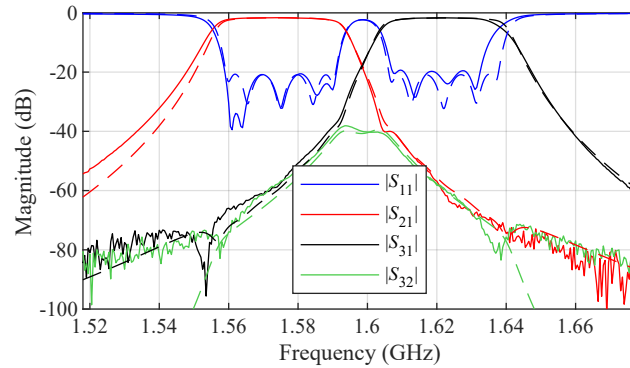


Figure 4.11: Comparison between synthesized (dashed lines) and measured responses (solid lines). Data from [16].

figures make the proposed diplexer highly compact [16].

### 4.3.2 Microstrip

The realized prototype of the “low” frequency diplexer [Fig. 4.5(c)] presents the magnitudes of the scattering parameters depicted in Fig. 4.12(a) and (c). The center frequencies of the channels are 0.87 GHz and 2.03 GHz and are intended for satellite communications. The FBW for the lower (higher) channel is 28.6 % (27.4 %) and the insertion loss for the lower (higher) channel is 0.58 dB (0.66 dB). The dimensions are 19.0 mm × 39.0 mm.

The prototype of the “high” frequency diplexer shown in Fig. 4.5(d) presents the responses reported in Fig. 4.12(b) and (d). The center frequencies of the channels are 2.02 GHz and 3.61 GHz and are intended for personal communication service and 5G applications. The FBW for the lower (higher) channel is 40.6 % (20.2 %) and the insertion loss for the lower (higher) channel is 0.35 dB (0.28 dB). The dimensions are 15.5 mm × 19.5 mm.

As anticipated, transmission zeros appear for the transmission coefficients  $|S_{21}|$  and  $|S_{31}|$  of both diplexers. Unlike the combline cavity filter and diplexer, the measurements for the microstrip diplexers are compared with simulations instead of synthesized responses. Again, this derives from the fact that no topological model for the spiral resonators has been developed yet. Not least, the diplexer masks are far more different from being of Chebyshev type, to which the combline cavity filter and diplexer are instead closer. In addition, microstrip diplexers [17, 18] present a worse spurious response

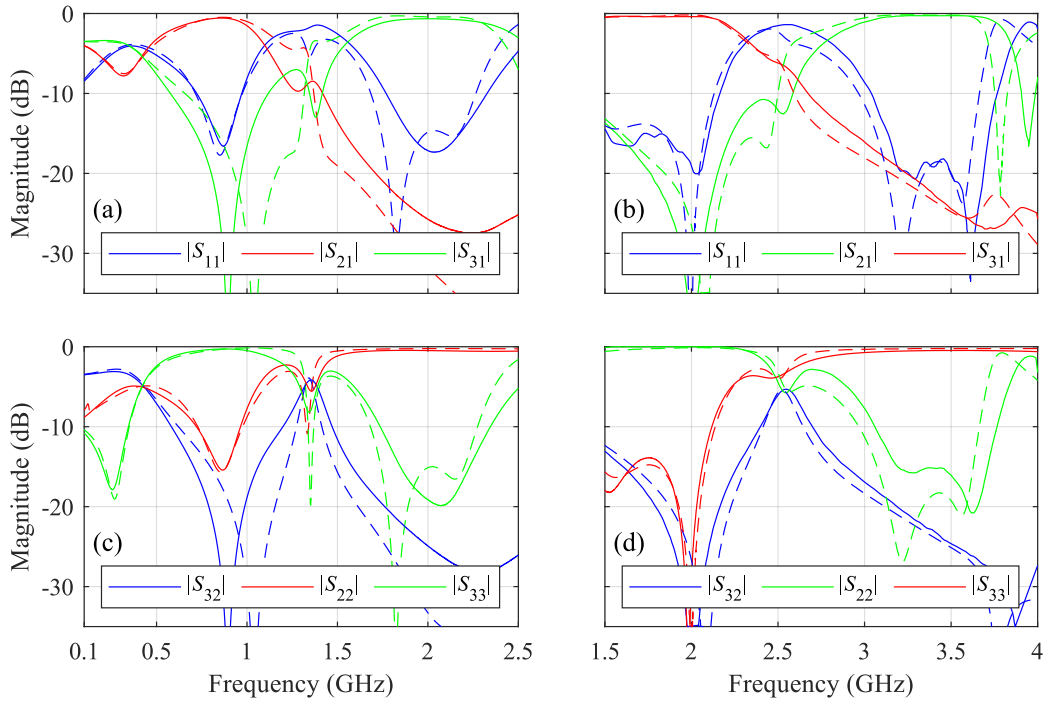


Figure 4.12: Measured (continuous) and simulated (dashed) frequency responses of the prototypes: (a) [(b)]  $|S_{11}|$ ,  $|S_{21}|$ , and  $|S_{31}|$  for the “low” [“high”] frequency diplexer; (c) [(d)]  $|S_{32}|$ ,  $|S_{22}|$ , and  $|S_{33}|$  for the “low” [“high”] frequency diplexer. Data from [17, 18].

compared to combline cavity filter and diplexer [15, 16]. In [17, 18], the realized microstrip diplexers are compared with others from the literature. The proposed spiral resonators are among the most compact ones and the lowest lossy ones, remaining simple to realize as they are uniplanar without vias.

## 4.4 Conclusion and future developments

Research focused on a) the comparison of inductive and capacitive types of end coupling for an L-band combline coaxial cavity filter and the design of a compact L-band diplexer in the same technology; b) the design of two low-loss compact microstrip diplexers based on complementary spiral resonators. For point a), the results show that the capacitive coupling is more sensitive to the wire penetration inside the cavity, despite being easier to manufacture. The two types of end coupling are equivalent from an electrical point of

view since both realize the desired value of the external quality factor. The realized diplexer is compact and presents one of the highest ratio between unloaded quality factor and occupied volume. For point b), we demonstrate the possibility of obtaining a diplexer response by using complementary spiral resonators. In these, the high-pass elements share the same shape and are taken from the literature, while the low-pass elements are different and novel. Both designs result to be compact and with low loss.

As further developments, it would be of interest to:

1. extend the analysis of the external quality factor to multimode cavities;
2. introduce tuning elements to mitigate manufacturing tolerances in the realization of the external quality factor;
3. design a filtenna [89] for L-band applications (E1 Galileo and Iridium). Filtennas directly match the output port of the filter to the input impedance of the antenna, thus avoiding the use of  $50\ \Omega$ -terminations and potentially saving space;
4. develop an equivalent topology modeling nonconventional spiral resonators as the ones presented;
5. design more compact low-loss microstrip resonators with a wide spurious-free bandwidth.

Point 1 is an extension of the analysis of single-mode cavities performed here and is useful in the design of multimode filters that require multimode cavities with each mode excited separately. An example is [115]. Point 2 is of interest since a discrepancy between simulation and measured results has been noticed in Fig. 4.7 and therefore the value obtained by simulations during the design phase may require adjustment once the device is realized. Point 3 derives from the fact that the author has performed a preliminary study on a circularly polarized patch antenna [116] for L-band applications. Then, an antenna directly integrated in the filter would probably lead to a saving of space and less loss since  $50\ \Omega$ -terminations would not be required anymore. Point 4 is important to use well-established techniques for the synthesis of filters and diplexers based on the coupling matrix, thus permitting a more accurate control of the filter response without the need to rely on time-consuming optimizations. Eventually, point 5 is necessary to keep pace with the development of always smaller devices that integrate more systems.

# Chapter 5

## Enhanced asymmetric open TEM cells

### 5.1 Introduction

The transverse electromagnetic (TEM) cells were invented in the 1970s [117]. The basic working principle of TEM cells is to create the largest possible volume of space for the widest bandwidth in which the electric field meets the uniformity criteria of IEC 61000-4-20 [118]. This volume is called uniform test volume (UTV). The first TEM cells were closed, but open TEM cells were also developed to improve accessibility to the UTV. For example, in [119] a lateral wall is removed and in [120] both lateral walls are removed.

Since their introduction, TEM cells have been used in many fields, such as dielectric characterization, probe calibration, electromagnetic compatibility, and electromagnetic interference. Recently, research has focused more on the applications of TEM cells, but there are also papers on the design. For example, in [121] a novel method is outlined to calculate the characteristic impedance of closed TEM cells.

The research described here also deals with the design of TEM cells and focuses on these two points: (a) increase of the size of the UTV while keeping the highest usable frequency [120]; (b) improvement of the impedance matching and consequent reduction of the excitation of higher-order modes that would degrade the field uniformity in the UTV [19]. A third point would be how to further improve impedance matching. An ongoing project on this deals with the manufacturing of a pillar-free TEM. In addition, such a

TEM cell is conceived for in-house manufacturing both for the do-it-yourself community and for a wider use of the TEM cell among practitioners.

The chapter is structured as follows. Sect. 5.2 presents the methodology and Sect. 5.3 shows and discusses the results. Eventually, Sect. 5.4 is concerned with the conclusion and possible future developments.

## 5.2 Methods

Regarding point (a), an asymmetric design is pursued in [120] (Fig. 5.1). An asymmetric TEM cell has a septum that is not halfway between the outer conductors to have a larger UTV while keeping the size of the TEM cell limited [122]. A drawback of pursuing an asymmetric design is that the field is more intense between the septum and the upper conductor, thus limiting the field intensity in the region of interest, namely, between the septum and the lower conductor. The septum in Fig. 5.1 is planar, but nonplanar septa have also been investigated [121].

Referring to Fig. 5.1, the transition from a coaxial cable to a narrow stripline occurs in the feed. In the wide central stripline, the field is more uniform and there the UTV is hosted. Eventually, the taper is responsible

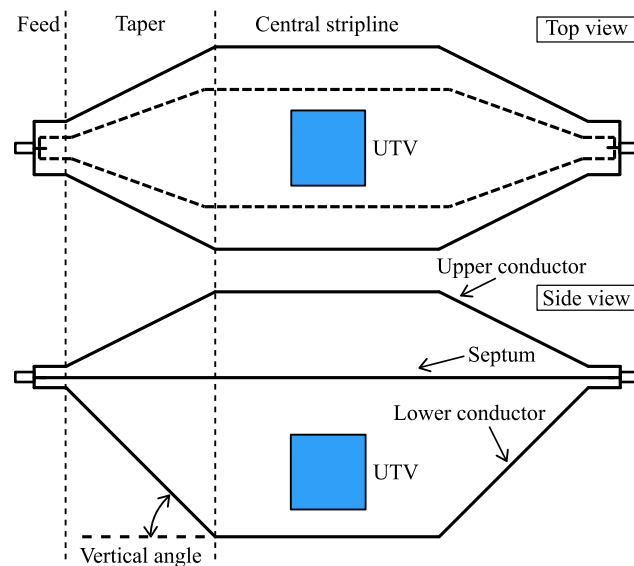


Figure 5.1: Technical drawing of an asymmetric TEM cell (Adapted from [120] ©2022 U.R.S.I. Landesausschuss in Deutschland e.V., Germany).

for a smooth transition between the narrow stripline in the feed and the central stripline, so that the field uniformity does not degrade.

First, the design focuses on determining the dimensions of the TEM-cell cross sections to achieve a  $50\ \Omega$ -characteristic impedance for the striplines in the feed and in the middle. To compute the characteristic impedance of a stripline, the formulas in [123] are used since they represent a good trade-off between accuracy and complexity. Second, the transition between the coaxial cable and the feed stripline is designed. Third, the linear tapers connect the central part and the feeds. To guarantee a good field uniformity, the vertical angle in Fig. 5.1 is as low as  $30^\circ$ . For more details on the design of the TEM cell, the reader is referred to [120]. Thanks to the outlined approach, the UTV is a cube with side 10 cm and the working frequency is from 30 to 1000 MHz, thus covering the CISPR bands C and D [124].

Concerning point (b), the research focused on the tapers, key elements in microwave devices. They connect different parts of the TEM cell with cross sections of different sizes (but same characteristic impedance for the fundamental TEM mode). In particular, the TEM cell requires a taper from a narrow stripline (feed) to a wide one (central stripline).

To improve return loss, a bent profile for the septum is designed (Fig. 5.2). This enforces a  $50\ \Omega$ -characteristic impedance at each  $z$ -cross section, to reduce impedance mismatches. Assuming that the outer conductors are infinitely wide, the characteristic impedance of a stripline is given by [123]

$$Z_c(z) = Z_c(h_s(z), h_t(z), w_s(z), t) \quad (5.1)$$

where, according to Fig. 5.2,  $h_s(z)$  [ $h_t(z)$ ] is the distance between the septum and the lower [upper] conductor,  $w_s(z)$  the septum profile, and  $t$  the septum thickness. The quantities  $h_s(z)$ ,  $h_t(z)$ , and  $t$  are fixed. Then,  $w_s(z)$  is the only degree of freedom. Enforcing a characteristic impedance  $Z_c(z)$  (5.1) equal to  $50\ \Omega$ , the bent septum profile  $w_s(z)$  with  $0\ \text{mm} \leq z \leq l_1$  is obtained. Note from Fig. 5.2 that the linear profile extends from 0 mm to  $l_2 > l_1$ . This is needed to mitigate the impedance mismatching for the linear profile, but it is no longer needed for the bent profile. For further details, see [19].

This solution would virtually permit an infinite return loss if only the desired TEM mode were excited. However, higher-order modes are also present. To account for them, suitable methods, such as the coupling mode method [125, 126], should be adopted. However, the assumption of single-mode propagation turned out to deliver accurate results [19].

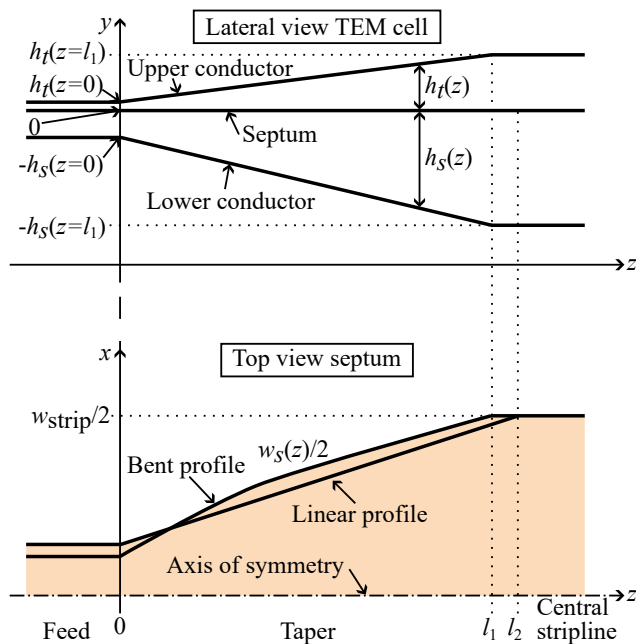


Figure 5.2: Visualization of the design problem for the advanced septum profile (Adapted from [19] Creative Commons Attribution 4.0 License).

### 5.3 Results and discussion

The manufactured TEM cell with the linear septum profile from [120] is shown in Fig. 5.3. The material for the realization cost 500 € [120]. The measured and simulated  $|S_{11}|$  are depicted in Fig. 5.4. The measured  $|S_{11}|$  is slightly greater than the simulated one, but is less than the  $-10$  dB threshold in all the frequency range of interest. The maximum value for  $|S_{11}|$  and the frequency of the maximum are reported in Table 5.1. The frequency of the maximum is quite different between measurements and simulations. The two maxima are in close proximity, and the peaks in the simulations and measurements correspond to separate peaks of  $|S_{11}|$ , accounting for the difference in their frequencies.

For a more extensive and accurate experimental characterization of the TEM cell, the reader is referred to [127] (electric field strength p. 17, unloaded and loaded insertion loss p. 93, field factor p. 94, scattering parameters p. 108, electric field strength p. 111, field requirements p. 112).

Considering the bent septum profile, the linear [120] and bent [19] profiles  $w_s(z)$ , and their difference are depicted in Fig. 5.5. The bent profile is

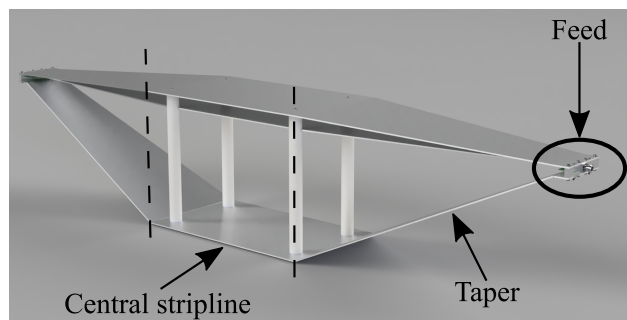
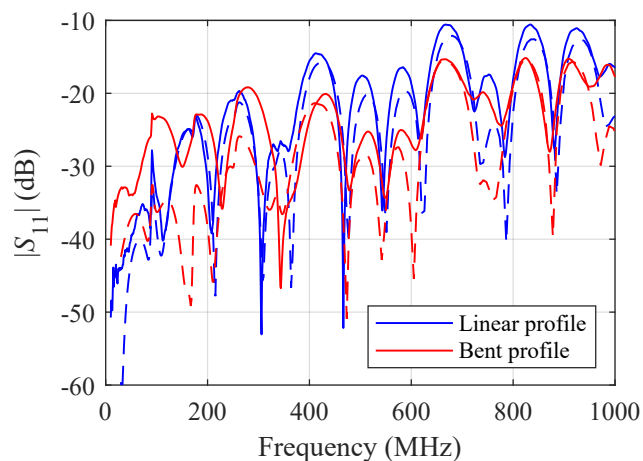


Figure 5.3: Realized TEM cell.

Figure 5.4: Magnitude of  $S_{11}$ : solid (dashed) lines are from measurements (simulations). Data from [19, 120].Table 5.1: Maximum value and frequency of the maximum for  $|S_{11}|$ .

Septum profile	sim./meas.	max $ S_{11} $ (dB)	at (MHz)
Linear	sim.	-12.1	681.1
	meas.	-10.6	834.3
Bent	sim.	-15.3	827.6
	meas.	-15.2	825.0

narrower near the feed, but the two profiles have the same width when they reach the central stripline at the two different  $z$ -coordinates  $l_1$  and  $l_2$ . For details in the computation of  $w_s(z)$ , the reader is referred to [19].

The  $|S_{11}|$  for the TEM cell with a bent profile is shown in Fig. 5.4. Thanks to this improvement, the maximum of  $|S_{11}|$  decreases from  $-10.6$  dB

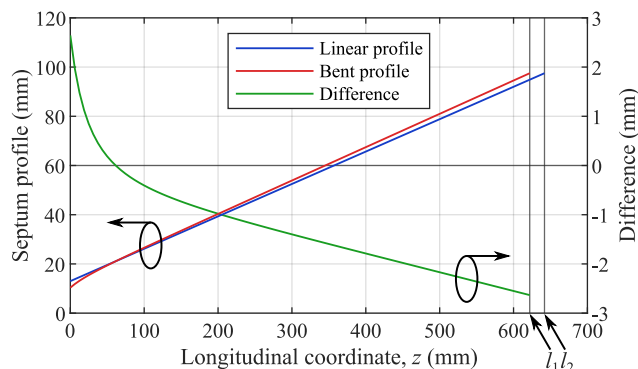


Figure 5.5: Linear and bent profiles, and their difference. The coordinate refers to the septum top view of Fig. 5.2 (Adapted from [19] Creative Commons Attribution 4.0 License).

to  $-15.2$  dB, thus validating both the design and manufacturing. Note from Table 5.1 that there is almost no difference between measurements and simulations for the TEM cell with the bent profile. The deviations between measurements and simulations for  $|S_{11}|$ , particularly noticeable at frequencies below 300 MHz, are due to construction and assembly flaws, and the limited accuracy of the vector network analyzer at low magnitude values [19]. The code and data for the design of the bent septum are available at [128].

## 5.4 Conclusion and future developments

An asymmetric TEM cell with a linear septum profile and a 10 cm-side cube UTV is designed and characterized. The  $|S_{11}|$  is less than  $-10$  dB up to 1 GHz. To improve impedance matching, a simple design technique is described for the tapering of the septum. This technique assumes TEM-only propagation and enforces a constant  $50 \Omega$ -characteristic impedance along the taper, thus obtaining the desired septum profile. The measurements validate the design since the maximum of  $|S_{11}|$  decreases from  $-10.6$  dB to  $-15.2$  dB.

As next steps, it is of interest to consider higher-order modes in the septum design to further improve matching, and characterize the pillar-free TEM cell conceived for in-house manufacturing and mentioned in Sect. 5.1 for a wider spread of the TEM cell among practitioners.

# Chapter 6

## Advanced analysis techniques for closed waveguide devices

### 6.1 Introduction

An introduction on computational electromagnetics has been given in Ch. 2. There, the focus was on open problems. Now, the focus is on closed problems, that is, problems in which the electromagnetic field is confined in a bounded region of space. Many numerical methods are available for the analysis of waveguide problems [30, 129]. Recently, methods based on domain transformation have become popular [130]. An example of domain transformation is transformation optics (TO), also known as transformation electromagnetics. This numerical approach is used to solve waveguide problems with almost arbitrary cross sections [131–133].

Although originally conceived for open problems, the TO has been applied more recently also to closed ones. In [134], TO is applied to solve the eigenvalue problem of arbitrarily shaped 3D perfect electric conductor (PEC) resonators considering a multipole expansion in spherical waves (global-domain basis functions). TO has been applied to solve 2D eigenvalue problems for closed waveguides in [135] for the first time and the method has been refined in [20] by taking care of the exact boundary conditions (BCs) to enforce. Although [20, 135] are limited to 2D eigenvalue problems and [134] to 3D eigenvalue ones, attention has also been drawn to 3D problems with excitation. In [21], waveguide scattering problems with nonsmooth lateral surfaces are analyzed in a mode matching (MM) framework that relies on the

waveguide modes provided by the 2D eigenvalue solver, and in [22], TO combined with hierarchical model reduction and finite element method (FEM) is used to analyze 3D structures with smooth lateral surfaces having circular waveguides (CWs) as input and output ports. The work in [22] is an extension of [136], where devices with smooth surfaces based on the rectangular waveguide are addressed. For the smooth case, the fields in the cross section are solved by resorting to the TO approach, while the longitudinal dependence of the fields is treated by using Lagrange interpolation.

There are many applications for both the 2D eigenvalue solver and the 3D solvers for problems with an excitation. Regarding the former, waveguide modes are needed for the MM analysis, the coupling mode method [125,126], and the analysis of patch antennas in a cavity model framework [78,137,138]. Concerning the latter for nonsmooth devices, MM can solve filters [139] and polarizers [140,141]. Regarding the latter for smooth devices, possible applications are high-power passive components [142], such as polarizers for microwave plasma heating [143,144] and particle accelerator cavities [145]. Furthermore, complex smooth 3D printed devices [146] can also be analyzed.

This chapter is intended to offer a panoramic and comprehensive view of the work of the author on the analysis of closed waveguides. As such, it reviews [20–22,135]. Starting from the 2D case, we move to the 3D case as a straightforward extension. Results are provided to show the accuracy.

The chapter is organized as follows. Sect. 6.2 introduces a unified view of TO as applied to the analysis of guided wave problems. This is followed by Sect. 6.3, which presents and discusses the results of the proposed numerical method and compares it with the results of commercial FWSs and, if available, measurements. The last Sect. 6.4 concludes and provides an outlook on potential future developments.

## 6.2 Methods

The TO theory is now illustrated: domain transformation in Subsect. 6.2.1, enforcement of the BCs in Subsect. 6.2.2, wave equation in Subsect. 6.2.3, field expansions in Subsect. 6.2.4, and eventually the application of MM to modes computed through TO in Subsect. 6.2.5.

### 6.2.1 Domain transformation

A generic waveguide is shown in Fig. 6.1(a). The TO method maps a generic waveguide from an original domain (OD)  $(r', \phi', z')$  to a transformed domain (TD)  $(r, \phi, z)$ . Polar coordinates are preferred here and in the following since they suit better the problems considered. In the OD, the lateral surface of the waveguide  $\bar{\rho}(\phi', z')$  is defined. The function  $\bar{\rho}(\phi', z')$  is a strictly positive single-valued function depending on both the angular  $\phi'$  and longitudinal  $z'$  coordinates and with finite continuous derivatives. The lateral surface is made of PEC. The transformation is

$$\begin{cases} r &= \frac{r'}{\bar{\rho}(\phi', z')} \\ \phi &= \phi' \\ z &= z' \end{cases} . \quad (6.1)$$

The domains of the problem are

$$\Omega_{\text{OD}} = [0, \bar{\rho}(r', \phi', z')] \times [0, 2\pi) \times [0, L] \quad \text{in the OD} \quad (6.2a)$$

$$\Omega_{\text{TD}} = [0, 1] \times [0, 2\pi) \times [0, L] \quad \text{in the TD.} \quad (6.2b)$$

In the TD, the transformed waveguide is a cylinder of radius 1. The lateral surface is of PEC in the TD as well.

The electric and magnetic fields, solution of the Maxwell equations in the OD  $(\mathbf{E}', \mathbf{H}')$  and in the TD  $(\mathbf{E}, \mathbf{H})$ , are related by the Jacobian  $\bar{\bar{J}}$  of the transformation (6.1) as

$$\mathbf{E}' = \bar{\bar{J}}^T \mathbf{E} \quad \mathbf{H}' = \bar{\bar{J}}^T \mathbf{H}, \quad (6.3)$$

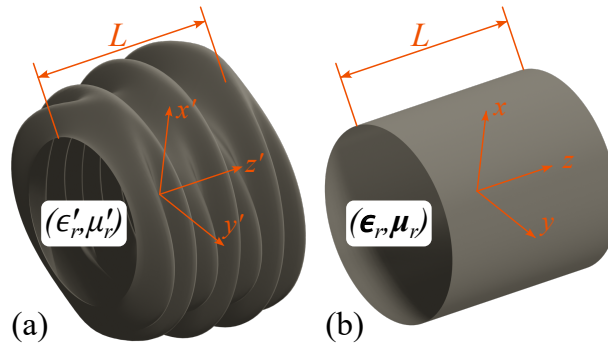


Figure 6.1: Geometric transformation. Device in: (a) OD; (b) TD (From [22] Creative Commons Attribution 4.0 License).

provided that the material parameters are mapped according to

$$\bar{\bar{\epsilon}}_r = \frac{\bar{\bar{J}} \bar{\bar{\epsilon}}'_r \bar{\bar{J}}^T}{\det(\bar{\bar{J}})} \quad \bar{\bar{\mu}}_r = \frac{\bar{\bar{J}} \bar{\bar{\mu}}'_r \bar{\bar{J}}^T}{\det(\bar{\bar{J}})}, \quad (6.4)$$

with  $\bar{\bar{\epsilon}}'_r$  and  $\bar{\bar{\mu}}'_r$  the permittivity and permeability filling the device in the OD and  $^T$  the transpose operator. The material parameters are mapped according to [135]

$$\bar{\bar{\epsilon}}_r = \frac{\bar{\bar{J}} \bar{\bar{\epsilon}}'_r \bar{\bar{J}}^T}{\det(\bar{\bar{J}})} \quad \bar{\bar{\mu}}_r = \frac{\bar{\bar{J}} \bar{\bar{\mu}}'_r \bar{\bar{J}}^T}{\det(\bar{\bar{J}})} \quad (6.5)$$

For simplicity, throughout the paper it is assumed  $\epsilon'_r = \mu'_r = 1$ . Then, (6.5) becomes

$$\bar{\bar{\epsilon}}_r = \bar{\bar{\mu}}_r = \frac{\bar{\bar{J}} \bar{\bar{J}}^T}{\det(\bar{\bar{J}})} \equiv \bar{\bar{\Lambda}}. \quad (6.6)$$

If  $\epsilon'_r$  and  $\mu'_r$  were complex and different from one, the following treatment would remain unchanged, but the simplification (6.6) would not apply.

The matrix  $\bar{\bar{\Lambda}}$  and its inverse are tensors whose expressions are

$$\bar{\bar{\Lambda}} = \begin{bmatrix} 1 + \Xi^2 + r^2 \Pi^2 & \Xi & r \Pi \Psi^{-1} \\ \Xi & 1 & 0 \\ r \Pi \Psi^{-1} & 0 & \Psi^{-2} \end{bmatrix} \quad (6.7)$$

$$\bar{\bar{\Lambda}}^{-1} = \begin{bmatrix} 1 & -\Xi & -r \Pi \Psi \\ -\Xi & 1 + \Xi^2 & r \Pi \Xi \Psi \\ -r \Pi \Psi & r \Pi \Xi \Psi & (1 + r^2 \Pi^2) \Psi^2 \end{bmatrix}$$

being

$$\begin{aligned} \Pi(\phi, z) &= \Pi = -\frac{\partial \bar{\rho}}{\partial z} \\ \Xi(\phi, z) &= \Xi = -\frac{1}{\bar{\rho}} \frac{\partial \bar{\rho}}{\partial \phi} \\ \Psi(\phi, z) &= \Psi = \frac{1}{\bar{\rho}}, \end{aligned} \quad (6.8)$$

where the dependence on  $\phi$  and  $z$  is omitted.

A special case of great interest is the one of uniform cross-section along the longitudinal coordinate. This case was introduced in [135] and refined in [20]. In this case, the analysis is reduced to the 2D cross section, thus

permitting the calculation of the eigenvalues and eigenmodes. The tensors (6.7) then reduce to [20, 135]

$$\bar{\bar{\Lambda}} = \begin{bmatrix} 1 + \Xi^2 & \Xi & 0 \\ \Xi & 1 & 0 \\ 0 & 0 & \Psi^{-2} \end{bmatrix} \quad \bar{\bar{\Lambda}}^{-1} = \begin{bmatrix} 1 & -\Xi & 0 \\ -\Xi & 1 + \Xi^2 & 0 \\ 0 & 0 & \Psi^2 \end{bmatrix}. \quad (6.9)$$

### 6.2.2 Boundary conditions

After the transformation, a simpler geometry is obtained in the TD at the cost of an anisotropic and inhomogeneous permittivity and permeability (Fig. 6.1). However, the problems in the OD and TD are equivalent from a mathematical point of view. In the TD, the waveguide domain is a circular cylinder. Then, it is easier to enforce the BCs. However, these deserve care, as shown in the following.

The device has PEC walls both in the OD and in the TD. Then, it is immediate to fulfill the BCs for the electric field in the TD even if the medium filling the waveguide is anisotropic and inhomogeneous [20]. The BCs are satisfied in the TD if and only if they are satisfied in the OD [22]. Consequently, if a field expansion satisfies the BCs for the electric field in the TD, then the field mapped by (6.3) satisfies the BCs in the OD too. The proof of this statement is given in [22]. The BCs for a PEC wall assume the same expression in both domains

$$\mathbf{i}_n \times \mathbf{E} = 0 \quad \mathbf{i}_{n'} \times \mathbf{E}' = 0, \quad (6.10)$$

where the electric fields are evaluated at the boundary ( $r = 1$  in the TD and  $r' = \bar{\rho}(\phi', z')$  in the OD) and  $\mathbf{i}_n$  ( $\mathbf{i}_{n'}$ ) is the outward unit vector orthogonal to the boundary in the TD (OD). On the contrary, the BCs for the magnetic field assume different expressions in the two domains due to the anisotropy and inhomogeneity of the medium

$$\mathbf{i}_n \times \left( \bar{\bar{\Lambda}}^{-1} \nabla \times \mathbf{H} \right) = 0 \quad \mathbf{i}_{n'} \times (\nabla \times \mathbf{H}') = 0. \quad (6.11)$$

In (6.11),  $\bar{\bar{\Lambda}}^{-1}$  appears in the TD only. An expansion of the magnetic field in terms of the CW modes does not fulfill the BCs (6.11) in the TD and then neither in the OD. As a consequence, correction terms must be added [20], increasing the complexity of the field expansion. The fulfillment of the BCs raises issues in [134, 147] and is overlooked in [136].

### 6.2.3 Wave equation

The vector wave equation for the electric field is

$$\nabla \times (\bar{\mu}_r^{-1} \nabla \times \mathbf{E}) - k_0^2 \bar{\epsilon}_r \mathbf{E} = -j\omega\mu_0 \mathbf{j}_s, \quad (6.12)$$

where  $k_0 = \omega\sqrt{\epsilon_0\mu_0}$  is the free space wavenumber and  $\mathbf{j}_s$  the impressed electric currents at the ports. The weak form formulation [148] of (6.12) is

$$\int_{\Omega_{\text{TD}}} \nabla \times \mathbf{w} \cdot \bar{\Lambda}^{-1} \nabla \times \mathbf{E} d\Omega - k_0^2 \int_{\Omega_{\text{TD}}} \mathbf{w} \cdot \bar{\Lambda} \mathbf{E} d\Omega = -j\omega\mu_0 \int_{S_1 \cup S_2} \mathbf{w} \cdot \mathbf{j}_s dS, \quad (6.13)$$

where  $\mathbf{w}$  are the weighting functions,  $\mathbf{i}_n$  the outward unit vector at the ports ( $\pm \mathbf{i}_z$  in our case), and  $S_1$  and  $S_2$  the surfaces of the two ports in the TD. According to (6.6),  $\bar{\Lambda}$  replaces  $\bar{\mu}_r$  and  $\bar{\epsilon}_r$  in (6.13). A Galerkin framework is applied for discretization (weighting functions  $\mathbf{w}$  equal to the expansion functions, introduced next).

### 6.2.4 Field expansion

#### 2D case

If interested in computing the eigenvalues and eigenmodes of an arbitrarily shaped 2D cross section, no source must be considered in the right-hand side of (6.12) and (6.13), and, assuming a uniform structure along the direction of propagation, the 3D integrals in (6.13) reduce to 2D integrals. In this case, the usual decomposition in transverse electric (TE) and transverse magnetic (TM) modes applies [10]. For the TM modes, the electric field along the longitudinal component  $\mathbf{E}_z$  is expanded over CW modes. For the TE modes, two ways are possible: (a) write an equation for  $\mathbf{H}_z$  and expand it in terms of CW modes plus a correction term accounting for the different BCs; (b) solve the vector wave equation for the transverse electric field  $\mathbf{E}_t$ . Approach (a) is described in [20] and approach (b) is currently under study. For TM modes, the longitudinal component of the electric field  $\mathbf{E}_z$  is expanded as

$$\mathbf{E}_z \cdot \mathbf{i}_z = \sum_{m=0}^M \sum_{n=1}^N [a_{mn} J_m(k_{mn}\rho) \cos(m\phi) + b_{mn} J_m(k_{mn}\rho) \sin(m\phi)], \quad (6.14)$$

where  $k_{mn}$  is the  $n$ -th zero of the Bessel function of the first kind and order  $m$ ,  $J_m(\cdot)$ , and  $a_{mn}$  and  $b_{mn}$  are the weights associated to the basis functions.

Since in the TD the radius of the waveguide is one, expansion (6.14) automatically satisfies the BCs (6.10) according to the definition of zero of a function.

The longitudinal magnetic field component is more complex since straightforward expansion in CW TE modes would not satisfy the BC (6.11). Bases different from those originally exploited in [135] are necessary

$$\mathbf{H}_z \cdot \mathbf{i}_z = \sum_{m=0}^M \sum_{n=1}^N [a_{mn} f_{mn}(\rho, \phi) + b_{mn} g_{mn}(\rho, \phi)], \quad (6.15)$$

with

$$f_{mn}(\rho, \phi) = J_m(k'_{mn}\rho) \cos(m\phi) + r_m(\rho) l_{mn}(\phi) \quad (6.16a)$$

$$g_{mn}(\rho, \phi) = J_m(k'_{mn}\rho) \sin(m\phi) + r_m(\rho) v_{mn}(\phi) \quad (6.16b)$$

and  $k'_{mn}$  the  $n$ -th zero of the derivative of the Bessel function of order  $m$  and  $a_{mn}$  and  $b_{mn}$  are again the weights associated to the basis functions. The functions  $r_m(\rho)$ ,  $l_{mn}(\phi)$ , and  $v_{mn}(\phi)$  are degrees of freedom that allow each term of the expansion to satisfy the BCs (6.11). If  $r_m(\rho)$  or  $l_{mn}(\phi)$ , and  $v_{mn}(\phi)$  vanished, the usual expressions of the CW modes would be recovered. For more details, the reader is referred to [20]. For a numerical implementation, indices  $n$  and  $m$  in (6.14) and (6.15) are limited by  $N$  and  $M$ , respectively.

Substituting the field expansion (6.14) in (6.13) or (6.15) in the dual expression for the magnetic field, the following linear system is obtained

$$(\mathbf{F} - k_c^2 \mathbf{G}) \mathbf{c} = \mathbf{0}, \quad (6.17)$$

where the wavenumber at cutoff  $k_c$  replaces  $k_0$ . The vector  $\mathbf{c}$  in (6.17) contains the weights  $a_{mn}$  and  $b_{mn}$  of expansion (6.14) or (6.15). The matrices  $\mathbf{F}$  and  $\mathbf{G}$  contain the integrals between the basis functions, the weight functions, and the entries of  $\bar{\bar{\Lambda}}$  and  $\bar{\bar{\Lambda}}^{-1}$ . The expressions for  $\mathbf{F}$  and  $\mathbf{G}$  are given in [20].

### 3D case

For 3D devices, the electric field is expanded as

$$\mathbf{E}(r, \phi, z) = \mathbf{E}_t(r, \phi, z) + \mathbf{E}_z(r, \phi, z), \quad (6.18)$$

where subscript  $t$  ( $z$ ) indicates the transverse (longitudinal) component, with

$$\mathbf{E}_t(r, \phi, z) = \sum_{n=1}^{N_{\text{TE}}} \mathbf{e}_{t,n}^{\text{TE}}(r, \phi) \tau_n^{\text{TE}}(z) + \sum_{n=1}^{N_{\text{TM}}} \mathbf{e}_{t,n}^{\text{TM}}(r, \phi) \tau_n^{\text{TM}}(z) \quad (6.19a)$$

$$\mathbf{E}_z(r, \phi, z) = \sum_{n=1}^{N_{\text{TM}}} \mathbf{e}_{z,n}^{\text{TM}}(r, \phi) \zeta_n^{\text{TM}}(z), \quad (6.19b)$$

where  $\mathbf{e}_{t,n}^{\text{TE}}$ ,  $\mathbf{e}_{t,n}^{\text{TM}}$ , and  $\mathbf{e}_{z,n}^{\text{TM}}$  represent the real field maps for TE and TM modes in CWs, as indicated by the superscript, and  $N_{\text{TE}}$  ( $N_{\text{TM}}$ ) the number of TE (TM) modes considered in the expansion. The functions  $\tau_n^{\text{TE}}(z)$ ,  $\tau_n^{\text{TM}}(z)$ , and  $\zeta_n^{\text{TM}}(z)$  in (6.19) express the longitudinal field variation [136] and they are defined as

$$\tau_n^{\text{TE}}(z) = \sum_{l=1}^{N_{l,t}} c_{n,l}^{\text{TE}} \varphi_l(z) \quad (6.20a)$$

$$\tau_n^{\text{TM}}(z) = \sum_{l=1}^{N_{l,t}} c_{n,l}^{\text{TM}} \varphi_l(z) \quad (6.20b)$$

$$\zeta_n^{\text{TE}}(z) = \sum_{l=1}^{N_{l,z}} d_{n,l}^{\text{TM}} \psi_l(z), \quad (6.20c)$$

where  $c_{n,l}^{\text{TE}}$ ,  $c_{n,l}^{\text{TM}}$ , and  $d_{n,l}^{\text{TM}}$  are the degrees of freedom associated to the Lagrange polynomials  $\varphi_l(z)$  and  $\psi_l(z)$ , and  $N_{l,t}$  ( $N_{l,z}$ ) is the number of nodes for the 1D discretization along  $z$  for the transverse (longitudinal) component. The degree of polynomial  $\psi_l(z)$  is one less than the degree of polynomial  $\varphi_l(z)$  [136]. Throughout the article, quadratic (linear) finite elements for the transversal (longitudinal) component are used. For further details, see [22].

Similar to the 2D case, substituting the field expansion (6.19) in (6.13), the following linear system is obtained

$$(\mathbf{A} - k_0^2 \mathbf{B}) \mathbf{c} = -j\omega\mu_0 \mathbf{d}. \quad (6.21)$$

Again, the vector  $\mathbf{c}$  in (6.21) contains the weights  $c_{n,l}^{\text{TE}}$ ,  $c_{n,l}^{\text{TM}}$ , and  $d_{n,l}^{\text{TM}}$  of the expansions (6.19) and (6.20). The matrices  $\mathbf{A}$  and  $\mathbf{B}$ , and vector  $\mathbf{d}$  contain the integrals between the basis functions, the weight functions, and the entries of  $\bar{\bar{\Lambda}}$  and  $\bar{\bar{\Lambda}}^{-1}$ . The expressions for  $\mathbf{A}$ ,  $\mathbf{B}$ , and  $\mathbf{d}$  are given in [22]. Observe the similarity between (6.17) and (6.21), except for the fact that no excitation vector appears in (6.21) and that the cutoff eigenvalue  $k_c$  replaces the free space wavenumber  $k_0$ .

### 6.2.5 Mode matching

Once a numerical tool is available to compute the 2D modes of hollow closed waveguides, the MM technique has been applied to solve guided scattering problems (Fig. 6.2) [21]. To do so, the line-integral formulation of MM [149–152] is applied.

In [21], nothing new about MM is presented, but rather two different approaches, namely the TO to compute the 2D waveguide modes and the line-integral formulation of MM, are applied together for the first time to solve guided-wave scattering problems. Only planar discontinuities orthogonal to the propagation axis of two different semiinfinite waveguides (Fig. 6.2) can be rigorously analyzed by MM. These will be referred to as waveguide steps. Once the generalized scattering matrix [129] of the discrete step is computed, the generalized scattering matrix of the entire device is obtained by cascading the generalized scattering matrices of the step and the delay matrices of the uniform transmission lines [129].

Although smooth transitions may be approximated as small nonsmooth transitions and analyzed through MM [153], this latter approach is more computationally expensive and approximates geometry [22]. Consequently, a specific solution for smooth transitions was sought.

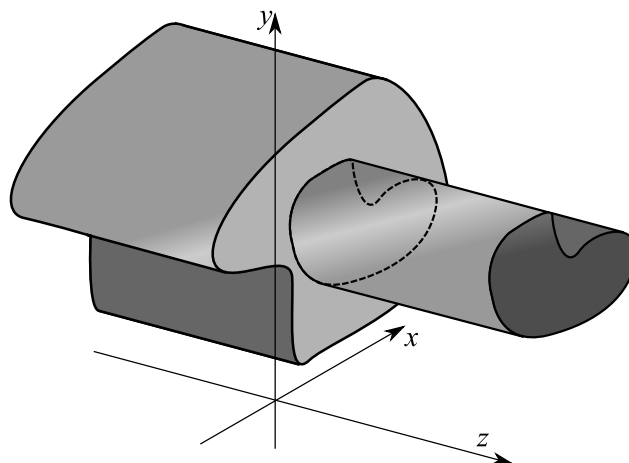


Figure 6.2: Definition of the problem: waveguide single step (Adapted from [21] Creative Commons Attribution 4.0 License).

## 6.3 Results and discussion

### 6.3.1 2D eigenvalue problems

The analysis of a circle with a cut (Fig. 6.3) is performed in [20]. The contour is piece-wise defined and fillets are added to have  $\frac{\partial \bar{\rho}}{\partial \phi}$  continuous. The MATLAB code for this analysis is available at [154].

In Fig. 6.4, the eigenvalues of the proposed method are reported against 2D FEM [155] results for varying the ratio between the length of the cut and the radius of the CW. Due to the symmetry of the cross section with respect to the  $x$ -axis, the sine and cosine terms in (6.14) and (6.15) are orthogonal, hence the distinction between sine and cosine in Fig. 6.4. The agreement between the two methods is excellent. Note that the difference between the eigenvalues for the sine and cosine expansions increases as  $d/R$ . For the error analysis with FEM results, the reader is referred to [20].

### 6.3.2 3D problems with excitation

#### Nonsmooth waveguide devices

For example, the polarizer described in [141] is analyzed with MM resorting to the field maps provided by the highlighted 2D eigenvalue solver. The

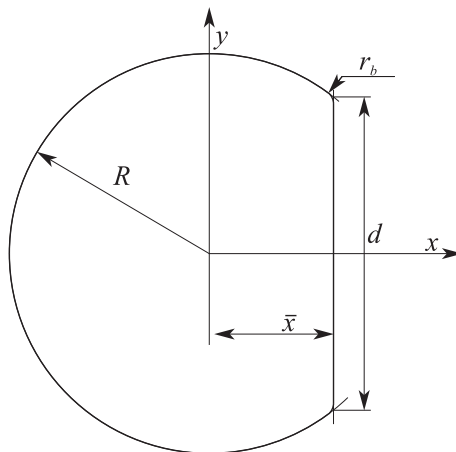


Figure 6.3: Circle of radius  $R$  with a cut at a distance  $\bar{x}$  from its center. Fillets of radius  $r_b$  are added to have a smooth transition (Adapted from [20] ©2022 Wiley Periodicals, LLC.).

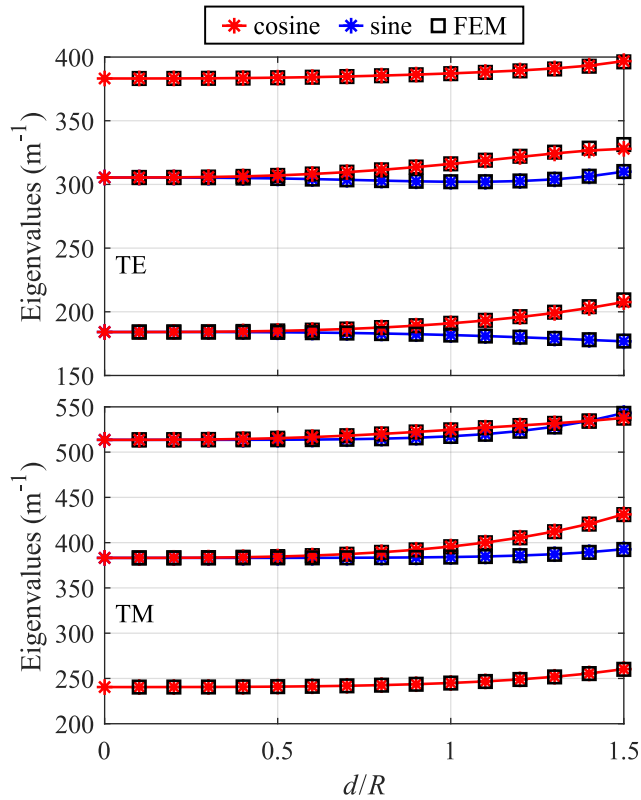


Figure 6.4: Eigenvalues for a circle with a cut (Fig. 6.3). The parameters are  $R = 10$  mm,  $r_b = 1$  mm,  $M = N = 20$ , and the ratio  $d/R$  is varied. Data from [20].

MATLAB code implementing MM is available at [156].

The polarizer in [141] is made up of steps between CW and a CW with two parallel cuts (Fig. 6.5). The two orthogonal polarizations of the CW (Fig. 6.5) undergo different propagation such that their phase difference at the end of the polarizer is  $90^\circ$ . The polarizer operates in the  $Ka$ -band with center frequency  $f_0 = 32$  GHz. The cutoff frequency of the fundamental  $TE_{11}$  modes is 18.73 GHz and the one for the first higher-order mode  $TM_{01}$  is 24.47 GHz.

The results for  $|S_{11}|$  of both polarizations and the phase difference between polarizations for  $S_{21}$  are reported in Fig. 6.6 and compared with FEM results from HFSS. A convergence analysis is carried out for the MM method. The converge analysis is aimed at finding how many modes are needed to deliver accurate results, that is, how many modes should be included in the

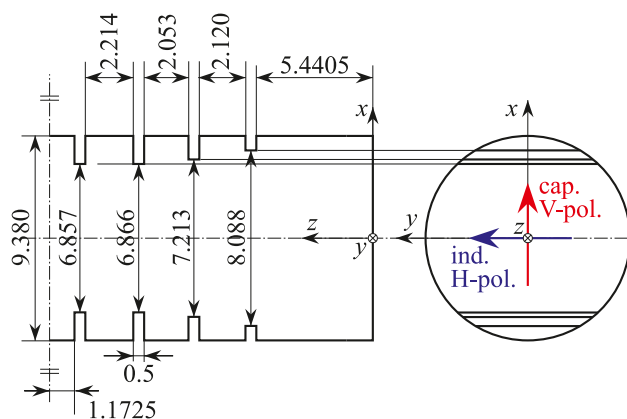


Figure 6.5: Geometry of the polarizer. Since the polarizer is symmetric, only half is shown. The red and blue arrows on the right define the polarizations: red for capacitive (vertical) and blue for inductive (vertical). Dimensions are in millimeters. The total length of the polarizer is 30 mm (Adapted from [21] Creative Commons Attribution 4.0 License).

summation so that all relevant contributions are included. Similar considerations can be extended to the 2D eigenvalue problem and the 3D problem with excitation for smooth waveguide devices. Since the number of modes or basis functions depends on the specific geometry being considered, it is not possible to determine an error estimator for the automatic selection of the number of basis functions. The convergence analysis should then be repeated for each specific geometry, as usually done in commercial FWSs. In this case, the determining parameter for the convergence analysis is  $f_{\text{SPM}}$  and indicates that all modes whose cutoff frequency is less than  $f_{\text{SPM}}$  are considered in the MM analysis. If  $f_{\text{SPM}}/f_0 = 9$ , the results from MM well agree with those from measurements if  $|S_{11}|$  is greater than about  $-40$  dB. Discrepancies below this threshold are due to the limited accuracy of MM and the manufacturing tolerances of the device of the order of  $0.01$  mm [141]. Considering a  $\pm 0.4^\circ$  deviation from the target value of  $90^\circ$ , a 10 % FBW is achieved. For a comparison between the proposed method and HFSS in terms of computation time, the reader is referred to [21].

### Smooth waveguide devices

Now, two phase shifters with smooth lateral surfaces are analyzed for high-power applications. The target frequency bandwidth is the  $Ka$ -band. The

expression for the lateral surface is

$$\bar{\rho}(\phi', z') = R + r \sin^2 \left( \frac{\pi z'}{L} \right) \cos(n\phi'), \quad (6.22)$$

where  $R$  is the baseline radius,  $r$  the offset of the lobes,  $L$  the length of the device, and  $n = 2$  the number of lobes. For  $r/R$  small,  $R + r \cos(n\phi')$

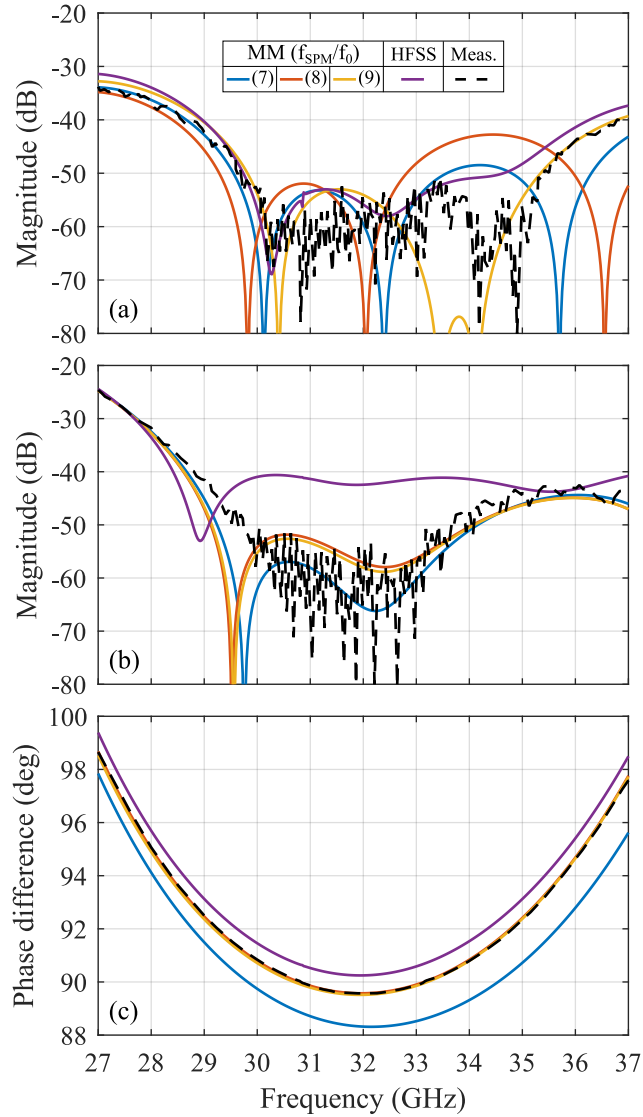


Figure 6.6: Polarizer [141]: (a)  $|S_{11}|$  for TE<sub>11</sub> inductive polarization; (b)  $|S_{11}|$  for TE<sub>11</sub> capacitive polarization; (c) phase difference between polarizations. In the legend, Meas. stands for measurements. Data from [21].

resembles an ellipse [144]. The parameters in millimeters are: ( $s$ , for short)  $R = 5$ ,  $r = 0.917$ ,  $L = 48$ ; ( $\ell$ ,  $\ell$  for long)  $R = 13.895$ ,  $r = 1.99$ ,  $L = 1000$ . Note that the device ( $\ell$ ) is two orders of magnitude longer than the ( $s$ ) one. The input and output CWs for device ( $\ell$ ) are over-moded to reduce loss (the cutoff frequency of the fundamental  $TE_{11}$  modes is 6.32 GHz and the one for the first higher-order mode  $TM_{01}$  is 8.26 GHz).

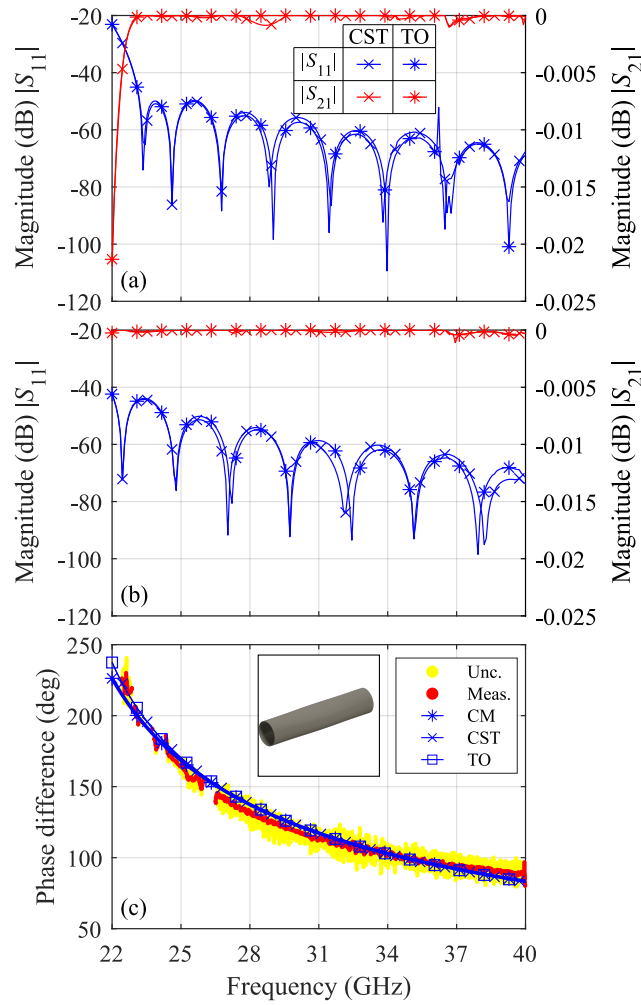


Figure 6.7: Short shifter [144]: (a)  $|S_{11}|$  and  $|S_{21}|$  for  $TE_{11}$  inductive polarization; (b)  $|S_{11}|$  and  $|S_{21}|$  for  $TE_{11}$  capacitive polarization; (c) phase difference between polarizations. In the legend of (c), Unc. stands for uncertainty, Meas. for measurements, and CM for the coupled mode theory used in [144]. Data from [22].

The results of this method are compared with the measured ones from [144] and the numerical ones from CST. The magnitude of the reflection and transmission coefficients and the phase difference are compared with FEM results from CST and the coupled mode theory [144] in Fig. 6.7 for the device ( $s$ ) and in Fig. 6.8 for the device ( $\ell$ ). Only measured results for the phase difference are available from [144]. The orientations of the polarizations are defined as in Fig. 6.5. The methods show strong agreement, especially

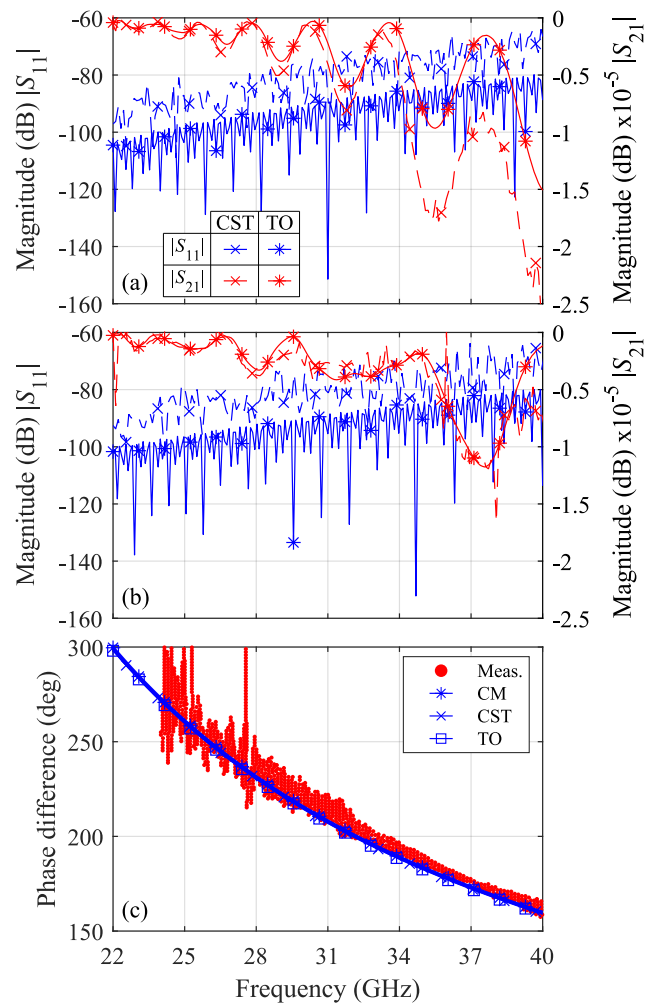


Figure 6.8: Long shifter [144]: (a)  $|S_{11}|$  and  $|S_{21}|$  for TE<sub>11</sub> inductive polarization; (b)  $|S_{11}|$  and  $|S_{21}|$  for TE<sub>11</sub> capacitive polarization; (c) phase difference between polarizations. In the legends of (c), Meas. stands for measurements, and CM for the coupled mode theory used in [144]. Data from [22].

for the phase difference. Magnitude discrepancies for  $|S_{11}|$ , occurring only for values below  $-60$  dB, arise from the limited accuracy of CST and the proposed method. The two phase shifters combined realize a polarizer [144] with a FBW of 32% and phase margin of  $\pm 5^\circ$  from the target value of  $90^\circ$ . For a detailed comparison of computational costs between the proposed method and CST, the reader is directed to [22].

## 6.4 Conclusion and future developments

A panoramic view of TO applied to closed waveguide problems is provided. Starting from the transformation from the OD to the TD, the description of the solutions to 2D eigenvalue problems and 3D problems with excitation for nonsmooth and smooth waveguide devices followed. All three cases align well with full-wave numerical methods, like FEM, and available measurements.

Research on this topic has great potential. Possible extensions are:

1. solution of the 2D eigenvalue problem for multi-connected domains;
2. solution of the 2D eigenvalue problem considering the electric field vector wave equation for TE modes;
3. analysis of devices with smooth lateral surfaces and arbitrary input and output ports (not limited to CWs);
4. extension of the 3D method for smooth surfaces to free-form shapes;
5. implementation of the proposed methods into a commercial FWS.

Point 1 is of interest for deformed coaxial cables and could be applied to patch antennas with a degeneration driver in a cavity model framework [78, 137]. Point 2 is of interest to obtain an expansion over CW modes even for TE modes. In addition, this is a prerequisite for point 3 since the field expansion for the 3D problem is based only on the electric field and it is necessary to expand the eigenmodes of the ports in terms of CW modes. Point 3 is key for analyzing a wider class of waveguide devices such as rectangular to CW transitions. Combined with MM, it enhances the analysis of complex geometries like those in [157]. Point 4 is also useful for analyzing more arbitrary devices such as those with a free-form shape [130, 133], nowadays enabled by 3D printing. Eventually, point 5 would prove the effectiveness and recognition of the method in the scientific and industry communities.

# Chapter 7

## Conclusion and future developments

### 7.1 Summary of contributions

In summary, the main contributions outlined in the thesis are:

- Ch. 2** an innovative method based on the dyadic Green's function and the equivalence principle is proposed to solve open scattering problems involving an antenna illuminating a scatterer. This method allows for an arbitrary equivalence surface enclosing the antenna, thus decreasing the minimum permitted distance between the antenna and the scatterer. The scattering due to the scatterer is solved by the transmission matrix method. A limitation of the proposed approach is that no higher-order interactions between the antenna and the scatterer are considered numerically, although an algorithm for the solution has been sketched;
- Ch. 3** a new automatic easy-to-implement API between HFSS and MATLAB or Python is developed. This is accomplished by replacing the numerical values of the variables with placeholders. These are updated with new numerical values for each variable combination requested by the design approach being considered. This method does not resort to VBA scripts, thus making the proposed API user-friendly. The use of the API is illustrated with an example. Currently, the API is limited to FWSs encoded with ASCII files and therefore is not applicable, for instance, to CST;

**Ch. 4** on the one hand, coaxial combline cavity filters and diplexers are considered. In particular, (a) capacitive and inductive end couplings are compared and (b) a filter and a diplexer for E1 Galileo and Iridium applications are manufactured. The analysis (a) shows that both end couplings may be equivalent from an electrical point of view and the capacitive end coupling is more sensitive to manufacturing tolerances but easier to manufacture. The designs (b) are characterized by measured responses close to the synthesized ones.

On the other hand, single-layer microstrip diplexers are considered. In particular, two low-loss compact microstrip diplexers based on complementary spiral resonators are designed. The high-pass spiral resonators are the same in both diplexers, while the low-pass ones are not. The microstrip diplexers present competitive performance compared to the literature in terms of size and loss, but they are characterized by a narrow spurious-free bandwidth;

**Ch. 5** an enhanced asymmetric open TEM cell with a 10 cm-side cube UTV up to 1 GHz is designed. As a further development, the septum has been tapered to improve the impedance matching. To accomplish this, TEM-only propagation is assumed and a  $50\ \Omega$ -characteristic impedance along the taper is enforced for the TEM mode. In this way, the maximum  $|S_{11}|$  improved from  $-10.6\ \text{dB}$  to  $-15.2\ \text{dB}$ . Despite the improvement, the proposed solution is not full-wave, thus better results for  $|S_{11}|$  may be obtained by tapering the septum taking higher-order modes into account;

**Ch. 6** a full-wave numerical method for the analysis of closed waveguides is developed. The method is based on TO and considers both 2D eigenvalue problems and 3D problems with excitation. The original structure is transformed into a circular cylinder filled with inhomogeneous and anisotropic permittivity and permeability. The unknown field is expanded to fulfill the BCs. Both for the 2D and the 3D problems, the method proposed delivers results in good agreement with those from FEM and measurements, whenever available. The method is limited to waveguide devices with lateral surfaces expressed as single-valued functions with finite derivatives. For the 3D problems with excitation and smooth lateral surface, it is additionally requested that the input and output ports are CWs.

## 7.2 Directions for future work

In the author's point of view, the most remarkable next developments are:

- Ch. 2** numerical implementation of the algorithm for the analysis of open scattering problems that takes into account the higher-order interactions between the antenna and the scatterer;
- Ch. 3** extension of the API to programs not encoded in ASCII and to parallel simulations, and integration of the API into commercial CAD software;
- Ch. 4** extension of the external quality factor analysis to multimode cavities and introduction of tuning elements for the external quality factor; design of antennas directly integrated into filters; modeling of spiral resonators through an equivalent topology and design of more compact low-loss filters and diplexers with a wide spurious-free bandwidth;
- Ch. 5** consideration of higher-order modes in the analysis and design of the septum and characterization of the open TEM cell without pillars conceived for in-house manufacturing;
- Ch. 6** extension of the 2D eigenvalue problem solver to multi-connected domains; analysis of the 2D eigenvalue problem through the vector wave equation for the transverse electric field; extension of the method to devices with arbitrary ports and adaptation of the method to free-form shapes; implementation of the method in commercial CAD software.



# Nomenclature

$\varepsilon_0$	Permittivity of vacuum	$8.8542 \times 10^{-12} \text{ F m}^{-1}$
$\mu_0$	Permeability of vacuum	$1.2566 \times 10^{-6} \text{ H m}^{-1}$
$c$	Speed of light in vacuum	$299\,792\,458 \text{ m s}^{-1}$
$\varepsilon$	Permittivity	
$\mu$	Permeability	
$j$	Imaginary unit	
$\omega$	Angular frequency	
$t$	Time	
$e^{j\omega t}$	Harmonic time factor	
$\mathbf{E}$	Electric field	
$\mathbf{H}$	Magnetic field	
$f_0$	Center frequency	
$\lambda$	Wavelength	
$k$	Wavenumber	
$k_0$	Free-space wavenumber	
$k_c$	Cutoff wavenumber	
$Z$	Wave impedance	
$Z_c$	Characteristic impedance	

$g$	Free-space scalar Green's function
$\bar{\bar{G}}$	Free-space dyadic Green's function
$\mathbf{T}$	Transmission matrix
$S_{ij}$	Scattering parameter (output at port $i$ with port $j$ excited)
$Q_E$	External quality factor
$\Gamma_d$	Group delay
$\bar{\rho}$	Waveguide lateral surface
$\mathsf{T}$	Transpose operator

# Acronyms

**API** application programming interface

**BC** boundary condition

**CAD** computer-aided design

**CW** circular waveguide

**FBW** fractional bandwidth

**FEM** finite element method

**FWS** full-wave simulator

**MM** mode matching

**NCE** numeric computing environment

**OD** original domain

**PEC** perfect electric conductor

**TD** transformed domain

**TE** transverse electric

**TEM** transverse electromagnetic

**TM** transverse magnetic

**TO** transformation optics

**TSMF** transverse spherical multipole function

**UTV** uniform test volume

**VBA** visual basic for applications

**VSMF** vector spherical multipole function

# Appendix A

## Full list of publications

The author's publications are subdivided into:

- International journals: 13 (of which 1 before the Ph.D.);
- International conferences: 19 full papers and 2 abstracts;
- National conferences: 2;
- Source code: 8.

The list of all publications follows<sup>1</sup>.

### International Journals

1. G. G. Gentili, **G. Giannetti**, M. Khosronejad, G. Pelosi, and S. Selleri. “Modes computation in arbitrarily shaped waveguides by a transformation optics approach”, *International Journal of RF and Microwave Computer-Aided Engineering*, 31.1 (2021), e22480. [DOI: 10.1002/mmce.22480] [135]
2. G. G. Gentili, **G. Giannetti**, G. Pelosi, and S. Selleri. “Considerations on boundary conditions in transformation optics for complete field computation in generic waveguides”, *Microwave and Optical Technology Letters*, 65.1 (2023), pp. 373-380. [DOI: 10.1002/mop.33493] [20]
3. G. G. Gentili, **G. Giannetti**, G. Pelosi, and S. Selleri. “Transformation optics combined with line-integrals for fast and efficient mode matching analysis of waveguide devices”, *IEEE Journal of Microwaves*, 3.3 (2023), pp. 1051-1060. [DOI: 10.1109/JMW.2023.3275212] [21]

---

<sup>1</sup>The author's bibliometric indices are the following:  $H$ -index = 5, total number of citations = 70 (source: Google Scholar on October 31, 2024)

4. **G. Giannetti**, M. P. Anania, M. Bellaveglia, E. Chiadroni, A. Cianchi, A. D. Dotto, M. Galletti, A. Gallo, A. Giribono, L. Piersanti, R. Pompili, S. Romeo, B. Serenellini, S. Tocci, C. Vaccarezza, F. Villa, and M. Ferrario. “Experimental and numerical characterization of timing jitter for short electron beams in a linear photo-injector”, *Measurement Science and Technology*, 35.2 (2023), p. 025015. [DOI: 10.1088/1361-6501/ad099c] [84]
5. **G. Giannetti**, “Improved and easy-to-implement HFSS-MATLAB interface without VBA scripts: an insightful application to the numerical design of patch antennas”, *The Applied Computational Electromagnetics Society Journal*, 38.06 (2023), pp. 377-381. [DOI: 10.13052/2023.ACES.J.380601] [14]
6. **G. Giannetti**, C. Spindelberger, and H. Arthaber, “Simple semianalytical septum design for improved matching in open TEM cells”, *IEEE Letters on Electromagnetic Compatibility Practice and Applications*, 6.1 (2024), pp. 6-10. [DOI: 10.1109/LEMCPA.2023.3333003] (**featured on the front cover of the issue**) [19]
7. **G. Giannetti** and S. Maddio, “Low-loss compact diplexer based on complementary spiral resonators”, *Microwave and Optical Technology Letters*, 66.6 (2024), e34202. [DOI: 10.1002/mop.34202] [17]
8. **G. Giannetti**, S. Maddio, and S. Selleri, “A compact low-loss single-layer vialess diplexer based on complementary microstrip spiral resonators for satellite communications”, *Progress In Electromagnetics Research Letters*, 122 (2024), pp. 45-51. [DOI: 10.2528/PIERL24061104] [18]
9. E. Boni, **G. Giannetti**, S. Maddio, and G. Pelosi, “Comparison of inductive and capacitive end couplings in the design of a combline microwave cavity filter for the E1 Galileo band”, *Advances in Radio Science*, 22 (2024), pp. 1-8. [DOI: 10.5194/ars-22-1-2024] [15]
10. **G. Giannetti** and L. Klinkenbusch, “A numerical alternative for 3D addition theorems based on the bilinear form of the dyadic Green’s function and the equivalence principle”, *Advances in Radio Science*, 22 (2024), pp. 9-15. [DOI: 10.5194/ars-22-9-2024] [13]
11. **G. Giannetti**, S. Maddio, and E. Boni, “Compact all-metal in-line combline coaxial cavity diplexer,” *Journal of Telecommunications and Information Technology*, 4 (2024), pp. 9-14. [DOI: 10.26636/jtit.2024.4.1783] [16]

12. **G. Giannetti**, S. Selleri, G. G. Gentili, G. Garcia-Contreras, J. Córcoles, and J. A. Ruiz-Cruz, “Advanced modeling of circular waveguide-based devices with smooth profiles using transformation optics and hierarchical model reduction,” *IEEE Journal of Microwaves*, 4.4 (2024), pp. 675-689. [DOI: 10.1109/JMW.2024.3454563] [22]
13. **G. Giannetti**, M. Bellaveglia, A. Gallo, S. Maddio, A. Mostacci, L. Piersanti, B. Serenellini, S. Selleri, and S. Tocci, “In-house design, manufacturing, and testing of a 2.856 GHz combline microwave cavity filter for the low-level RF systems of linear particle accelerators,” *Advanced Electromagnetics*, 14.1 (2025), pp. 8–13. [DOI: 10.7716/aem.v14i1.2517] [158]

## International Conferences

### Full papers

1. C. Spindelberger, **G. Giannetti**, and H. Arthaber, “Increasing the test-volume of open TEM cells by using an asymmetric design,” in *2022 Kleinheubach Conference*, Miltenberg (Germany), 2022, pp. 1-4. [URL: <https://ieeexplore.ieee.org/document/9954542>] [120]
2. L. Piersanti, D. Alesini, M. Bellaveglia, S. Bini, B. Buonomo, F. Cardelli, C. D. Giulio, E. D. Pasquale, M. Diomedede, L. Faillace, A. Falone, G. Franzini, A. Gallo, **G. Giannetti**, A. Liedl, D. Moriggi, S. Pioli, S. Quaglia, L. Sabbatini, M. Scampati, G. Scarselletta, A. Stella, S. Tocci, and L. Zelinotti, “Commissioning and first results of an X-band LLRF system for TEX test facility at LNF-INFN,” in *Journal of Physics: Conference Series*, IOP Publishing, Bangkok (Thailand), 2023, p. 12075. [DOI: 10.1088/1742-6596/2420/1/012075] [159]
3. E. Boni, **G. Giannetti**, S. Maddio, and G. Pelosi, “A circular polarized antenna for GPS and Iridium applications,” in *2023 IEEE International Symposium on Antennas and Propagation*, Portland (Oregon, USA), 2023, pp. 195-196. [DOI: 10.1109/USNC-URSI52151.2023.10237948] [116]
4. E. Boni, **G. Giannetti**, S. Maddio, and G. Pelosi, “An equation-based method for the design of end couplings in combline microwave cavity filters,” in *2023 IEEE International Symposium on Antennas and Propagation*, Portland (Oregon, USA), 2023, pp. 1473-1474. [DOI: 10.1109/USNC-URSI52151.2023.10237496] [76]
5. G. G. Gentili, **G. Giannetti**, S. Maddio, and M. Oldoni, “A gap coupled patch array based on the multilobate design,” in *2023 IEEE International*

- Symposium on Antennas and Propagation*, Portland (Oregon, USA), 2023, pp. 477-478. [DOI: 10.1109/USNC-URSI52151.2023.10238120] [160]
6. **G. Giannetti** and L. Klinkenbusch, “Comparative study of two multipole-based numerical methods for 2D field-translation schemes,” in *2023 Kleinheubach Conference*, Miltenberg (Germany), 2023, pp. 1-4. [URL: <https://ieeexplore.ieee.org/document/10296703>] (**Young Scientist Award and Young Scientist Best Paper Award - 2nd place**) [45]
  7. E. Boni, **G. Giannetti**, S. Maddio, and G. Pelosi, “Fast and efficient systematic procedure for and flexibility on the end coupling design in microwave filters,” in *2023 Kleinheubach Conference*, Miltenberg (Germany), 2023, pp. 1-4. [URL: <https://ieeexplore.ieee.org/document/10296826>] [77]
  8. E. Boni, **G. Giannetti**, S. Maddio, and G. Pelosi, “Capacitive end-couplings in combline microwave cavity filters with probe parallel to resonators’ axes: comparison and design guidelines,” in *2023 Kleinheubach Conference*, Miltenberg (Germany), 2023, pp. 1-4. [URL: <https://ieeexplore.ieee.org/document/10296707>] [101]
  9. **G. Giannetti** and L. Klinkenbusch, “The contributions to electromagnetism achieved by Heinrich Hertz at Kiel University,” in *2023 8th IEEE History of Electrotechnology Conference*, Florence (Italy), 2023, pp. 1-3. [DOI: 10.1109/HISTELCON56357.2023.10365820] [161]
  10. A. Giribono, D. Alesini, A. Bacci, M. Bellaveglia, F. Cardelli, E. Chiadroni, A. Del Dotto, L. Faillace, M. Ferrario, A. Gallo, A. Ghigo, **G. Giannetti**, A. Mostacci, M. Opromolla, V. Petrillo, L. Piersanti, R. Pompili, S. Romeo, M. Rossetti Conti, A. R. Rossi, V. Shpakov, G. J. Silvi, and C. Vaccarezza, “Electron beam analysis and sensitivity studies for the EuPRAXIA@ SPARC LAB RF injector,” in *Journal of Physics: Conference Series*, Venice (Italy), 2024, p. 32022. [DOI: 10.1088/1742-6596/2687/3/032022] [162]
  11. **G. Giannetti**, C. Spindelberger, S. Selleri, and H. Arthaber, “Effects of the ground plane and of neighbouring objects on the performances of open TEM cells,” in *2024 IEEE International Symposium on Antennas and Propagation*, Florence (Italy), 2024, pp. 2731-2732. [DOI: 10.1109/AP-S/INC-USNC-URSI52054.2024.10686986] [163]
  12. **G. Giannetti**, S. Maddio, and S. Selleri, “A twelve-element sequentially rotated array for circular polarization links at 5.8 GHz,” in *2024 IEEE International Symposium on Antennas and Propagation*, Florence (Italy), 2024,

- 
- pp. 2535-2536. [DOI: 10.1109/AP-S/INC-USNC-URSI52054.2024.10686819] [164]
13. G. G. Gentili, **G. Giannetti**, S. Maddio, and S. Selleri, "Tuning of multilobate patch antennas using the cavity model in a space mapping framework," in *2024 IEEE International Symposium on Antennas and Propagation*, Florence (Italy), 2024, pp. 1479-1480. [DOI: 10.1109/AP-S/INC-USNC-URSI52054.2024.10685909] [78]
  14. **G. Giannetti**, S. Maddio, and S. Selleri, "A versatile approach for the optimization of printed series antenna array," in *2024 IEEE International Symposium on Antennas and Propagation*, Florence (Italy), 2024, pp. 2231-2232. [DOI: 10.1109/AP-S/INC-USNC-URSI52054.2024.10686909] [79]
  15. **G. Giannetti**, "Automatic generation and substitution of placeholders for a MATLAB-HFSS interface," in *2024 IEEE International Symposium on Antennas and Propagation*, Florence (Italy), 2024, pp. 2005-2006. [DOI: 10.1109/AP-S/INC-USNC-URSI52054.2024.10686900] [72]
  16. K. Davidhi, **G. Giannetti**, M. Righini, and S. Selleri, "A compact passband filter based on folded split ring resonators for ISM applications at 5.8GHz," in *2024 IEEE International Symposium on Antennas and Propagation*, Florence (Italy), 2024, pp. 2697-2698. [DOI: 10.1109/AP-S/INC-USNC-URSI52054.2024.10687017] [165]
  17. G. G. Gentili, **G. Giannetti**, S. Maddio, and M. Oldoni, "A filter based on gap coupled multilobate design for C-band applications," in *2024 IEEE International Symposium on Antennas and Propagation*, Florence (Italy), 2024, pp. 2625-2626. [DOI: 10.1109/AP-S/INC-USNC-URSI52054.2024.10686342] [166]
  18. **G. Giannetti**, "Fully automated Python- and MATLAB-HFSS interfaces without VBA scripts for advanced design techniques," in *2024 54rd European Microwave Conference*, Paris (France), 2024, pp. 64-67. [DOI: 10.23919/EuMC61614.2024.10732839] [73]
  19. **G. Giannetti** and L. Klinkenbusch, "Interpretation and separability of the effective permittivity in case that both permittivity and conductivity are complex," in *2023 URSI International Symposium on Electromagnetic Theory*, Vancouver (British Columbia, Canada), 2023. [URL: <https://flore.unifi.it/handle/2158/1328818>] [167]

## Abstracts

1. **G. Giannetti** and L. Klinkenbusch, “Conditions and approximations for retrieving the complex permittivity and conductivity from the effective permittivity”, in *2023 Kleinheubach Conference*, Miltenberg (Germany), 2023. [URL=<https://flore.unifi.it/handle/2158/1354832>]
2. L. Klinkenbusch and **G. Giannetti**, “Das Wirken von Heinrich Hertz an der Christian-Albrechts-Universität zu Kiel 1883-1885”, in *2023 Kleinheubach Conference*, Miltenberg (Germany), 2023. [URL=<https://flore.unifi.it/handle/2158/1354831>]

## National Conferences

1. E. Boni, **G. Giannetti**, and S. Maddio, “Design of a combline microwave cavity filter for the E1 Galileo band”, *XXIV Riunione Nazionale Elettromagnetismo - Proceedings*, Catania (CT), Italy, 2022. [URL=<https://flore.unifi.it/handle/2158/1328491>]
2. **G. Giannetti**, S. Maddio, and S. Selleri, “A quadrature hybrid directional coupler with superelliptical shape for 5.8 GHz applications”, *XXV Riunione Nazionale Elettromagnetismo - Proceedings*, Viareggio (LU), Italy, 2024. [URL=<https://flore.unifi.it/handle/2158/1395672>]

## Source Code

1. **G. Giannetti**, “Mode Fields Computed with a Transformation Optics Approach”, 2023. [DOI: 10.24433/CO.5437224.v1]
2. **G. Giannetti**, “Mode matching analysis of waveguide devices applied to mode fields computed with the transformation optics approach”, 2023. [DOI: 10.24433/CO.4483883.v1]
3. **G. Giannetti**, “Gianne97/HFSS-MATLAB-API-without-VBA-scripts: HFSS-MATLAB API with-out VBA scripts - Publication. Version Publication”, 2023. [DOI: 10.5281/zenodo.8065817]
4. **G. Giannetti**, “Gianne97/HFSS-Python-API-without-VBA-scripts: HFSS-Python-API-without-VBA- scripts-v1.2. Version v1.2”, 2024. [DOI: 10.5281/zenodo.10787184]

5. **G. Giannetti**, C. Spindelberger, and H. Arthaber, “Code for the paper entitled “Simple semi-analytical septum design for improved matching in open TEM cells””, 2023. [DOI: 10.24433/CO.4880490.v1]
6. **G. Giannetti**, “Gianne97/Comblin-cavity-filter-for- the-E1-Galileo-band: Comblin-cavity-filter-for-the-E1-Galileo-band-Additional-Material. Version v1.3”, 2023. [DOI: 10.5281/zenodo.10246132]
7. **G. Giannetti**, “Gianne97/Comblin-cavity-filter-2856-MHz- bandwidth-30-MHz: Comblin-cavity-filter-2856-MHz- bandwidth-30-MHz-Zenodo. Version v2”, 2024. [DOI: 10.5281/zenodo.10670431]
8. **G. Giannetti**, “Gianne97/CS2MBNM: FirstVersion. Version v1”, 2024. [DOI: 10.5281/zenodo.10895365]

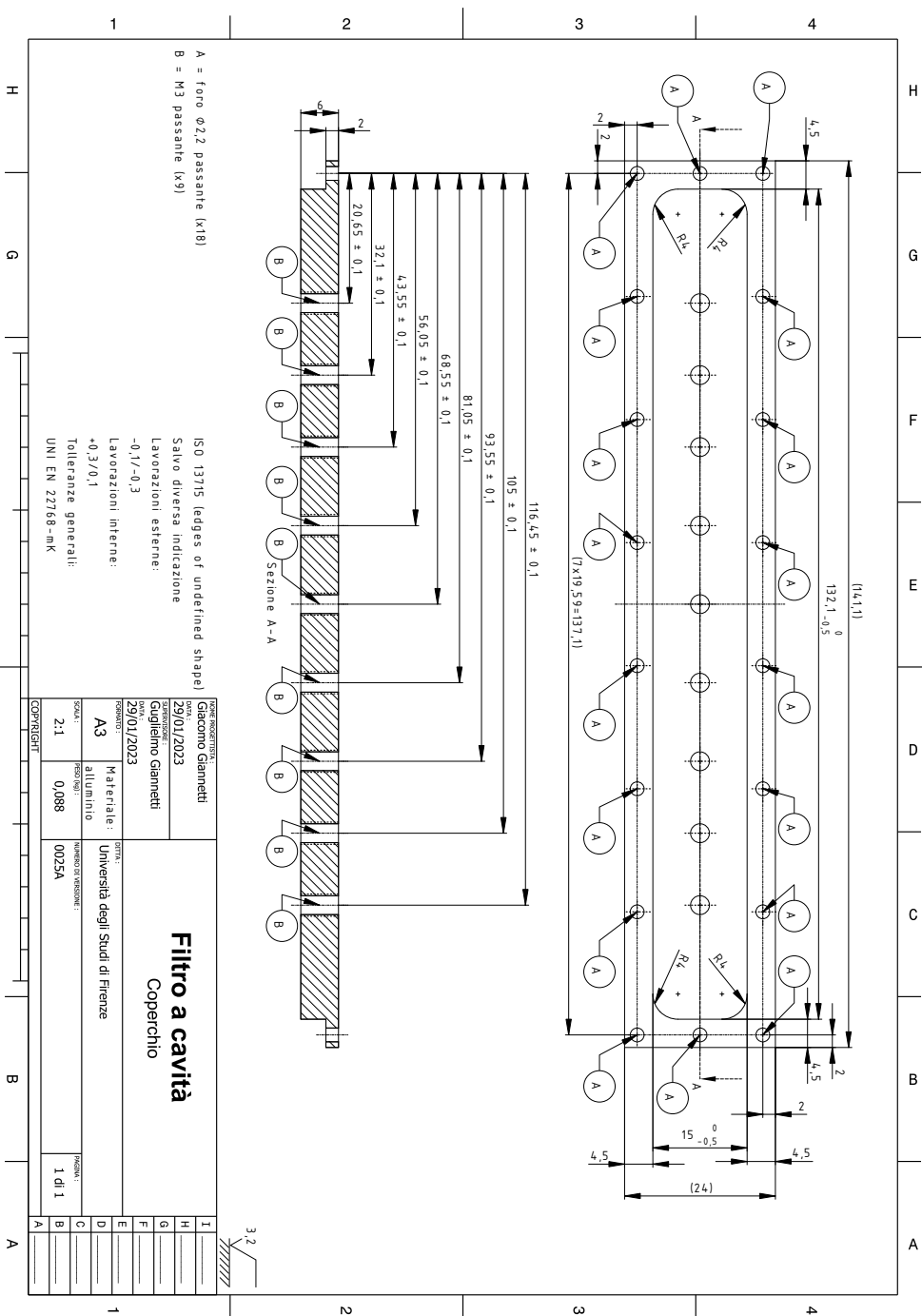


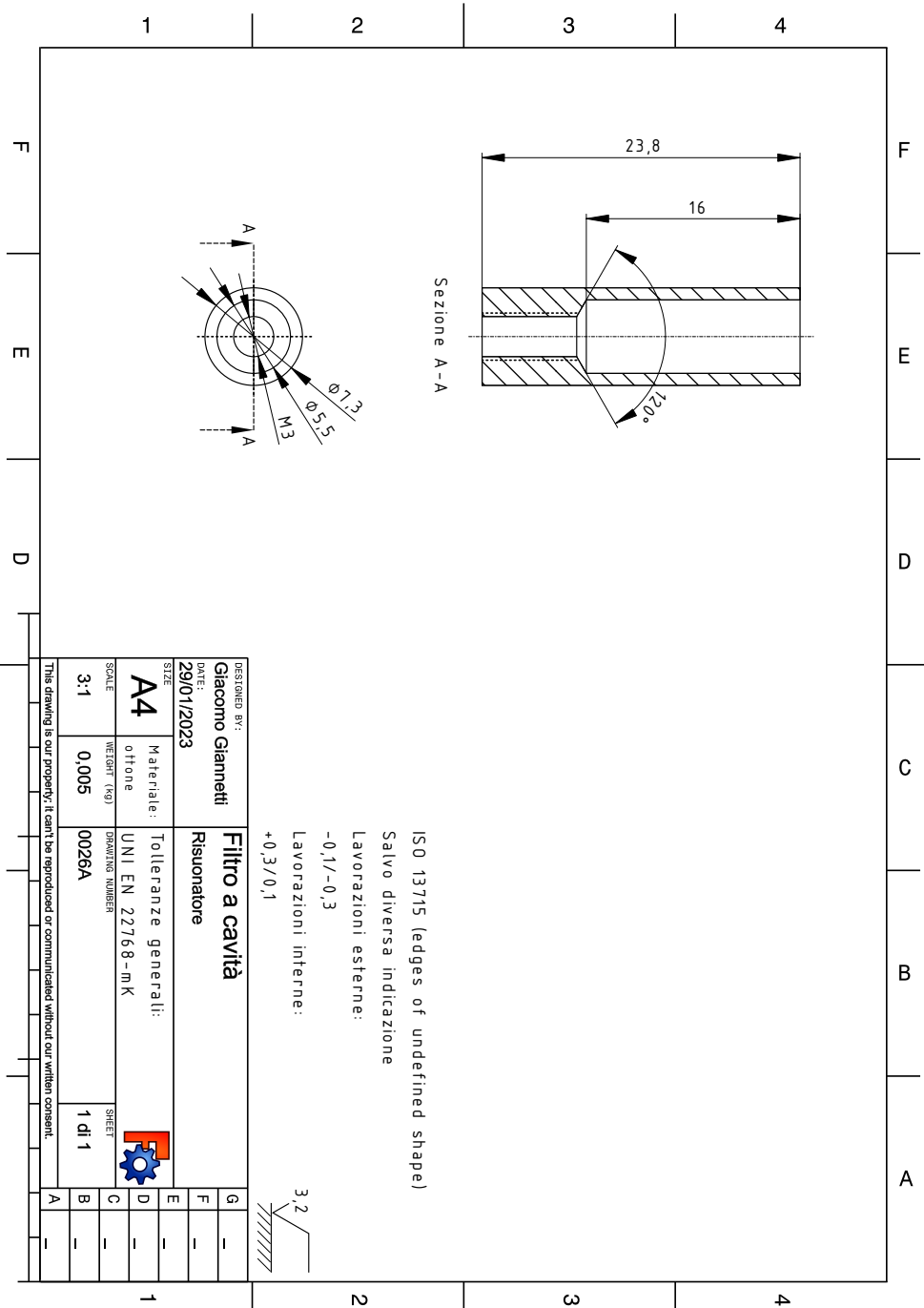
# Appendix B

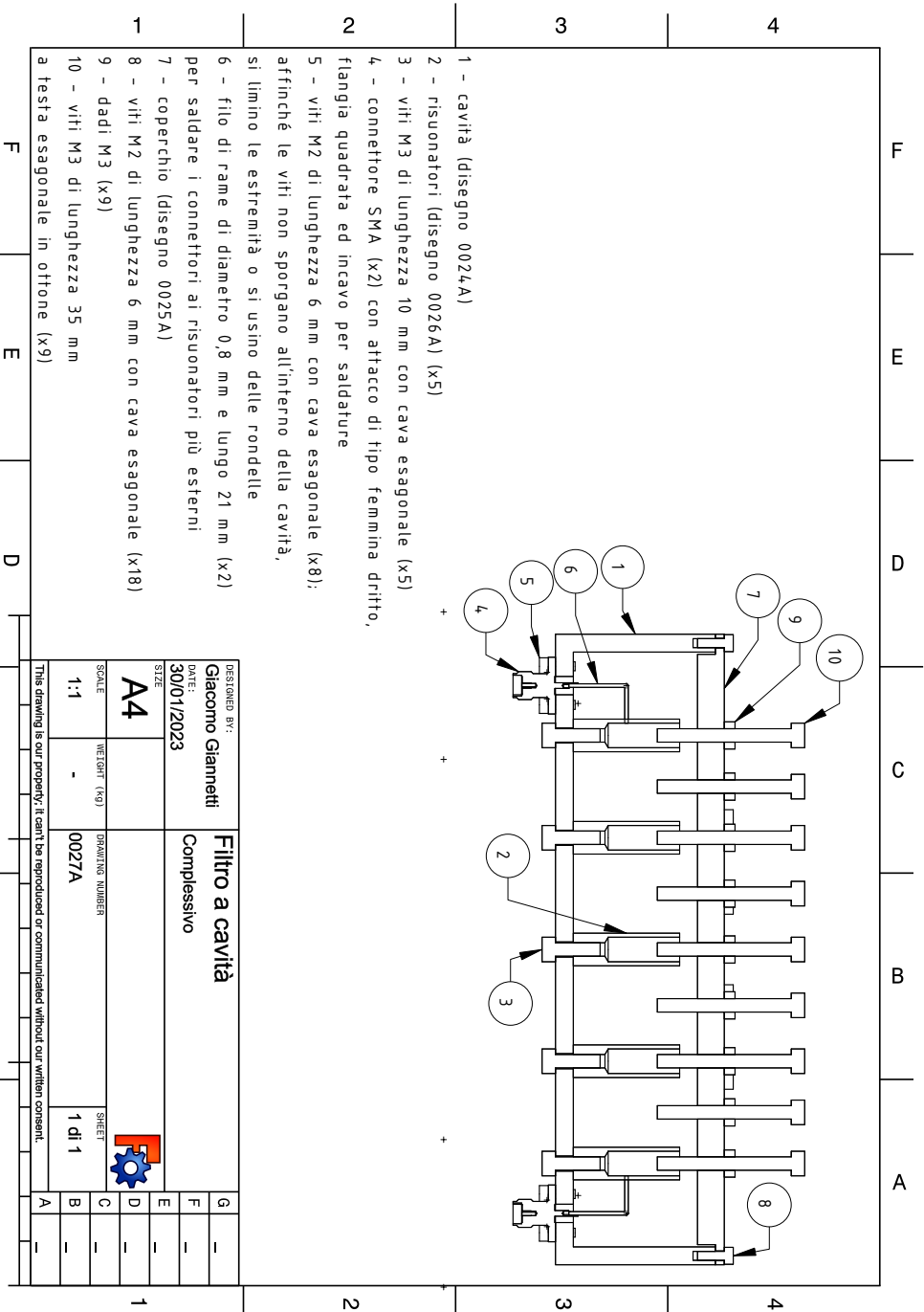
## Technical drawings

This appendix contains the technical drawings of the L-band cavity filter for E1 Galileo and Iridium presented in Ch. 4. The technical drawings appear in the following order: cavity, lid, resonator, and master layout. The cavity, lid, and resonators were manufactured by Prima Engineering s.r.l., Via Albert Einstein, 35/31 - 50013 Campi Bisenzio (FI), Italy, <https://primaeng.it/>. Since the manufacturer was Italian, the technical drawings are in Italian.









- 1 - cavità (disegno 0024A)
- 2 - risonatori (disegno 0026A) (x5)
- 3 - viti M3 di lunghezza 10 mm con cava esagonale (x5)
- 4 - connettore SMA (x2) con attacco di tipo femmina dritto, flangia quadrata ed incavo per saldature
- 5 - viti M2 di lunghezza 6 mm con cava esagonale (x8); affinché le viti non sporgano all'interno della cavità, si limino le estremità o si usino delle rondelle
- 6 - filo di rame di diametro 0,8 mm e lungo 21 mm (x2) per saldare i connettori ai risonatori più esterni
- 7 - coperchio (disegno 0025A)
- 8 - viti M2 di lunghezza 6 mm con cava esagonale (x18)
- 9 - dadi M3 (x9)
- 10 - viti M3 di lunghezza 35 mm a testa esagonale in ottone (x9)

DESIGNED BY: <b>Giacomo Giannetti</b>		<b>Filtro a cavità</b>		G	
DATE: <b>30/01/2023</b>		<b>Complessivo</b>		F	
SIZE <b>A4</b>				E	
SCALE <b>1:1</b>		DRAWING NUMBER <b>0027A</b>		D	
		WEIGHT (KG) <b>-</b>		C	
		SHEET <b>1 di 1</b>		B	
				A	

This drawing is our property; it can't be reproduced or communicated without our written consent.



# Bibliography

- [1] F. I. Kubota, P. A. Cauchick-Migue, G. Tortorella, and M. Amorim, “Paper-based thesis and dissertations: analysis of fundamental characteristics for achieving a robust structure,” *Production*, vol. 31, pp. 1–12, 2021.
- [2] R. Barrass, *Scientists Must Write: A Guide to Better Writing for Scientists, Engineers and Students*. London, UK: Chapman and Hall, 1978.
- [3] A. Dalton, K. Wolff, and B. Bekker, “Multidisciplinary research as a complex system,” *International Journal of Qualitative Methods*, vol. 20, p. 16094069211038400, 1 2021.
- [4] L. D. Landau and E. M. Lifshitz, *Electrodynamics of Continuous Media*, ser. *Electrodynamics of Continuous Media*. Oxford, UK: Pergamon, 1960.
- [5] J. D. Jackson, *Classical Electrodynamics*. New York (NY), USA: Wiley, 1999.
- [6] J. A. Stratton, *Electromagnetic Theory*, ser. *Electromagnetic Wave Theory*. Hoboken (NJ), USA: Wiley-IEEE Press, 2015.
- [7] C. Balanis, *Advanced Engineering Electromagnetics*. New York (NY), USA: Wiley, 2012.
- [8] S. Ramo, J. R. Whinnery, and T. Van Duzar, *Fields and Waves in Communication Electronics*. New York (NY), USA: Wiley, 1997.
- [9] R. F. Harrington, *Time-Harmonic Electromagnetic Fields*, ser. *IEEE press classic reissue*. New York (NY), USA: Wiley-IEEE Press, 2001.
- [10] R. E. Collin, *Foundations for Microwave Engineering*, ser. *Electrical engineering series*. New York (NY), USA: McGraw-Hill, 1992.
- [11] D. M. Pozar, *Microwave Engineering*, 4th ed. New York (NY), USA: Wiley, 2011.

- 
- [12] L. Allen, A. O’Connell, and V. Kiermer, “How can we ensure visibility and diversity in research contributions? How the Contributor Role Taxonomy (CRediT) is helping the shift from authorship to contributorship,” *Learned Publishing*, vol. 32, no. 1, pp. 71–74, 1 2019.
- [13] G. Giannetti and L. Klinkenbusch, “A numerical alternative for 3D addition theorems based on the bilinear form of the dyadic Green’s function and the equivalence principle,” *Advances in Radio Science*, vol. 22, pp. 9–15, 2024.
- [14] G. Giannetti, “Improved and easy-to-implement HFSS-MATLAB interface without VBA scripts: an insightful application to the numerical design of patch antennas,” *The Applied Computational Electromagnetics Society Journal*, vol. 38, no. 6, pp. 377–381, 11 2023.
- [15] E. Boni, G. Giannetti, S. Maddio, and G. Pelosi, “Comparison of inductive and capacitive end couplings in the design of a combline microwave cavity filter for the E1 Galileo band,” *Advances in Radio Science*, vol. 22, pp. 1–8, 2024.
- [16] G. Giannetti, S. Maddio, and E. Boni, “Compact all-metal in-line combline coaxial cavity diplexer,” *Journal of Telecommunications and Information Technology*, pp. 9–14, 10 2024.
- [17] G. Giannetti and S. Maddio, “Low-loss compact diplexer based on complementary spiral resonators,” *Microwave and Optical Technology Letters*, vol. 66, no. 6, 6 2024.
- [18] G. Giannetti, S. Maddio, and S. Selleri, “A compact low-loss single-layer vialess diplexer based on complementary microstrip spiral resonators for satellite communications,” *Progress In Electromagnetics Research Letters*, vol. 122, pp. 45–51, 2024.
- [19] G. Giannetti, C. Spindelberger, and H. Arthaber, “Simple semianalytical septum design for improved matching in open TEM cells,” *IEEE Letters on Electromagnetic Compatibility Practice and Applications*, vol. 6, no. 1, pp. 6–10, 2024.
- [20] G. G. Gentili, G. Giannetti, G. Pelosi, and S. Selleri, “Considerations on boundary conditions in transformation optics for complete field computation in generic waveguides,” *Microwave and Optical Technology Letters*, vol. 65, no. 1, pp. 373–380, 2023.

- 
- [21] —, “Transformation optics combined with line-integrals for fast and efficient mode matching analysis of waveguide devices,” *IEEE Journal of Microwaves*, vol. 3, no. 3, pp. 1051–1060, 2023.
- [22] G. Giannetti, S. Selleri, G. G. Gentili, G. Garcia-Contreras, J. Córcoles, and J. A. Ruiz-Cruz, “Advanced modeling of circular waveguide-based devices with smooth profiles using transformation optics and hierarchical model reduction,” *IEEE Journal of Microwaves*, vol. 4, no. 4, pp. 675–689, 2024.
- [23] R. E. Collin, *Field Theory of Guided Waves*, ser. Electromagnetic Wave Theory. New York (NY), USA: Wiley-IEEE Press, 1990.
- [24] P. Sumithra and D. Thiripurasundari, “Review on computational electromagnetics,” *Advanced Electromagnetics*, vol. 6, no. 1, p. 42, 3 2017.
- [25] B. M. Notaroš, “75 years of IEEE AP-S research in computational electromagnetics: a view on the discipline and its history, current state, and future prospects,” *IEEE Antennas and Propagation Magazine*, vol. 66, no. 3, pp. 68–83, 2024.
- [26] Z. Chen, C. F. Wang, and W. J. Hoefer, “A unified view of computational electromagnetics,” *IEEE Transactions on Microwave Theory and Techniques*, vol. 70, no. 2, pp. 955–969, 2 2022.
- [27] W. J. R. Hoefer, “A brief history of computational electromagnetics in microwave engineering—A personal retrospective,” *IEEE Journal of Microwaves*, vol. 3, no. 1, pp. 338–348, 1 2023.
- [28] D. B. Davidson, *Computational Electromagnetics for RF and Microwave Engineering*, 2nd ed. Cambridge, UK: Cambridge University Press, 2010.
- [29] R. Mittra, *Computer techniques for electromagnetics*. Oxford, UK: Pergamon, 1973.
- [30] T. Itoh, Ed., *Numerical Techniques for Microwave and Millimeter-Wave Passive Structures*. New York (NY), USA: Wiley, 1989.
- [31] R. C. Booton, *Computational Methods for Electromagnetics and Microwaves*. New York (NY), USA: Wiley, 1992.
- [32] R. F. Harrington and J. L. Harrington, *Field Computation by Moment Methods*. Oxford, UK: Oxford University Press, Inc., 1996.

- 
- [33] K. Zhao, V. Rawat, and J.-F. Lee, “A domain decomposition method for electromagnetic radiation and scattering analysis of multi-target problems,” *IEEE Transactions on Antennas and Propagation*, vol. 56, no. 8, pp. 2211–2221, 8 2008.
- [34] B. Stupfel, “A fast-domain decomposition method for the solution of electromagnetic scattering by large objects,” *IEEE Transactions on Antennas and Propagation*, vol. 44, no. 10, pp. 1375–1385, 1996.
- [35] S.-C. Lee, M. N. Vouvakis, and J.-F. Lee, “A non-overlapping domain decomposition method with non-matching grids for modeling large finite antenna arrays,” *Journal of Computational Physics*, vol. 203, no. 1, pp. 1–21, 2 2005.
- [36] M.-K. Li, W. C. Chew, and L. J. Jiang, “A domain decomposition scheme based on equivalence theorem,” *Microwave and Optical Technology Letters*, vol. 48, no. 9, pp. 1853–1857, 2006.
- [37] M.-K. Li and W. C. Chew, “Wave-field interaction with complex structures using equivalence principle algorithm,” *IEEE Transactions on Antennas and Propagation*, vol. 55, no. 1, pp. 130–138, 1 2007.
- [38] M. Alian and H. Oraizi, “Electromagnetic multiple PEC object scattering using equivalence principle and addition theorem for spherical wave harmonics,” *IEEE Transactions on Antennas and Propagation*, vol. 66, no. 11, pp. 6233–6243, 11 2018.
- [39] —, “Application of equivalence principle for EM scattering from irregular array of arbitrarily oriented PEC scatterers using both translation and rotation addition theorems,” *IEEE Transactions on Antennas and Propagation*, vol. 67, no. 5, pp. 3256–3267, 5 2019.
- [40] V. Losenicky, L. Jelinek, M. Capek, and M. Gustafsson, “Method of moments and T-matrix hybrid,” *IEEE Transactions on Antennas and Propagation*, vol. 70, no. 5, pp. 3560–3574, 5 2022.
- [41] P. C. Waterman, “Matrix formulation of electromagnetic scattering,” *Proceedings of the IEEE*, vol. 53, no. 8, pp. 805–812, 1965.
- [42] M. I. Mishchenko, L. D. Travis, and D. W. Mackowski, “T-matrix computations of light scattering by nonspherical particles: a review,” *Journal of Quantitative Spectroscopy and Radiative Transfer*, vol. 55, no. 5, pp. 535–575, 1996.

- [43] W. C. Chew, *Waves and Fields in Inhomogeneous Media*, ser. Electromagnetic waves. New York (NY), USA: IEEE Press, 1995.
- [44] M. Ganesh and S. C. Hawkins, “Three dimensional electromagnetic scattering T-matrix computations,” *Journal of Computational and Applied Mathematics*, vol. 234, no. 6, pp. 1702–1709, 2010.
- [45] G. Giannetti and L. Klinkenbusch, “Comparative study of two multipole-based numerical methods for 2D field-translation schemes,” in *2023 Kleinheubach Conference*, 2023, pp. 1–4.
- [46] L. Klinkenbusch, “Brief review of spherical-multipole analysis in radio science,” *URSI Radio Science Bulletin*, vol. 2008, no. 324, pp. 5–16, 2008.
- [47] “CST Studio Suite,” 2024. [Online]. Available: <https://www.3ds.com/products-services/simulia/products/cst-studio-suite/>
- [48] Y. Álvarez, F. Las-Heras, and M. R. Pino, “Reconstruction of equivalent currents distribution over arbitrary three-dimensional surfaces based on integral equation algorithms,” *IEEE Transactions on Antennas and Propagation*, vol. 55, no. 12, pp. 3460–3468, 12 2007.
- [49] J. L. Araque Quijano, L. Scialacqua, J. Zackrisson, L. J. Foged, M. Sabbadini, and G. Vecchi, “Suppression of undesired radiated fields based on equivalent currents reconstruction from measured data,” *IEEE Antennas and Wireless Propagation Letters*, vol. 10, pp. 314–317, 2011.
- [50] C. Tai, *Dyadic Green Functions in Electromagnetic Theory*. New York (NY), USA: IEEE Press, 1994.
- [51] A. J. Hesford and W. C. Chew, “On preconditioning and the eigensystems of electromagnetic radiation problems,” *IEEE Transactions on Antennas and Propagation*, vol. 56, no. 8, pp. 2413–2420, 2008.
- [52] S. M. Rao, D. R. Wilton, and A. W. Glisson, “Electromagnetic scattering by surfaces of arbitrary shape,” *IEEE Transactions on Antennas and Propagation*, vol. 30, no. 3, pp. 409–418, 1982.
- [53] E. K. Miller, “Model-based parameter estimation in electromagnetics. I. Background and theoretical development,” *IEEE Antennas and Propagation Magazine*, vol. 40, no. 1, pp. 42–52, 1998.
- [54] —, “Model-based parameter estimation in electromagnetics. II. Applications to EM observables,” *IEEE Antennas and Propagation Magazine*, vol. 40, no. 2, pp. 51–65, 1998.

- [55] ———, “Model-based parameter estimation in electromagnetics. III. Applications to EM integral equations,” *IEEE Antennas and Propagation Magazine*, vol. 40, no. 3, pp. 49–66, 1998.
- [56] R. L. Haupt, “Using MATLAB to control commercial computational electromagnetics software,” *The Applied Computational Electromagnetics Society Journal*, vol. 23, no. 1, pp. 98–103, 6 2022.
- [57] A. Farahbakhsh, D. Zarifi, and A. Abdolali, “Using MATLAB to model inhomogeneous media in commercial computational electromagnetics software,” *The Applied Computational Electromagnetics Society Journal*, vol. 30, no. 9, pp. 1003–1007, 8 2021.
- [58] “MATLAB,” 2024. [Online]. Available: <https://www.mathworks.com/>
- [59] “Python,” 2024. [Online]. Available: <https://www.python.org/>
- [60] “Ansys,” 2024. [Online]. Available: <https://www.ansys.com/>
- [61] Q. Tan, K. Fan, W. Yang, and G. Luo, “Low sidelobe series-fed patch planar array with AMC structure to suppress parasitic radiation,” *Remote Sensing*, vol. 14, no. 15, 8 2022.
- [62] I. Bouchachi, “Microstrip antenna synthesis using an application programming interface,” *Journal of Mechanics of Continua and Mathematical Sciences*, vol. spl1, no. 4, 11 2019.
- [63] J. B. Romdhane Hajri, D. Inserra, W. Gu, W. Hu, Y. Huang, J. Li, and G. Wen, “Fast and automatic RF design based on MATLAB-HFSS control applied on magnetic absorber with metasurface,” in *2019 Photonics & Electromagnetics Research Symposium - Fall*. IEEE, 12 2019, pp. 1339–1342.
- [64] X. Yuan, Z. Li, D. Rodrigo, H. S. Mopidevi, O. Kaynar, L. Jofre, and B. A. Cetiner, “A parasitic layer-based reconfigurable antenna design by multi-objective optimization,” *IEEE Transactions on Antennas and Propagation*, vol. 60, no. 6, pp. 2690–2701, 2012.
- [65] “FEKO,” 2024. [Online]. Available: <https://www.altair.com/feko>
- [66] A. Arsenovic, J. Hillairet, J. Anderson, H. Forsten, V. Ries, M. Eller, N. Sauber, R. Weikle, W. Barnhart, and F. Forstmayr, “scikit-rf: an open source Python package for microwave network creation, analysis, and calibration,” *IEEE Microwave Magazine*, vol. 23, no. 1, pp. 98–105, 1 2022.

- [67] N. Kinayman, “Python for microwave and RF engineers,” *IEEE Microwave Magazine*, vol. 12, no. 7, pp. 113–122, 12 2011.
- [68] C. Fang, S. Xinyang, and X. Zeng, “Using Python to launch electromagnetic scattering simulation with FEKO,” in *2021 13th International Symposium on Antennas, Propagation and EM Theory*. IEEE, 12 2021, pp. 1–3.
- [69] R. J. Sánchez-Mesa, D. M. Cortés-Hernández, J. E. Rayas-Sánchez, Z. Brito-Brito, and L. De La Mora-Hernández, “EM parametric study of length matching elements exploiting an ANSYS HFSS Matlab-Python Driver,” in *2018 IEEE MTT-S Latin America Microwave Conference*, 2018, pp. 1–3.
- [70] “PyAnsys,” 2024. [Online]. Available: <https://docs.pyansys.com/>
- [71] N. Shrestha, C. Botta, T. Barik, and C. Parnin, “Here we go again: why is it difficult for developers to learn another programming language?” in *Proceedings of the ACM/IEEE 42nd International Conference on Software Engineering*, ser. ICSE ’20. New York (NY), USA: Association for Computing Machinery, 2020, pp. 691–701.
- [72] G. Giannetti, “Automatic generation and substitution of placeholders for a MATLAB-HFSS interface,” in *2024 IEEE International Symposium on Antennas and Propagation*, 2024, pp. 2005–2006.
- [73] —, “Fully automated Python- and MATLAB-HFSS interfaces without VBA scripts for advanced design techniques,” in *2024 54th European Microwave Conference*, 2024, pp. 64–67.
- [74] —, “Gianne97/HFSS-MATLAB-API-without-VBA-scripts: HFSS-MATLAB API with fully automated preliminary steps,” 3 2024. [Online]. Available: <https://doi.org/10.5281/zenodo.10818978>
- [75] —, “Gianne97/HFSS-Python-API-without-VBA-scripts: HFSS-Python-API-without-VBA-scripts-v1.2,” 3 2024. [Online]. Available: <https://doi.org/10.5281/zenodo.10818988>
- [76] E. Boni, G. Giannetti, S. Maddio, and G. Pelosi, “An equation-based method for the design of end couplings in combline microwave cavity filters,” in *2023 IEEE International Symposium on Antennas and Propagation*, 2023, pp. 1473–1474.
- [77] —, “Fast and efficient systematic procedure for and flexibility on the end coupling design in microwave filters,” in *2023 Kleinheubach Conference*, 2023, pp. 1–4.

- [78] G. G. Gentili, G. Giannetti, S. Maddio, and S. Selleri, "Tuning of multilobate patch antennas using the cavity model in a space mapping framework," in *2024 IEEE International Symposium on Antennas and Propagation*, 2024, pp. 1479–1480.
- [79] G. Giannetti, S. Maddio, and S. Selleri, "A versatile approach for the optimization of printed series antenna array," in *2024 IEEE International Symposium on Antennas and Propagation*, 2024, pp. 2231–2232.
- [80] C. A. Balanis, *Antenna Theory: Analysis and Design*, 4th ed. Hoboken (NJ), USA: Wiley, 2016.
- [81] S. Maddio, A. Cidronali, M. Passafiume, G. Collodi, and S. Maurri, "Fine-grained azimuthal direction of arrival estimation using received signal strengths," *Electronics Letters*, vol. 53, no. 10, pp. 687–689, 2017.
- [82] K. Yang, G. David, J.-G. Yook, I. Papapolymerou, L. P. B. Katehi, and J. F. Whitaker, "Electrooptic mapping and finite-element modeling of the near-field pattern of a microstrip patch antenna," *IEEE Transactions on Microwave Theory and Techniques*, vol. 48, no. 2, pp. 288–294, 2000.
- [83] "GPT," 2022. [Online]. Available: <https://www.pulsar.nl/gpt/>
- [84] G. Giannetti, M. P. Anania, M. Bellaveglia, E. Chiadroni, A. Cianchi, A. D. Dotto, M. Galletti, A. Gallo, A. Giribono, L. Piersanti, R. Pompili, S. Romeo, B. Serenellini, S. Tocci, C. Vaccarezza, F. Villa, and M. Ferrario, "Experimental and numerical characterization of timing jitter for short electron beams in a linear photo-injector," *Measurement Science and Technology*, vol. 35, no. 2, p. 25015, 11 2023.
- [85] R. J. Cameron, C. M. Kudsia, and R. R. Mansour, *Microwave Filters for Communication Systems*, 2nd ed. Hoboken (NJ), USA: Wiley, 2018.
- [86] A. Sahu, P. H. Aaen, and V. K. Devabhaktuni, "Advanced technologies for next-generation RF front-end modules," *International Journal of RF and Microwave Computer-Aided Engineering*, vol. 29, no. 6, p. e21700, 6 2019.
- [87] A. O. Watanabe, M. Ali, S. Y. B. Sayeed, R. R. Tummala, and M. R. Pugalurtha, "A review of 5G front-end systems package integration," *IEEE Transactions on Components, Packaging and Manufacturing Technology*, vol. 11, no. 1, pp. 118–133, 1 2021.
- [88] O. A. Peverini, M. Lumia, G. Addamo, F. Paonessa, G. Virone, R. Tascone, F. Calignano, G. Cattano, and D. Manfredi, "Integration of an H-plane

- bend, a twist, and a filter in Ku/K-band through additive manufacturing,” *IEEE Transactions on Microwave Theory and Techniques*, vol. 66, no. 5, pp. 2210–2219, 5 2018.
- [89] P. P. Shome, T. Khan, S. K. Koul, and Y. M. M. Antar, “Filtenna designs for radio-frequency front-end systems: a structural-oriented review,” *IEEE Antennas and Propagation Magazine*, vol. 63, no. 5, pp. 72–84, 2021.
- [90] R. Gomez-Garcia, D. Psychogiou, J. M. Munoz-Ferreras, and L. Yang, “Avoiding RF isolators: reflectionless microwave bandpass filtering components for advanced RF front ends,” *IEEE Microwave Magazine*, vol. 21, no. 12, pp. 68–86, 12 2020.
- [91] R. V. Snyder, A. Mortazawi, I. Hunter, S. Bastioli, G. Macchiarella, and K. Wu, “Present and future trends in filters and multiplexers,” *IEEE Transactions on Microwave Theory and Techniques*, vol. 63, no. 10, pp. 3324–3360, 10 2015.
- [92] R. V. Snyder, G. Macchiarella, S. Bastioli, and C. Tomassoni, “Emerging trends in techniques and technology as applied to filter design,” *IEEE Journal of Microwaves*, vol. 1, no. 1, pp. 317–344, 1 2021.
- [93] S. Bastioli and R. V. Snyder, “Nonresonating modes do it better!: exploiting additional modes in conjunction with operating modes to design better quality filters,” *IEEE Microwave Magazine*, vol. 22, no. 1, pp. 20–45, 2021.
- [94] R. J. Cameron, A. R. Harish, and C. J. Radcliffe, “Synthesis of advanced microwave filters without diagonal cross-couplings,” in *IEEE Transactions on Microwave Theory and Techniques*, vol. 50, no. 12, 12 2002, pp. 2862–2872.
- [95] D. Swanson and G. Macchiarella, “Microwave filter design by synthesis and optimization,” *IEEE Microwave Magazine*, vol. 8, no. 2, pp. 55–69, 4 2007.
- [96] Y. Zeng and M. Yu, “Mirroring physical reality: nonconventional microwave filter synthesis,” *IEEE Microwave Magazine*, vol. 25, no. 3, pp. 32–46, 3 2024.
- [97] R. Mansour, “High-Q tunable dielectric resonator filters,” *IEEE Microwave Magazine*, vol. 10, no. 6, pp. 84–98, 10 2009.
- [98] D. G. Swanson, “Narrow-band microwave filter design,” *IEEE Microwave Magazine*, vol. 8, no. 5, pp. 105–114, 10 2007.

- [99] E. Boni, M. Montagni, and L. Pugi, “Project VELA, upgrades and simulation models of the UNIFI autonomous sail Drone,” in *Lecture Notes in Electrical Engineering*, vol. 627, 2020.
- [100] M. S. Anwar and H. R. Dhanyal, “Design of S-band combline coaxial cavity bandpass filter,” in *2018 15th International Bhurban Conference on Applied Sciences and Technology*. IEEE, 1 2018, pp. 866–869.
- [101] E. Boni, G. Giannetti, S. Maddio, and G. Pelosi, “Capacitive end-couplings in combline microwave cavity filters with probe parallel to resonators’ axes: comparison and design guidelines,” in *2023 Kleinheubach Conference, 2023*, pp. 1–4.
- [102] R. Vincenti Gatti, R. Rossi, and M. Dionigi, “In-line stepped ridge coaxial-to-rectangular waveguide transition with capacitive coupling,” *International Journal of RF and Microwave Computer-Aided Engineering*, vol. 29, no. 3, 3 2019.
- [103] J. B. Ness, “A unified approach to the design, measurement, and tuning of coupled-resonator filters,” *IEEE Transactions on Microwave Theory and Techniques*, vol. 46, no. 4, pp. 343–351, 1998.
- [104] G. Macchiarella and S. Tamiazzo, “Novel approach to the synthesis of microwave diplexers,” *IEEE Transactions on Microwave Theory and Techniques*, vol. 54, no. 12, pp. 4281–4290, 12 2006.
- [105] A. Cidronali, G. Collodi, S. Maddio, G. Pelosi, and S. Selleri, “Quasi-elliptical band-pass filters based on compact spiral resonators for C-band applications,” *Microwave and Optical Technology Letters*, vol. 61, no. 8, pp. 1983–1987, 8 2019.
- [106] A. Cidronali, G. Collodi, M. Lucchesi, S. Maddio, G. Pelosi, and S. Selleri, “A multi-stage pass-band filter with ultra-compact spiral-based elements,” in *2020 XXXIIIrd General Assembly and Scientific Symposium of the International Union of Radio Science*. IEEE, 8 2020, pp. 1–4.
- [107] D. Bukuru, K. Song, and Xue, “Compact wide-stopband planar diplexer based on rectangular dual spiral resonator,” *Microwave and Optical Technology Letters*, vol. 57, no. 1, pp. 174–178, 1 2015.
- [108] T. Kokkinos, A. P. Feresidis, and J. C. Vardaxoglou, “Analysis and application of metamaterial spiral-based transmission lines,” in *2007 International workshop on Antenna Technology: Small and Smart Antennas Metamaterials and Applications*. IEEE, 3 2007, pp. 233–236.

- [109] T. K. Rekha, P. Abdulla, P. M. Jasmine, and A. R. Anu, "Compact microstrip lowpass filter with high harmonics suppression using defected structures," *AEU - International Journal of Electronics and Communications*, vol. 115, p. 153032, 2 2020.
- [110] J. D. Baena, J. Bonache, F. Martín, R. M. Sillero, F. Falcone, T. Lopetegi, M. A. Laso, J. García-García, I. Gil, M. F. Portillo, and M. Sorolla, "Equivalent-circuit models for split-ring resonators and complementary split-ring resonators coupled to planar transmission lines," *IEEE Transactions on Microwave Theory and Techniques*, vol. 53, no. 4 II, pp. 1451–1460, 4 2005.
- [111] J. García-García, F. Martín, F. Falcone, J. Bonache, J. D. Baena, I. Gil, E. Amat, T. Lopetegi, M. A. G. Laso, J. A. M. Iturmendi, M. Sorolla, and R. Marqués, "Microwave filters with improved stopband based on sub-wavelength resonators," *IEEE Transactions on Microwave Theory and Techniques*, vol. 53, no. 6, pp. 1997–2006, 2005.
- [112] G. Giannetti, "Gianne97/Comblin-cavity-filter-for- the-E1-Galileo-band: Comblin-cavity-filter-for- the-E1-Galileo-band-Supporting-Material," 12 2023. [Online]. Available: <https://doi.org/10.5281/zenodo.10246137>
- [113] M. Guglielmi and G. Connor, "Chained function filters," *IEEE Microwave and Guided Wave Letters*, vol. 7, no. 12, pp. 390–392, 1997.
- [114] C. E. Chrisostomidis and S. Lucyszyn, "On the theory of chained-function filters," *IEEE Transactions on Microwave Theory and Techniques*, vol. 53, no. 10, pp. 3142–3151, 2005.
- [115] Y. Xie, F. C. Chen, Q. X. Chu, and Q. Xue, "Dual-band coaxial filter and diplexer using stub-loaded resonators," *IEEE Transactions on Microwave Theory and Techniques*, vol. 68, no. 7, pp. 2691–2700, 7 2020.
- [116] E. Boni, G. Giannetti, S. Maddio, and G. Pelosi, "A circular polarized antenna for GPS and Iridium applications," in *2023 IEEE International Symposium on Antennas and Propagation*, 2023, pp. 195–196.
- [117] M. L. Crawford, "Generation of standard EM fields using TEM transmission cells," *IEEE Transactions on Electromagnetic Compatibility*, vol. EMC-16, no. 4, pp. 189–195, 11 1974.
- [118] *IEC 61000-4-20 Electromagnetic compatibility (EMC) – Part 4-20: Testing and measurement techniques – Emission and immunity testing in transverse*

- electromagnetic (TEM) waveguides*, International Electrotechnical Commission Std. IEC 61 000-4-20:2010.
- [119] B. N. Das and S. A. Mohan, “TEM cell in absence of one of the walls parallel to the septum,” *IEEE Transactions on Electromagnetic Compatibility*, vol. EMC-27, no. 2, pp. 58–63, 1985.
- [120] C. Spindelberger, G. Giannetti, and H. Arthaber, “Increasing the test-volume of open TEM cells by using an asymmetric design,” in *2022 Kleinhauheubach Conference*, 2022, pp. 1–4.
- [121] Y. Gu, Z. Zhou, J. Ren, M. Sheng, and Q. Zhou, “Calculation of ATEM Cell characteristic impedance based on static field approximation and MoM,” *IEEE Transactions on Electromagnetic Compatibility*, vol. 66, no. 3, pp. 694–705, 6 2024.
- [122] M. L. Crawford and J. L. Workman, “Asymmetric versus symmetric TEM cells for EMI measurements,” in *1978 IEEE International Symposium on Electromagnetic Compatibility*. IEEE, 6 1978, pp. 1–7.
- [123] P. Robrish, “An analytic algorithm for unbalanced stripline impedance,” *IEEE Transactions on Microwave Theory and Techniques*, vol. 38, no. 8, pp. 1011–1016, 1990.
- [124] *CISPR 16-1-1 Specification for radio disturbance and immunity measuring apparatus and methods - Part 1-1: Radio disturbance and immunity measuring apparatus - Measuring apparatus*, International Special Committee on Radio Interference Std. CISPR 16-1-1:2019.
- [125] F. Sporleder and H. G. Unger, *Waveguide Tapers, Transitions, and Couplers*, ser. IEE electromagnetic waves. New York (NY), USA: P. Peregrinus, 1979.
- [126] B. Z. Katsenelenbaum, L. Mercader del Rio, M. Pereyaslavets, M. Sorolla Ayza, and M. Thumm, *Theory of Nonuniform Waveguides: the cross-section method*. London, UK: Institution of Electrical Engineers, 1 1998.
- [127] C. Spindelberger, “Low-cost receivers for EMC measurements,” Ph.D. dissertation, Technische Universität Wien, 2024. [Online]. Available: <http://hdl.handle.net/20.500.12708/195067>
- [128] G. Giannetti, C. Spindelberger, and H. Arthaber, “Code for the paper entitled “Simple semi-analytical septum design for improved

- matching in open TEM cells,” 9 2023. [Online]. Available: <https://codeocean.com/capsule/9527921/tree/v1>
- [129] G. Conciauro, M. Guglielmi, and R. Sorrentino, *Advanced Modal Analysis: CAD Techniques for Waveguide Components and Filter*. Hoboken (NJ), USA: Wiley, 1999.
- [130] M. Baranowski, L. Balewski, A. Lamecki, M. Mrozowski, and J. Galdeano, “The design of cavity resonators and microwave filters applying shape deformation techniques,” *IEEE Transactions on Microwave Theory and Techniques*, vol. 71, no. 7, pp. 3065–3074, 7 2023.
- [131] W. X. Jiang, W. X. Tang, and T.-J. Cui, “Transformation optics and applications in microwave frequencies,” *Progress In Electromagnetics Research*, vol. 149, pp. 251–273, 2014.
- [132] M. McCall, J. B. Pendry, V. Galdi, Y. Lai, S. A. Horsley, J. Li, J. Zhu, R. C. Mitchell-Thomas, O. Quevedo-Teruel, P. Tassin, V. Ginis, E. Martini, G. Minatti, S. Maci, M. Ebrahimpouri, Y. Hao, P. Kinsler, J. Gratus, J. M. Lukens, A. M. Weiner, U. Leonhardt, I. I. Smolyaninov, V. N. Smolyaninova, R. T. Thompson, M. Wegener, M. Kadic, and S. A. Cummer, “Roadmap on transformation optics,” *Journal of Optics (United Kingdom)*, vol. 20, no. 6, p. 063001, 6 2018.
- [133] A. Nestic, M. Blaicher, E. Orlandini, T. Olariu, M. Paszkiewicz, F. Negrado, P. Kraft, M. Sukhova, A. Hofmann, W. Dörfler, C. Rockstuhl, W. Freude, and C. Koos, “Transformation-optics modeling of 3D-printed freeform waveguides,” *Optics Express*, vol. 30, no. 21, p. 38856, 10 2022.
- [134] T. N. Kaifas, E. Vafiadis, X. M. Mitsalás, G. Granet, J. N. Sahalos, and G. A. Kyriakou, “Transformation electromagnetics eigenanalysis of perfect electric conductor cavities,” *IET Microwaves, Antennas and Propagation*, vol. 12, no. 8, pp. 1435–1443, 7 2018.
- [135] G. G. Gentili, G. Giannetti, M. Khosronejad, G. Pelosi, and S. Selleri, “Modes computation in arbitrarily shaped waveguides by a transformation optics approach,” *International Journal of RF and Microwave Computer-Aided Engineering*, vol. 31, no. 1, 2021.
- [136] G. Garcia-Contreras, J. Córcoles, J. A. Ruiz-Cruz, M. Oldoni, G. G. Gentili, S. Micheletti, and S. Perotto, “Advanced modeling of rectangular waveguide

- devices with smooth profiles by hierarchical model reduction,” *IEEE Transactions on Microwave Theory and Techniques*, vol. 71, no. 11, pp. 4692–4702, 2023.
- [137] J. R. James and P. S. Hall, Eds., *Handbook of Microstrip Antennas, Volume 1*. Stevenage, UK: Institution of Engineering and Technology, 1 1989.
- [138] ———, *Handbook of Microstrip Antennas, Volume 2*. Stevenage, UK: Institution of Engineering and Technology, 1 1989.
- [139] U. Papziner and F. Arndt, “Field theoretical computer-aided design of rectangular and circular iris coupled rectangular or circular waveguide cavity filters,” *IEEE Transactions on Microwave Theory and Techniques*, vol. 41, no. 3, pp. 462–471, 1993.
- [140] G. Bertin, B. Piovano, L. Accatino, and M. Mongiardo, “Full-wave design and optimization of circular waveguide polarizers with elliptical irises,” *IEEE Transactions on Microwave Theory and Techniques*, vol. 50, no. 4, pp. 1077–1083, 4 2002.
- [141] G. Virone, R. Tascone, M. Baralis, O. A. Peverini, A. Olivieri, and R. Orta, “A novel design tool for waveguide polarizers,” *IEEE Transactions on Microwave Theory and Techniques*, vol. 53, no. 3 I, pp. 888–893, 3 2005.
- [142] M. K. Thumm and W. Kasperek, “Passive high-power microwave components,” *IEEE Transactions on Plasma Science*, vol. 30, no. 3 I, pp. 755–786, 2002.
- [143] M. Thumm and H. Kumric, “High-power TE<sub>11</sub> and TM<sub>11</sub> circular polarizers in oversized waveguides at 70 GHz,” *International Journal of Infrared and Millimeter Waves*, vol. 10, no. 9, pp. 1059–1075, 9 1989.
- [144] T. Stange, “Simple Broadband Circular Polarizer in Oversized Waveguide,” *Journal of Infrared, Millimeter, and Terahertz Waves*, vol. 37, no. 2, pp. 137–146, 2 2016.
- [145] P. Arcioni, M. Bressan, and L. Perregrini, “A new boundary integral approach to the determination of the resonant modes of arbitrarily shaped cavities,” *IEEE Transactions on Microwave Theory and Techniques*, vol. 43, no. 8, pp. 1848–1856, 1995.
- [146] C. Tomassoni, O. A. Peverini, G. Venanzoni, G. Addamo, F. Paonessa, and G. Virone, “3D printing of microwave and millimeter-wave filters: additive manufacturing technologies applied in the development of high-performance

- filters with novel topologies,” *IEEE Microwave Magazine*, vol. 21, no. 6, pp. 24–45, 6 2020.
- [147] W. Huting and K. Webb, “Comparison of mode-matching and differential equation techniques in the analysis of waveguide transitions,” *IEEE Transactions on Microwave Theory and Techniques*, vol. 39, no. 2, pp. 280–286, 1991.
- [148] M. S. Gockenbach, *Understanding and Implementing the Finite Element Method*, ser. Other Titles in Applied Mathematics. Philadelphia (PA), USA: Society for Industrial and Applied Mathematics, 2006.
- [149] G. G. Gentili, “Properties of TE—TM mode-matching techniques,” *IEEE Transactions on Microwave Theory and Techniques*, vol. 39, no. 9, pp. 1669–1673, 1991.
- [150] G. Figlia and G. G. Gentili, “On the line-integral formulation of mode-matching technique,” *IEEE Transactions on Microwave Theory and Techniques*, vol. 50, no. 2, pp. 578–580, 2 2002.
- [151] M. Bozzi, G. Conciauro, and L. Perregrini, “On the evaluation of modal coupling coefficients by contour integrals,” *IEEE Transactions on Microwave Theory and Techniques*, vol. 50, no. 7, pp. 1853–1855, 7 2002.
- [152] V. Crinó, C. Tomassoni, and M. Mongiardo, “Comparison between line and surface integral formulations of the hybrid mode-matching/two-dimensional finite element method,” *International Journal of Numerical Modelling: Electronic Networks, Devices and Fields*, vol. 17, no. 6, pp. 575–592, 11 2004.
- [153] D. S. Nagarkoti, R. Sharma, R. L. Dua, and P. K. Jain, “Analysis of nonlinear cylindrical waveguide taper using modal matching technique,” *WARSE International Journal of Microwaves Applications*, vol. 1, no. 1, pp. 5–12, 2012.
- [154] G. Giannetti, “Mode fields computed with a transformation optics approach,” 3 2023. [Online]. Available: <https://codeocean.com/capsule/8589037/tree/v1>
- [155] G. Pelosi, R. Coccioli, and S. Selleri, *Quick finite elements for electromagnetic waves*, 2nd ed. Norwood (MA), USA: Artech House, 2009.
- [156] G. Giannetti, “Mode matching analysis of waveguide devices applied to mode fields computed with the transformation optics approach,” 4 2023. [Online]. Available: <https://codeocean.com/capsule/7937632/tree/v1>

- [157] P. Booth and E. V. Lluch, “Enhancing the performance of waveguide filters using additive manufacturing,” *Proceedings of the IEEE*, vol. 105, no. 4, pp. 613–619, 11 2016.
- [158] G. Giannetti, M. Bellaveglia, A. Gallo, S. Maddio, A. Mostacci, L. Piersanti, B. Serenellini, S. Selleri, and S. Tocci, “In-house design, manufacturing, and testing of a 2.856 GHz combline microwave cavity filter for the low-level RF systems of linear particle accelerators,” *Advanced Electromagnetics*, vol. 14, no. 1, pp. 8–13, 2 2025.
- [159] L. Piersanti, D. Alesini, M. Bellaveglia, S. Bini, B. Buonomo, F. Cardelli, C. D. Giulio, E. D. Pasquale, M. Diomede, L. Faillace, A. Falone, G. Franzini, A. Gallo, G. Giannetti, A. Liedl, D. Moriggi, S. Pioli, S. Quaglia, L. Sabbatini, M. Scampati, G. Scarselletta, A. Stella, S. Tocci, and L. Zelinotti, “Commissioning and first results of an X-band LLRF system for TEX test facility at LNF-INFN,” in *Journal of Physics: Conference Series*, vol. 2420, no. 1. IOP Publishing, 1 2023, p. 12075.
- [160] G. G. Gentili, G. Giannetti, S. Maddio, and M. Oldoni, “A gap coupled patch array based on the multilobate design,” in *2023 IEEE International Symposium on Antennas and Propagation*, 2023, pp. 477–478.
- [161] G. Giannetti and L. Klinkenbusch, “The contributions to electromagnetism achieved by Heinrich Hertz at Kiel University,” in *2023 8th IEEE History of Electrotechnology Conference*. IEEE, 9 2023, pp. 1–3.
- [162] A. Giribono, D. Alesini, A. Bacci, M. Bellaveglia, F. Cardelli, E. Chiadroni, A. Del Dotto, L. Faillace, M. Ferrario, A. Gallo, A. Ghigo, G. Giannetti, A. Mostacci, M. Opromolla, V. Petrillo, L. Piersanti, R. Pompili, S. Romeo, M. Rossetti Conti, A. R. Rossi, V. Shpakov, G. J. Silvi, and C. Vaccarezza, “Electron beam analysis and sensitivity studies for the EUPRAXIA@SPARC LAB RF injector,” in *Journal of Physics: Conference Series*, vol. 2687, no. 3. IOP Publishing, 1 2024, p. 032022.
- [163] G. Giannetti, C. Spindelberger, S. Selleri, and H. Arthaber, “Effects of the ground plane and of neighbouring objects on the performances of open TEM cells,” in *2024 IEEE International Symposium on Antennas and Propagation*, 2024, pp. 2731–2732.
- [164] G. Giannetti, S. Maddio, and S. Selleri, “A twelve-element sequentially rotated array for circular polarization links at 5.8 GHz,” in *2024 IEEE International Symposium on Antennas and Propagation*, 2024, pp. 2535–2536.

- 
- [165] K. Davidhi, G. Giannetti, M. Righini, and S. Selleri, “A compact passband filter based on folded split ring resonators for ISM applications at 5.8GHz,” in *2024 IEEE International Symposium on Antennas and Propagation*, 2024, pp. 2697–2698.
- [166] G. G. Gentili, G. Giannetti, S. Maddio, and M. Oldoni, “A filtenna based on gap coupled multilobate design for C-band applications,” in *2024 IEEE International Symposium on Antennas and Propagation*, 2024, pp. 2625–2626.
- [167] G. Giannetti and L. Klinkenbusch, “Interpretation and separability of the effective permittivity in case that both permittivity and conductivity are complex,” in *2023 URSI International Symposium on Electromagnetic Theory*, 2023.